University of Massachusetts Amherst

ScholarWorks@UMass Amherst

March 2016

Modeling, Analysis and Numerical Simulations in Mathematical Biology of Traveling Waves, Turing Instability and Tumor Dynamics

Mei Duanmu

MODELING, ANALYSIS AND NUMERICAL SIMULATIONS IN MATHEMATICAL BIOLOGY OF TRAVELING WAVES, TURING INSTABILITY AND TUMOR DYNAMICS

A Dissertation Presented

by

MEI DUANMU

Submitted to the Graduate School of the
University of Massachusetts Amherst in partial fulfillment
of the requirements for the degree of

DOCTOR OF PHILOSOPHY

February 2016

Department of Mathematics and Statistics

MODELING, ANALYSIS AND NUMERICAL SIMULATIONS IN MATHEMATICAL BIOLOGY OF TRAVELING WAVES, TURING INSTABILITY AND TUMOR DYNAMICS

A Dissertation Presented

by

MEI DUANMU

Approved as to style and content by:

_____

Nathaniel Whitaker, Chair

_____

Panayotis G. Kevrekidis, Member

_____

Qianyong Chen, Member

_____

Triantafillos Mountziaris, Member

_____

Farshid Hajir, Department Head
Department of Mathematics and Statistics

To my parents.

ACKNOWLEDGMENTS

ABSTRACT

MODELING, ANALYSIS AND NUMERICAL SIMULATIONS IN MATHEMATICAL BIOLOGY OF TRAVELING WAVES, TURING INSTABILITY AND TUMOR DYNAMICS

FEBRUARY 2016

MEI DUANMU

B.Sc., DALIAN UNIVERSITY OF TECHNOLOGY

M.Sc., UNIVERSITY OF MASSACHUSETTS AMHERST

Ph.D., UNIVERSITY OF MASSACHUSETTS AMHERST

Directed by: Professor Nathaniel Whitaker

The dissertation includes three topics in mathematical biology. They are traveling wave solutions in a chain of periodically forced coupled nonlinear oscillators, Turing instability in a HCV model and tumor dynamics.

Motivated by earlier studies of artificial perceptions of light called phosphenes, we analyze traveling wave solutions in a chain of periodically forced coupled nonlinear oscillators modeling this phenomenon. We examine the discrete model problem in its co-traveling frame and systematically obtain the corresponding traveling waves in one spatial dimension. Direct numerical simulations as well as linear stability analysis are employed to reveal the parameter regions where the traveling waves are stable, and these waves are, in turn, connected to the standing waves analyzed in earlier work. We also consider a two-dimensional extension of the model and demonstrate the robust

evolution and stability of planar fronts and annihilation of radial ones. Finally, we show that solutions that initially feature two symmetric fronts with bulged centers evolve in qualitative agreement with experimental observations of phosphenes.

For hepatitis C virus (HCV) model, using the Routh-Hurwitz conditions, we prove in most parameter regimes that there can be no Turing instability. The simulations support this in all parameter regions of the model. We introduce a modified model where Turing instability is observed.

For tumor dynamics model, we present the Fisher Kolomogorov equation (PDE) and the effective particle methods (ODE) for single front solution and localized solution with and without radiation. The predicted lifetimes of the patients from the PDE and ODE are compared and show good quantitative agreement.

TABLE OF CONTENTS

LIST OF TABLES

LIST OF FIGURES

CHAPTER 1

INTRODUCTION

In the dissertation, we discuss three topics in mathematical biology. They are traveling wave solutions in a chain of periodically forced coupled nonlinear oscillators, Turing instability in a HCV model and tumor dynamics. Chapter 1 through Chapter 6 study the topic of traveling wave solution. Chapter 7 simplifies the hepatitis C virus (HCV) model and analyzes Turing instability by adding diffusion terms. Chapter 8 studies the tumor dynamics and compares effects of different radiation methods.

1.1 Introduction to traveling wave solutions in a chain of periodically forced coupled nonlinear oscillators

Electrical stimulation of the retina can produce artificial perceptions of luminance changes called phosphenes, which may also arise in early stages of retinal or visual disease [1]. The induction of phosphenes is being used to help restore vision or develop visual aids for patients with severely compromised vision [2, 3], and an understanding of how phosphenes arise and behave could contribute to such efforts. In a detailed experimental study [4], Carpenter explored electrically induced phosphenes in human subjects. Each subject's eyes were immersed in a saline bath to which an alternating current was applied. When a dark object was passed through a subject's visual field in the presence of such stimulation, visual perceptions of line phosphenes occurred in its wake. The lines were observed to move and interact but never cross. This work suggested the presence of a bistability of activity states in the system, with

the moving lines representing boundaries between sets of cells in different activity regimes.

Drover and Ermentrout [5] developed a one-dimensional model providing a simple representation of the phosphenes in Carpenter's experiments and their motion. In their work, a chain of excitable neurons was driven by a spatially uniform periodic stimulus at a frequency higher than the cells could follow, inducing a 1 : 2 phase locking with the stimulus. In the absence of coupling, neurons could fire on even or odd cycles of the stimulus, resulting in an intrinsic bistability for the forced system. Sufficiently strong coupling, even if directionally unbiased, elicited unidirectional traveling waves in which cells were recruited to switch phase. Large amplitude forcing of an excitable system is a difficult problem to tackle analytically. In view of that difficulty, the more recent analysis of [6] assumed that each neuron is intrinsically oscillatory and characterized by a state evolving at half the frequency of an applied forcing signal. Using multiple time scale expansion and the Fredholm alternative, the authors of [6] derived a more analytically tractable *effective model* for the time evolution of the neurons' phases. This reduced model, which is quite general and particularly interesting in its own right, will be the focus of the present work.

In [6], a detailed numerical existence and stability analysis was done using XP-PAUT [7] for a finite chain of coupled phase oscillators. Certain interesting bifurcation phenomena were identified including saddle-node and pitchfork bifurcations in a two-dimensional parameter space characterizing the strength and asymmetry of coupling between nearest-neighbor oscillators. In Chapter 2, we derived the bifurcation curves and analyze the standing wave solutions. Beyond the critical points involved in these bifurcations, direct numerical simulations identified traveling waves that are strongly reminiscent of the "recruitment waves" obtained in the original chain of forced neural oscillators. It is exactly these traveling waves that we systematically obtain and analyze in Chapter 3, by a combination of numerical and, whenever possible, semi-

analytical techniques. Specifically, we consider the exact traveling wave problem, which takes the form of an advance-delay differential ordinary equation in the co-traveling frame of such waves and which we introduce along with the mathematical formulation of the problem in Chapter 3. In this chapter, we solve the problem numerically, identifying exact (up to numerical error) traveling and standing (zero-speed) waves within the full two-dimensional parameter space used in [6]. We explore the stability of these waves in two complementary ways. On the one hand, we consider the traveling waves as steady states of the associated advance-delay partial differential equation (PDE). On the other hand, we examine them via direct numerical simulations of the original system of ordinary differential equations (ODEs) for the coupled oscillators with the initial condition "distilled" on the lattice from the obtained traveling wave solution. In [6], this problem was studied in a limited range for the parameter μ measuring the asymmetry of the nearest-neighbor coupling function. In Chapter 4, our analysis extends to all values of μ. We show that traveling waves are stable in certain parameter regions that are periodic in μ and are located above a certain curve, below which there exist stable standing waves. The stability regions alternate along the direction of μ with regions where the waves are unstable due to the instability of the background state as well as a frontal instability. Simulations of the lattice system initialized by an unstable traveling wave show that the frontal instability results in formation of two fronts that propagate in the opposite directions with the same speed as the initial wave.

In Chapter 5, we extend the lattice model to a two-dimensional setting and show that the planar fronts obtained from the one-dimensional traveling wave are very robust even with a local initial distortion, unlike radial fronts, which are eventually annihilated in the dynamical evolution. Finally, we consider the evolution of two symmetric fronts with initially bulged centers and show that the resulting dynamics is in agreement with Carpenter's findings, based on observations of phosphenes, that

lines form loops instead of crossing through each other and that a line does not break apart unless it meets another line. In Chapter 6, we compare the traveling wave solutions and stability of these solutions with forward and centered difference method.

1.2 Introduction to Turing instability in a HCV model

In Chapter 7, we introduce a Hepatitis C Virus (HCV) model and analyze the Turing instability. Approximately 200 million people worldwide [35] are persistently infected with the HCV and are at risk of developing chronic liver disease, cirrhosis, and hepatocellular carcinoma [29]. In [32], a standard HCV viral-dynamic model of infection and clearance was proposed. Dahari and coauthors expanded this model by incorporating density-dependent proliferation and death in [33] and [34]. Reluga [29] further developed HCV model based on the work of [33], [34] by adding self curve of infected hepatocytes. In the dissertation, 3-equation model and 2-equation model are analyzed and compared. Diffusion terms are added to each of the 2-equation and 3-equation system. Using the Routh-Hurwitz conditions, we prove that in most parameter regions there can be no Turing instability (diffusion driven instability). Our simulations support this in all parameter regions of the model. We introduce a modified model where Turing instability is demonstrated. In Chapter 7 section 1, we introduce the 3-equation model consisting of the uninfected, infected and virus terms as well as the analysis of Turing instability by adding a diffusion term. In section 2, we set up a 2-equation model and analyze Turing instability by adding a diffusion term. Section 3 is a numerical comparison of solution to 2-equation and 3-equation model. Section 4 proposes a new model to observe Turing instability. Section 5 is an introduction to Routh-Hurwitz conditions which we apply to analyze Turing instability in section 2 and 3.

1.3 Introduction to tumor dynamics

In Chapter 8, we introduce the tumor cell population model without and with radiation. In [47], Fisher-Kolmogorov (FK) equation $u_t = Du_{xx} + \rho u(1-u)$ is used to describe the dynamics of a tumor cell population density $u(x,t)$. D and ρ represent dispersal rate and proliferation rate. In [47], some ordinary differential equations (ODEs) are derived for front parameters arising in the FK equation. These effective equations (ODEs) are derived for both the single front solution and localized solution. This is called effective particle method. Results of the effective particle method and the FK equation are compared and shown to be in good quantitative agreement. In this dissertation, radiotherapy is brought into the model as a process to reduce both tumor and normal cells. We modify the model of FK equation and effective particle methods by updating the tumor cell density according to survival probability of each radiation method. Based on clinical observation, the lifetime cut off criteria are set. By the cut off criteria, different radiation methods are designed and corresponding lifetime is derived. In Chapter 8 section 1, we present the FK (PDE) equation and the ODE (effective particle methods) for a single front solution with and without radiation. The lifetime predicted from the PDE and ODE are compared in section 2. In section 3 and section 4, FK equation and ODE are derived for localized solution. The simulated lifetime for localized solution are listed and compared. In section 5, low grade glioma radiation is introduced and corresponding lifetime is calculated and compared. Also we design the radiotherapy methods by keeping the damage to the normal tissue the same and compare the lifetime.

CHAPTER 2

ONE DIMENSIONAL STANDING WAVE

In this chapter, we consider the existence and stability of standing wave solution of one-dimensional phase equations system with N oscillators. First, we study the existence of standing wave solution. Then we study the stability of standing wave solution. When the standing wave solution stability changes, we derive the pitchfork and saddle-node bifurcation curves as shown in Fig. 2.7. Finally, we analyze the pitchfork and saddle-node bifurcation with respect to parameters μ and k.

2.1 Discrete system with coupling (ODE system)

Consider a chain of N periodically forced oscillators governed by the reduced spatially discrete model of stimulated retinal cells derived in [6]:

$$
\begin{aligned}
\dot{\theta}_{-n} &= kH(\theta_{-n+1} - \theta_{-n}) + f(\theta_{-n}) \\
\dot{\theta}_{j} &= k[H(\theta_{j-1} - \theta_{j}) + H(\theta_{j+1} - \theta_{j})] + f(\theta_{j}), \quad \text{for} \ \ j = -n+1, \ldots, N-n-2 \\
\dot{\theta}_{N-n-1} &= kH(\theta_{N-n-2} - \theta_{N-n-1}) + f(\theta_{N-n-1}).
\end{aligned}
$$

$$(2.1)$$

Here $\theta_j(t)$ is the slowly evolving phase of each neuron, $f(\theta)$ is a π-periodic forcing or locking function, and $H(\theta)$ is a 2π-periodic function characterizing the coupling of the nearest neighbors and multiplied by the coupling constant $k > 0$. The periodicities of $f(\theta)$ and $H(\theta)$ represent the $1 : 2$ frequency locking present in the system and can be easily generalized to different types of frequency locking. In [6] the number of oscillators was set to be even, $N = 2n$, but here we also allow it to be odd, $N = 2n+1$.

6

In what follows, we consider prototypical examples of the two functions proposed in [6],

$$H(\theta) = \sin(\theta + \mu) - \sin(\mu), \quad f(\theta) = -\sin(2\theta),$$

where the parameter μ measures the asymmetry of the coupling function $H(\theta)$. We can identify 0 with 2π such that $\theta_j \in [0, 2\pi)$ and then the firing of the jth neuron corresponds to θ_j crossing through some distinguished value, taken for some oscillator models, for example, to be $\theta_j = \pi$. It is not hard to see that in the case of $\mu = 0$, when $H(\theta) = \sin\theta$ is odd, there exist equilibrium split state (antiphase) solutions given by

$$(\theta_{-n}, \ldots, \theta_{-1}, \theta_0, \ldots, \theta_{N-n-1}) = (0, \ldots, 0, \pi, \ldots, \pi) \quad \text{and} \quad (\pi, \ldots, \pi, 0, \ldots, 0).$$

If $N = 2n$, these solutions have equal numbers of oscillators firing in each cycle. When μ is nonzero, such piecewise constant split states no longer exist. However, there are single-front equilibrium split states that are close to the above antiphase state but have boundary layers near the front. In [6], such steady state solutions of (2.1) are obtained numerically by varying μ and k.

2.2 Existence and stability of standing waves for the chain

In [6], the bifurcation curve is derived for $N = 10$ as shown in Fig. 2.1. We calculate the bifurcation curve for $N = 50$ which is similar to the one for $N = 10$ derived in [6].

To study the solution to the discrete ODE system, we select two pairs of (μ, k) and solve the steady state ODE ($\frac{d\theta_i}{dt} = 0$) at these parameter points with Newton method. When $\mu = 0.5$, $k = 0.5$, the solution is shown in Fig. 2.2 part (a). In part (b), the evolution of the solution until $t = 50$ solved with Runge Kutta method is shown. From the figure, the wave stays at the same position without moving until

(a)
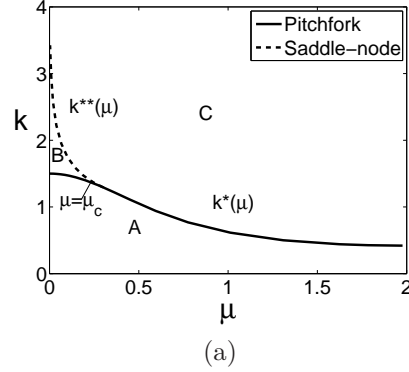
Figure 2.1: Bifurcation diagram for stationary solutions of the system (2.1) with $N = 2n = 10$, as obtained in [6]. The primary split state equilibria are stable in region A and destabilize via a pitchfork bifurcation (solid curve, $(k = k^*)$. At $\mu < \mu_c$ the bifurcation is supercritical and gives rise to a pair of secondary split state equilibria that are stable in region B and disappear through a saddle-node bifurcation (dashed curve, $k = k^{**}(\mu)$), $\mu < \mu_c$.

(a)   (b)
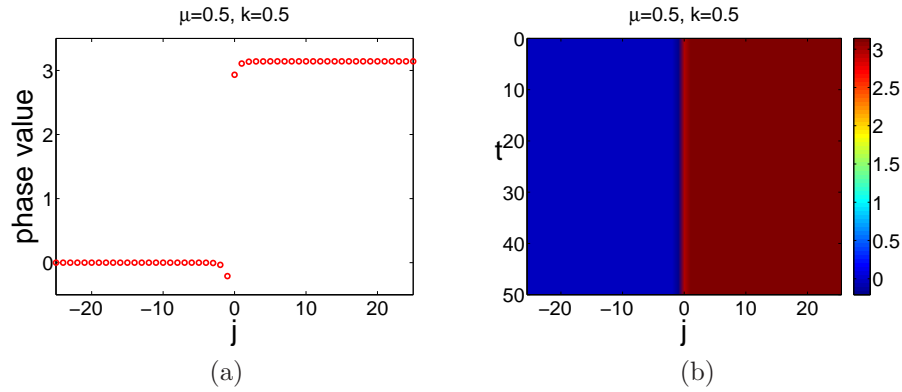
Figure 2.2: Part (a), standing wave solution at $\mu = 0.5$, $k = 0.5$. Part (b), time evolution of the standing wave solution until $t = 50$.

$t = 50$ which means the solution is a standing wave solution. When $\mu = 0.5$, $k = 1.5$, the solution (part (a)) and time evolution (part (b)) until $t = 50$ are shown in Fig. 2.3. From the time evolution plot, we can see that the solution is not a standing wave solution and in fact is a traveling wave which we discuss later.
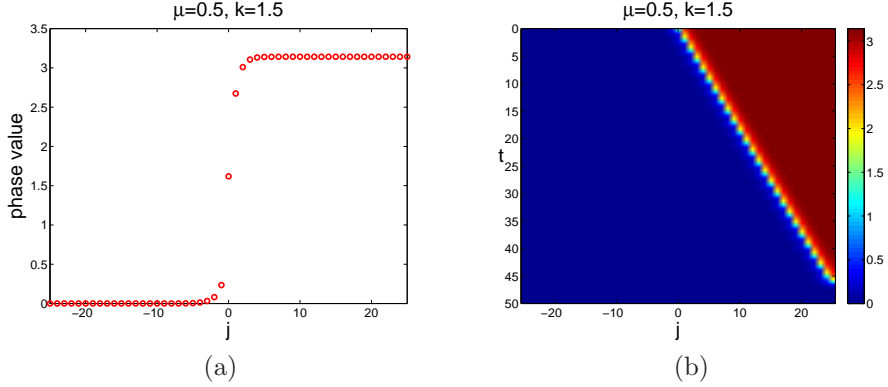
Figure 2.3: Part (a), traveling wave solution at $\mu = 0.5$, $k = 1.5$. Part (b), time evolution of the traveling wave solution until $t = 50$.

2.2.1 Derivation of Pitchfork curve

We take the initial guess of the split state solution to be $[0, \ldots, 0, \pi, ..., \pi]$ at $k = 0.4$. We use this initial guess at $k = 0.4$ to solve the ODE system with Newton method. With the parameter (k) continuation and Newton's method, we can obtain the solution along k for a fixed μ. As shown in Fig. 2.4 left panel, marching upward (arrow direction) with parameter continuation from $k = 0.4$, we can check maximum real part of eigenvalue of Jacobian matrix for different value of k. In Fig. 2.4 right panel, this is the table of maximum real value of eigenvalue for each value of k. When k is small and below the bifurcation curve, the maximum real part of eigenvalue is negative which means the standing wave solution is stable. As k increases, the maximum real part of eigenvalue increases from negative to positive around $k = 1.0492$ where the standing wave solution becomes unstable. Connecting all the points the standing wave stability changes gives the pitchfork bifurcation curve as shown in Fig. 2.4 blue curve.

μ	k	max(eig)
0.5	0.4	-1.4034
0.5	0.6	-1.0266
0.5	0.8	-0.6021
0.5	1.0	-0.1260
0.5	1.0491	-2.2424e-4
0.5	1.0492	3.5834e-5
0.5	1.2	0.4124
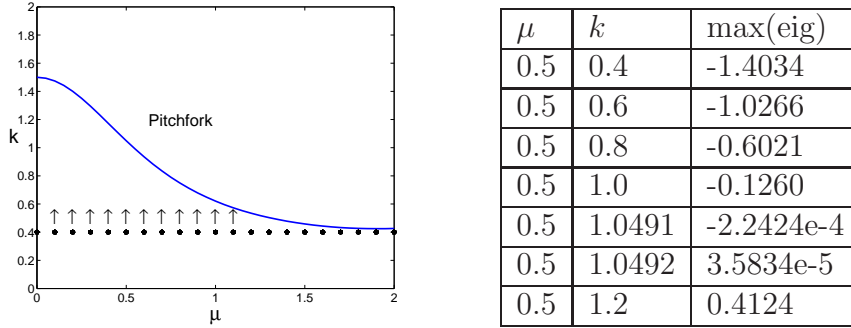
Figure 2.4: Left: Pitchfork curve (blue) obtained through standing wave solution stability analysis. Up arrow means the parameter continuation direction. Right table: maximum real part of eigenvalue around pitchfork bifurcation for $\mu = 0.5$.

2.2.2 Derivation of Saddle-node curve

Let the initial guess of the split state solution $[0, ..., 0, \pi/2, \pi, ..., \pi]$ evolve with Runge Kutta method at parameter $\mu = 0.1$, $k = 1.6$. Thus the initial guess evolves into initial solution at this point. With the parameter continuation, we have the solution along $\mu = 0$ within domain $k > 1.5$. For a fixed value of $k > 1.5$, starting from the solution along $\mu = 0$, we march towards right with parameter (μ) continuation and Newton's method. We can have the solution by checking maximum real part of eigenvalue. As shown in Fig. 2.5 right panel, for fixed value of k, with increase of μ, the maximum eigenvalue increase to value close to 0 which means the Jacobian matrix is close to singular. From the table, the Jacobian matrix is closed to singular around $\mu = 0.0599$. Also this is where the standing wave solution change from stable to unstable. Connecting all these points, we get the saddle-node curve(green) in Fig. 2.5 left panel.

For the region between pitchfork and saddle-node curves and $k < 1.5$, we zoom in this region and shown in Fig. 2.6 left panel. With parameter continuation and Newton's method, marching towards right until where the Jacobian matrix becomes singular. This is where the standing wave solution changes from stable to unstable. As

10
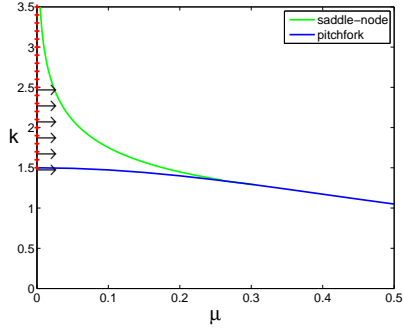
μ	k	max(eig)
0.025	2.0	-0.5892
0.03	2.0	-0.5477
0.035	2.0	-0.5007
0.04	2.0	-0.4473
0.045	2.0	-0.3857
0.0598	2.0	-0.0199
0.0599	2.0	singular

Figure 2.5: Left: Saddle-node curve (green) obtained through standing wave solution stability analysis. Right arrow means the parameter continuation direction. Right table: maximum real part of eigenvalue around saddle-node bifurcation curve for $k = 2$.
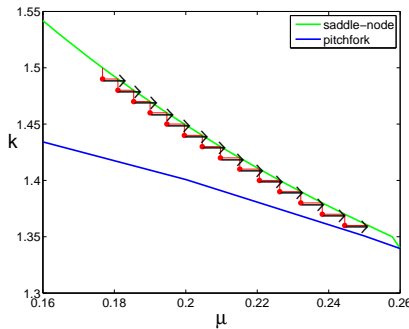
μ	k	max(eig)
0.2445	1.36	-0.0102
0.2450	1.36	-0.0115
0.2460	1.36	-0.0140
0.2480	1.36	-0.0175
0.2500	1.36	-0.0160
0.2510	1.36	-0.0022
0.2511	1.36	singular

Figure 2.6: Left: Saddle-node curve (green) below $k = 1.5$ obtained through standing wave solution stability analysis. Right arrow means the parameter continuation direction. The ladder shape in the figure shows that we use the solution at one point as initial guess for next ladder. Right table: maximum of real eigenvalue around saddle-node bifurcation curve for $k = 1.36$.

shown in Fig. 2.6 right panel, the Jacobian matrix becomes singular near $\mu = 0.2511$. Connecting these points give the saddle-node curve below $k = 1.5$.

2.3 Bifurcation analysis

As we derived the pitchfork and saddle-node curves from previous section, a prototypical example of the resulting diagram in the (μ, k) plane is shown in Fig. 2.7 part (a) with 50-oscillator system, adapted from Fig. 2.1 (10-oscillator) in [6]. The primary split state solution is stable in a region of small enough k (region A) but
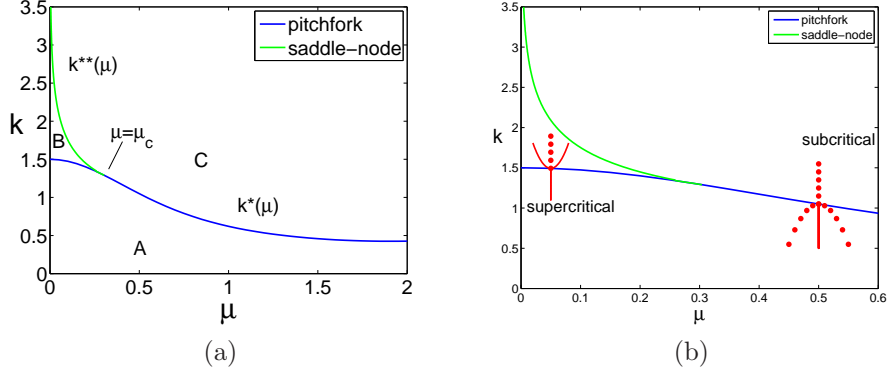
Figure 2.7: Part (a) Bifurcation diagram for stationary solutions of the ODE system (2.1) with $N = 2n = 50$, similar with the one obtained in [6] with $N = 10$. The primary split state equilibria are stable in region A and destabilize via a pitchfork bifurcation (blue curve, $k = k^*(\mu)$). At $\mu < \mu_c$ the bifurcation is supercritical and gives rise to a pair of secondary split state equilibria that are stable in region B and disappear through a saddle-node bifurcation (green curve, $k = k^{**}(\mu)$, $\mu < \mu_c$). Part (b) Graph illustration of supercritical pitchfork curve ($\mu < \mu_c$) and subcritical pitchfork curve ($\mu > \mu_c$).

becomes unstable through a pitchfork bifurcation at $k = k^*(\mu)$ shown by the solid curve. As shown in Fig. 2.7 part (b), the pitchfork bifurcation is subcritical for μ above a certain threshold, $\mu > \mu_c$. For $\mu < \mu_c$, the bifurcation is supercritical and gives rise to two other, secondary, stable nonsymmetric split states that exist in region B. These states, in turn, disappear through a saddle-node bifurcation at $k = k^{**}(\mu)$ (green curve), where $k^{**}(\mu) > k^*(\mu)$.

Then we explore the pitchfork and saddle-node bifurcation curves in detail. As shown in Fig. 2.7 part (a), pitchfork bifurcation curve (blue) and saddle-node bifurcation curve (green) separate the parameter region into three regions A, B and C. From region A to region B, with the increase of k to $k^*(\mu)$, one stable solution branch bifurcates into two stable branches and one unstable branch. To observe this, Fig. 2.8 part (a) shows the bifurcation diagram (θ_{25} vs k) for a 50-oscillator system at $\mu = 0.025$. θ_{25} is the phase value of the 25th oscillator. With the increase of k from 0, the stable

branch bifurcates into two stable branches and one unstable branch when $k = k^*$. The unstable branches is the continuation of stable branch when $k < k^*$. This means keeping on the same branch, the solution becomes unstable with the increase of k and turns back around $k = 450$ which is shown in part (b). The value of θ_{25} returns to value near $-\pi/2$ when $k = 0$. Along two stable branches, the curves turn back near $k^{**}(\mu)$ which is on the saddle-node bifurcation and the solution becomes unstable. In part (c) and (d), two stable solution at $(\mu = 0.025, k = 2)$ on two stable branches are shown. Compared with part (a), the value of θ_{25} at black points $(k = 2)$ are phase value at the 25th oscillator of part (c) and (d). Similarly, in Fig. 2.9, the bifurcation diagram at $\mu = 0.1$ is shown. With the increase of k, the stable solution branch bifurcates into two stable branches and one unstable branch. The stable branches change to unstable and turn back at $k^{**}(\mu)$ which is on the saddle-node curve. The unstable branch turns back near $k = 45$ as shown in Fig. 2.10 part (b). In Fig. 2.9 part (b) and (c), two stable solutions at $(\mu = 0.1, k = 1.6)$ are shown. Compared with part (a), the phase value at the 25th oscillator is the θ_{25} value at the red points$(k = 1.6)$.
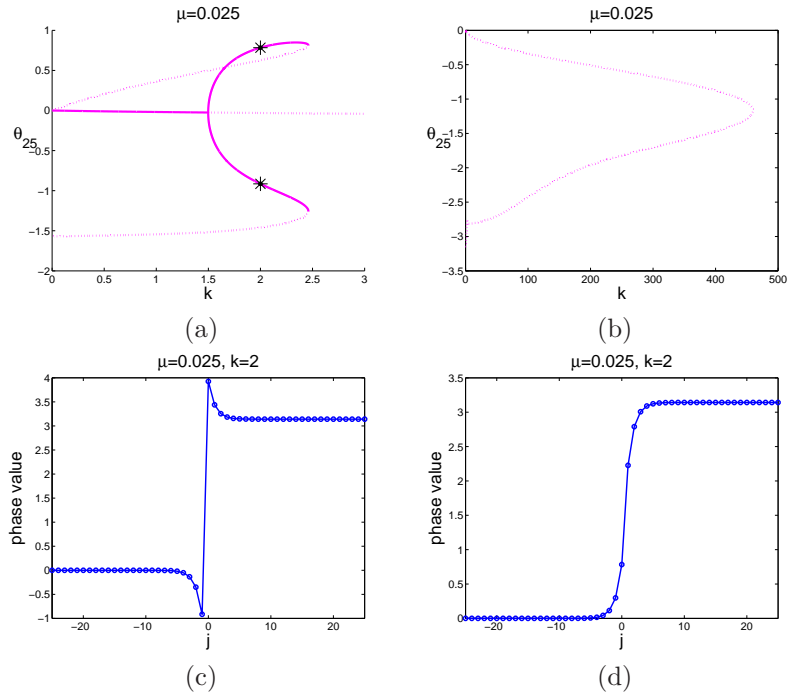
Figure 2.8: Part (a) Bifurcation diagram for $\mu = 0.025$ of 50-oscillator system. The solid line represents stable solution branch. The dashed line represents unstable solution branch. Part (b) An overview of whole bifurcation diagram on a large domain of k. The bifurcation diagram turns back around $k = 450$. Part (c), (d) Two stable standing wave solution at $(\mu = 0.025, k = 2)$.
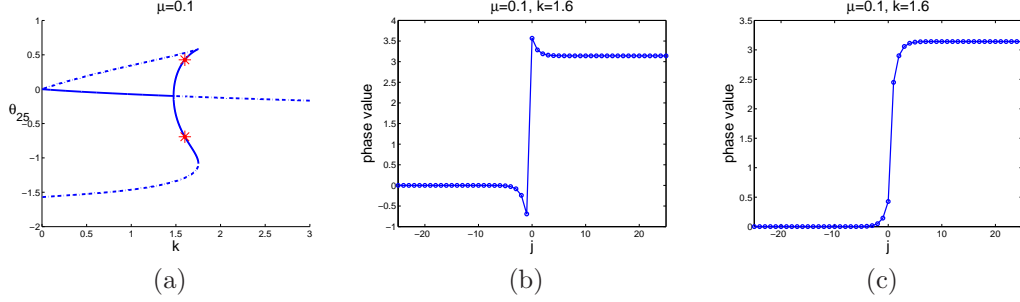
Figure 2.9: Part(a) Bifurcation diagram for $\mu = 0.1$ for 50-oscillator system. Part(b),(c) Two different stable solutions at $(\mu = 0.1, k = 1.6)$.

In Fig. 2.10 part (a), bifurcation diagrams of $\mu = 0.4, 0.2, 0.1, 0.025$ are shown for a 50-oscillator system. For each value of μ, as k increases from 0, the solution of (2.1) keeps stable when $k < k^*(\mu)$ which is on pitchfork bifurcation curve as shown in Fig. 2.7(a). For small μ ($\mu < \mu_c$), the pitchfork bifurcation is supercritical. At the bifurcation point, the stable solution branch separates in to three branches, one unstable solution branch and two stable solution branch as shown in Fig 2.7. For $\mu > \mu_c$, the pitchfork is subcritical. The stable solution branch separates into three unstable solution branches. For any value of $\mu > 0$, all the stable branches turn back when touching saddle-node bifurcation as unstable branches to either 0 or $-\pi/2$. The unstable branch also turns back as unstable branch to $-\pi/2$ or $-\pi$ as shown in Fig 2.10 part (b). They turn back as negative value because the vertical coordinates is value of θ_{25} which is on the left half part among 50 oscillator system. Fig. 2.10 part (b) is a bifurcation diagram shown on a greater domain of parameter k. Every bifurcated branch turns back at certain value of k. The smaller value of μ is, the greater k is needed for unstable branch to turn back.

15
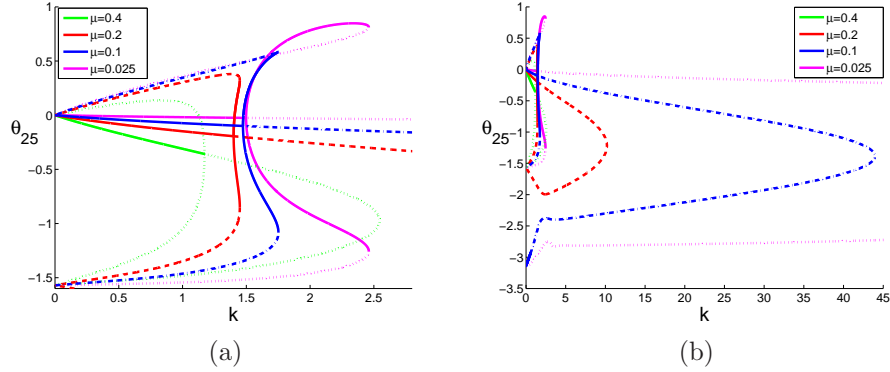
Figure 2.10: Part (a): Bifurcation Diagrams for $\mu = 0.4, 0.2, 0.1, 0.025$ for 50-oscillator system. Part (b): Overview of the bifurcation diagrams on a greater range of k.

In Fig. 2.11 part (a), the bifurcation diagram for $\mu = 0$ is shown. The solution is stable when $k < k^*(\mu) = 1.5$. At $k = 1.5$, the solution bifurcates into two stable branches and one unstable branch. In part (c) and (d), two stable solution fronts are shown. In Fig. 2.11 part (b), we can see the stable branches turn to unstable around $k = 15.17$. Also from part (b), we can see the periodicity of π. From the structure of Eq. (2.1), If $(\theta_1, \ldots, \theta_{50})$ is the solution to the system, then $(\theta_1 \pm n\pi, \ldots, \theta_{50} \pm n\pi)$ is also a solution for any value of μ. The unstable branches continue and no turning back is observed. To check the unstable solution on two bifurcated branches, the solution at $k = 50, 100, 200, 400$ and 600 are shown and compared in part (e) and (f). On one branch, the solution becomes split states $(-\pi/2, \ldots, -\pi/2, 3\pi/2, \ldots, 3\pi/2)$ as k increased to 600. On the other branch, the solution becomes $(\pi/2, \pi/2, ..., \pi/2, \pi/2)$ as k increases to 600.

To examine the difference of solution from different oscillator numbers, results of 10-oscillator and 50-oscillator are compared at $\mu = 0.4$. The difference of value of θ_{25} and θ_5 is $o(10^{-4})$ across value of k. This shows that the difference is very small.

16
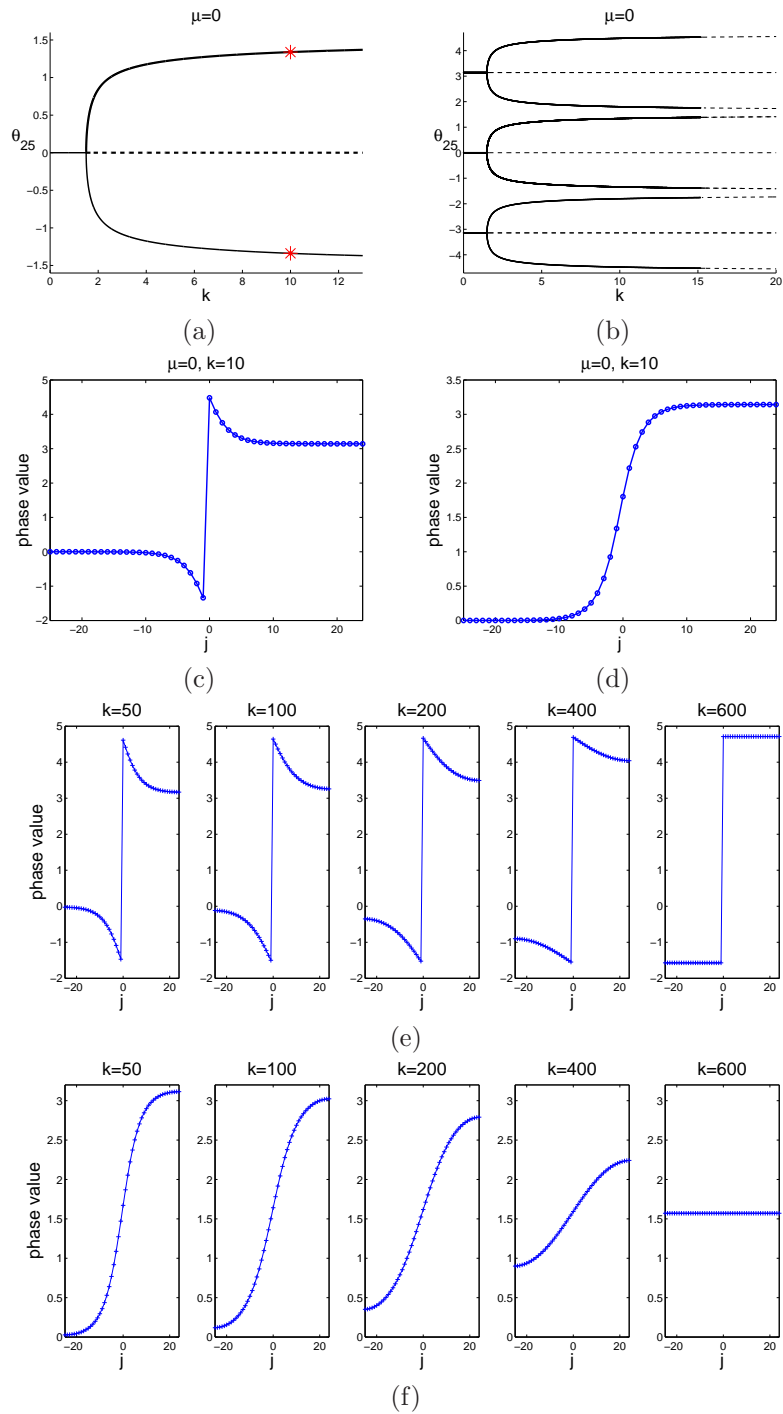
Figure 2.11: (a) Bifurcation diagram at $\mu = 0$. (b) Overview of bifurcation diagram on a greater range of k. All the stable branches change to unstable around $k = 15.17$. From observation, the period of the solution is π. (c), (d) Two different stable standing wave solution at $(\mu = 0, k = 10)$ (e) Front change of standing wave solution with increase of k.

17

2.4 Numerical methods for bifurcation

To trace out different bifurcated branches at bifurcation curves, a Pseudo-Arclength algorithm is used. As explained in [27], in Pseudo-Arclength continuation method, arc length is approximated with line on the tangent space. For a step Δs along the tangent vector (red line in Fig. 2.12) at the current pointer as a predictor (soft dot in Fig. 2.12), use Newton's method to find the corrector (filled dot in Fig. 2.12) on the curve. At the bifurcated point, the direction of stable branch is orthogonal to the original branch direction. We can get this direction from the vector in the null space of the Jacobian matrix. In practice, the direction is got through Singular Value Decomposition (SVD) of J. Suppose $J = U\Sigma V^*$. The columns of V which correspond to zero singular values form an orthonormal basis for the null space of J. As diagonal singular value of Σ in the matlab SVD result is listed in decreasing order. The last element on diagonal line of Σ is vanishing to 0. So the last column of V is in null space. This is what we used as a direction vector in practice.

$$J = \begin{pmatrix} F_\theta & F_k \\ \theta'_n & k'_n \end{pmatrix} \tag{2.2}$$

Through switching the direction at the bifurcation point, we can find the other branches and trace out the bifurcation diagram. The following Eq. (2.3) is equation showing Pseudo-Arclength continuation [27]. We solve Eq. (2.4) and Eq. (2.5) for $(\Delta\theta_{n+1}, \Delta k_{n+1})$ and direction vector $(\theta'_{n+1}, k'_{n+1})$.

To get initial value , we solved the ODE system Eq. (2.1) at $k_0 = k$ and $k_1 = k + \Delta k$ ($\Delta k = 0.00000001$) . Then we can get $\theta'_0 = (\theta_1 - \theta_0)/\Delta s$ and $k'_0 = (k_1 - k_0)/\Delta s$. Thus we have the initial direction vector. Then with Newton method, we can iteratively update θ_n, k_n [27].

$$F(\theta_{n+1}, k_{n+1}) = 0$$

$$(u_{n+1} - u_n)\theta'_n + (k_{n+1} - k_n)k'_n - \Delta s = 0 \tag{2.3}$$

$$\begin{pmatrix} F_\theta & F_k \\ \theta'_n & k'_n \end{pmatrix} \begin{pmatrix} \Delta\theta_{n+1} \\ \Delta k_{n+1} \end{pmatrix} = - \begin{pmatrix} F(\theta_{n+1}, k_{n+1}) \\ (\theta_{n+1} - \theta_n)\theta'_n + (k_{n+1} - k_n)k'_n - \Delta s) \end{pmatrix} \tag{2.4}$$

Then solve next director vector.

$$\begin{pmatrix} F_\theta & F_k \\ \theta'_n & k'_n \end{pmatrix} \begin{pmatrix} \theta'_{n+1} \\ k'_{n+1} \end{pmatrix} = \begin{pmatrix} 0 \\ 1 \end{pmatrix} \tag{2.5}$$
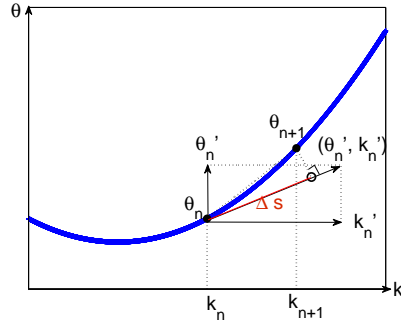
Figure 2.12: As shown in [27], Pseudo-Arclength continuation illustration. (θ'_n, k'_n) is the direction vector. (θ_{n+1}, k_{n+1}) is the solution at the (n+1) step. Δs is the one step along the director vector.

CHAPTER 3

ONE DIMENSIONAL TRAVELING WAVE

As shown in Chapter 2, standing waves are unstable in region C of Fig. 2.1. Fig. 2.3 shows an unstable standing wave which actually is a traveling wave. We begin to study traveling wave solutions in this chapter. We set up the advance-delay differential equation (3.4) based on the ODE system (2.1). To solve the traveling wave equation and velocity, we use Newton's method with additional pinning condition. The forward difference is applied in the space discretization. For comparison, centered difference method is also used and the results are summarized in Chapter 6. From the ansatz of the advance delay differential equation set up, the solution from the advance delay differential equation is the time expansion of ODE solution at different time. The ODE system solution and speed are encoded in the advance-delay differential equation. The stability of traveling wave solution is analyzed. The front shape of the traveling wave solution to ODE is periodic with a period of reciprocal of speed $(1/c)$. We solve the traveling wave speed from ODE system (2.1) which shows consistency with the speed solved from advance-delay differential equation.

3.1 Traveling wave equation set up

We consider the infinite chain of oscillators

$$\dot{\theta}_j = k[H(\theta_{j-1} - \theta_j) + H(\theta_{j+1} - \theta_j)] + f(\theta_j), \quad j \in \mathbb{Z}. \tag{3.1}$$

We start by seeking a solution of this system in the form $\theta_j(t) = \Theta(z, \tau)$, where $z = j - ct$ is a traveling wave coordinate with wave velocity c and $\tau = t$, such that

$\Theta \to 0$ and $\Theta \to \pi$ when $z \to -\infty$ and ∞, respectively, or vice versa. Substitution of this ansatz into (3.1) leads to the partial differential advance-delay equation (co-traveling frame PDE) of the form

$$\Theta_\tau - c\Theta_z = k[H(\Theta(z+1,\tau) - \Theta(z,\tau)) + H(\Theta(z-1,\tau) - \Theta(z,\tau))] + f(\Theta(z,\tau)).$$

$$(3.2)$$

Traveling wave solutions of (3.1),

$$\theta_j(t) = \phi(z), \quad z = j - ct, \tag{3.3}$$

are stationary solutions of (3.2) and satisfy the advance-delay differential equation

$$-c\phi'(z) = k[H(\phi(z+1) - \phi(z)) + H(\phi(z-1) - \phi(z))] + f(\phi(z)). \tag{3.4}$$

Since every translate of the traveling wave solution is also a solution, the additional pinning condition $\phi(0) = \pi/2$ is imposed on the nonlinear system in order to fix (i.e., pin) the traveling wave. This condition uniquely identifies the solution, as well as the corresponding velocity c.

3.2   Examples of traveling wave solutions

We start by considering solutions of the traveling wave Eq. (3.4) satisfying $\phi(0) = \pi/2$, $\phi(z) \to \pi$ as $z \to \infty$, $\phi(z) \to 0$ as $z \to -\infty$. Eq. (3.4) is discretized in the interval $[-25, 25]$ with a forward difference approximation of the derivative in the left hand side (for comparison purposes, a centered difference scheme was also used. The results are summarized in Chapter 6). The middle grid point is fixed to satisfy the pinning condition $\phi(0) = \pi/2$, and the speed c is added as a variable. We solve the resulting system using Newton's method for the traveling wave $\phi(z)$ and its velocity

c, thus identifying numerically exact (at least up to a prescribed tolerance of 10^{-12} in the discretized system) solutions.

Examples of traveling wave solutions are shown in Fig. 3.1 corresponding to different values of the parameters k and μ, characterizing the intersite coupling. In Fig. 3.1, the traveling wave solution $\phi(z)$ (solid line) is shown at $(k = 2.25, \mu = 0.5)$, $(k = 1.5, \mu = 0.5)$ and $(k = 1.1, \mu = 0.5)$. By solving Eq. (3.4), we also get velocities $c = 0.8123$, $c = 0.5368$ and $c = 0.2382$ respectively. These are in excellent agreement with the velocities $c = 0.8124$, $c = 0.5367$ and $c = 0.2377$, respectively, obtained from the solution of the ODE system (2.1) initialized by the traveling wave. The details of velocity calculation from ODE system are introduced in the last section of this chapter.

In Fig. 3.2, stability of the traveling wave solution $\phi(z)$ is analyzed by computing the spectrum of the Jacobian matrix obtained by linearizing Eq. (3.2) about $\phi(z)$ with a forward difference approximation of the spatial derivative. Fig. 3.2 indicates that the eigenvalues of the linearization Jacobian of the PDE (3.2), evaluated at this solution, have only negative real parts, implying the linear (spectral) stability of the traveling wave solution as a stationary solution of Eq. (3.2). Observe that as k decreases at fixed μ, the velocity c of the traveling wave decreases, and the eigenvalues shown in Fig. 3.2 move closer to the imaginary axis as well. Nonetheless, the obtained eigenvalues in all three cases remain in the left half-plane $\text{Re}\lambda < 0$, suggesting that the relevant wave is stable as a stationary solution of the co-traveling wave PDE (3.2).

We check stability of the obtained solutions by solving the advance-delay PDE (3.2) initialized at the traveling wave. Fig. 3.3 show space-time evolution of the solution of the advance-delay PDE (3.2) with the initial condition $\Theta(z, 0) = \phi(z)$. The solution is obtained with the discretization grid used to obtain the traveling wave $\phi(z)$. As expected, the results show that $\phi(z)$ is a stationary solution of Eq. (3.2) confirming the robust evolution of this steady state. The time evolution of the PDE
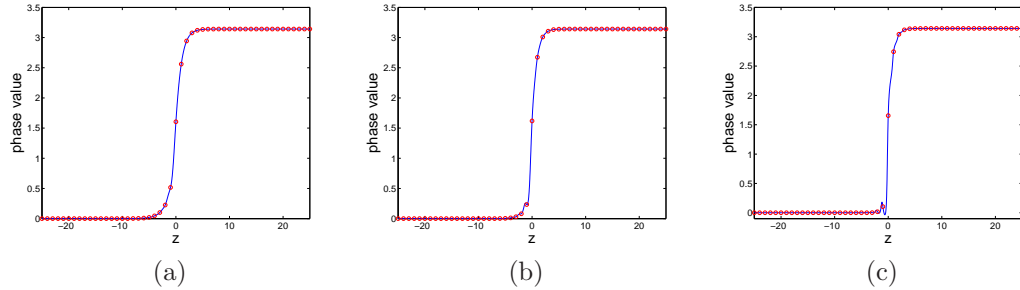
Figure 3.1: Traveling wave solution (solid curve) $\phi(z)$ of (3.4) at $\mu = 0.5$, $k = 2.25$, $k = 1.5$ and $k = 1.1$. The velocities are $c = 0.8123$, $c = 0.5368$ and $c = 0.2382$. The initial condition (circles) $\theta_j(0) = \phi(j)$ on the lattice is initial value for the ODE simulations shown in Fig. 3.4.

(3.2) is accomplished using the classical fourth order Runge-Kutta method. For the space discretization of PDE, second order forward difference is applied.

We also check stability of the obtained solutions by solving the ODE system (2.1). In Fig. 3.4, we show the space-time evolution of the solution of the ODE system (2.1) with $N = 2n + 1 = 51$ oscillators initialized by the traveling wave solution $\phi(z)$ evaluated at the integer values of z, $\theta_j(0) = \phi(j)$, $j = -25, \ldots, 25$. The ODE system (2.1) is accomplished using the classical fourth order Runge-Kutta method. We anticipate that the spectral stability of the solution for the PDE implies the dynamical stability of the traveling wave as the solution of the ODE system (2.1), as confirmed by our simulations. However, the general demonstration of such a connection is, to the best of our knowledge, an intriguing open problem in analysis.

3.3 Existence and velocity of traveling waves solution for the chain

We now explore more systematically the existence and the speed of traveling waves in the (μ, k) parameter plane. The existence and speed results for sufficiently small μ $(0 \leq \mu \leq 1.5)$ are summarized in Fig. 3.5(a), which shows the contour plot of velocity

(a)   (b)   (c)
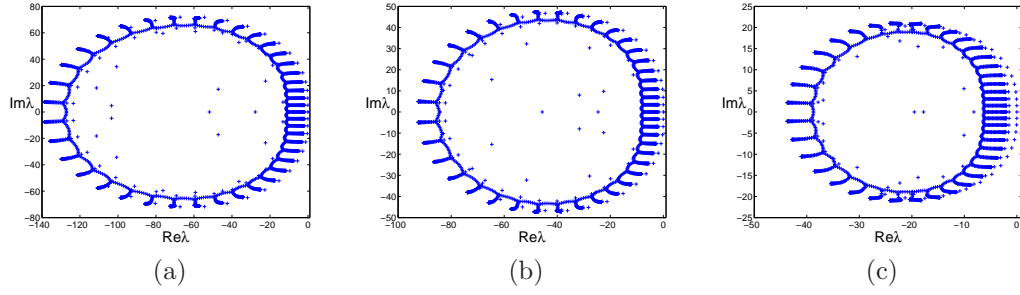
Figure 3.2: Eigenvalues of the Jacobian of the linearization of the co-traveling frame PDE (3.2) around the stationary solution $\phi(z)$.

(a)   (b)   (c)
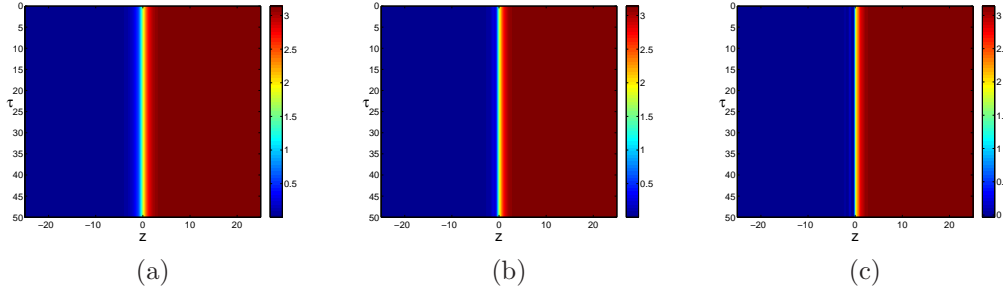
Figure 3.3: The space-time evolution of the solution of PDE (3.2) with the stationary state as the initial condition $\Theta(z,0) = \phi(z)$.

(a)   (b)   (c)
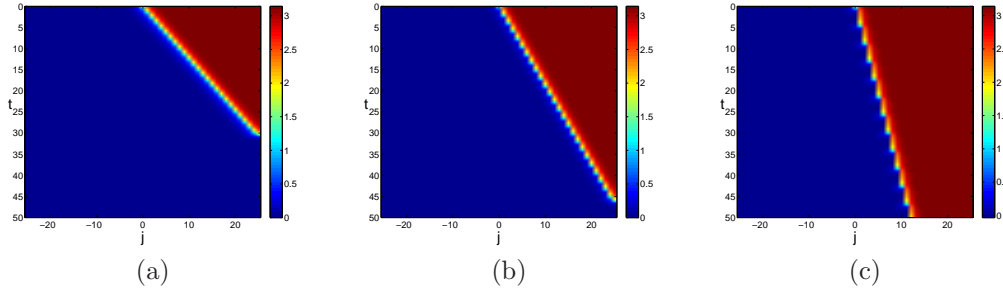
Figure 3.4: The space-time evolution of the solution of ODE (2.1) with initial condition $\theta_j(0) = \phi(j)$ shown by circles in Fig. 3.1.

24

of the traveling wave computed at different μ and k using Eq. (3.4) and complements the steady state analysis of [6] shown in Fig. 2.1. For comparison, pitchfork (yellow) and saddle-node (red) bifurcation curves for a 51-oscillator chain are also included. These bifurcation curves are the same with the ones in Fig. 2.7. While we perform our computations in a finite chain, having examined chains of different sizes, we expect our principal conclusions to persist (essentially without modification) for the case of the infinite chain. On the flip side, we can identify traveling waves only in region C, while below it their speed degenerates to 0, leading to standing waves (split-state equilibria), in agreement with the findings of [6] for the finite chain case (and our discussion of standing wave states above).

We now explore this comparison in more quantitative detail in Fig. 3.5(b). Here the open circles mark the curve above which numerical simulations of ODE system (2.1) yield stable traveling waves. To obtain these points, we fixed μ and solved (3.4) for the traveling wave solution $\phi(z)$ and its velocity at (μ, k) starting with k just above the bifurcation curves and then progressively decreasing its value. To verify the velocity of the traveling wave at given (μ, k), we then used $\theta_j(0) = \phi(j)$ as initial conditions in the simulations of (2.1) and computed the velocity of the propagating front. The open circles were obtained by finding the values of k where the traveling wave solution has zero velocity up to the numerical error in both methods. The comparison strongly suggests that the disappearance of standing wave solutions of [6] gives rise to the traveling wave solutions analyzed here.

The isocontours associated with different velocities, shown in Fig. 3.5(a), illustrate how the velocity c of traveling waves, as obtained from the PDE, depends on the two parameters μ and k. To complement these results with a monoparametric visualization, we also show some plots of velocity $c(k, \mu)$ at fixed μ in Fig. 3.6(a),(b) and of velocity c as a function of μ at fixed k in Fig. 3.6(c),(d). These curves show that the

25

(a)   (b)
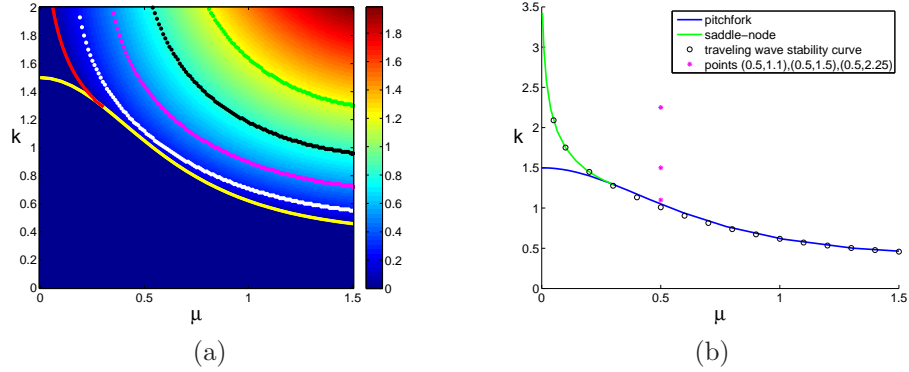
Figure 3.5: (a) Contour plot of the velocity c of the traveling waves in the (μ, k) plane obtained by solving Eq. (3.4) and isocontours of $c = 0.25$ (white), $c = 0.5$ (magenta), $c = 0.8$ (black) and $c = 1.2$ (green), shown together with the pitchfork (yellow) and saddle-node (red) bifurcation curves obtained for the equilibrium states of the 51-oscillator chain. (b) The curve (open circles) where the traveling waves have (almost) zero velocity nearly coincides with the saddle-node (green) and pitchfork (blue) bifurcation curves; parameter values used in Figs. 3.1, 3.2, 3.3 are also shown (magenta dots).

velocity increases with k and μ. As the velocity decreases, these curves approach the region containing the standing waves.

3.4 Periodically changed wavefront shape

Note that in the contour plot of the traveling wave in Fig. 3.4, it travels along a line with slope c. A sawtooth of size $1/c$ could be observed in the contour plot. The traveling wave ansatz (3.3) implies that $\theta_j(t) = \theta_{j+1}(t + 1/c)$ for any integer j, meaning that the phase value $\theta_j(t)$ is periodic (modulo shifts) with a period of $1/c$. This shows that when the wave is traveling, the wave front shape will change periodically. The "integer spaced" fronts have the same shape. Fig. 3.7 panel (a) shows traveling wave fronts at $k = 2.25$, $\mu = 0.5$ every $t = 0.5$ starting from $t = 0$. The wave fronts at different time are different from observation. In panel (b), (c) and (d), integer spaced wave fronts are shown starting from $t = 0, 0.5$ and 2 respectively. The space between two adjacent wavefronts is 1. All these panels show agreement of
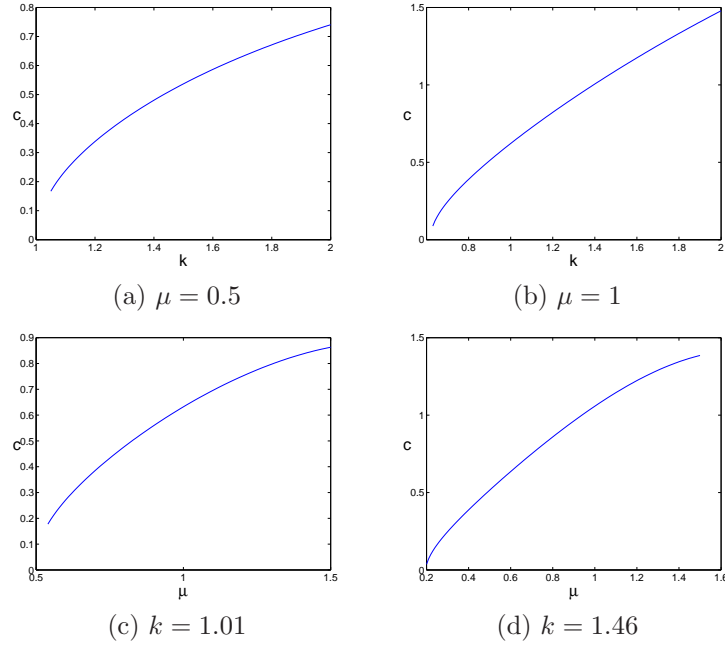
Figure 3.6: Velocity c as a function of k at fixed μ (panels a and b) and as a function of μ at fixed k (panels c and d).

the periodic phase value with period $1/c$. To observe clearly, only the middle part of the wavefronts are enlarged and shown in the figure. $t = 0.5$ is selected as time step because it is a proper one to observe the difference in wavefronts. There would be more front shapes observed if the time step is finer.

Similar plots are made in Fig. 3.8 for $\mu = 0.5$, $k = 1.5$. Panel (a) is the wave front shown with $\Delta t = 0.5$. Part (b),(c) and (d) are plots of wave fronts with integer spaced starting at $t = 0, 1$ and 2.5. In Fig. 3.9, wave front for $\mu = 0.5$, $k = 1.1$. Panel (a) is the wave front every $t = 1$. Part (b),(c) and (d) are plots of wave fronts with integer spaced starting at $t = 0, 1$ and 3. All the plots show that the wave fronts is periodic with period $1/c$.

(a) $k = 2.25$, $t_0 = 0$

(b) $k = 2.25$, $t_0 = 0$

(c) $k = 2.25$, $t_0 = 0.5$

(d) $k = 2.25$, $t_0 = 2$
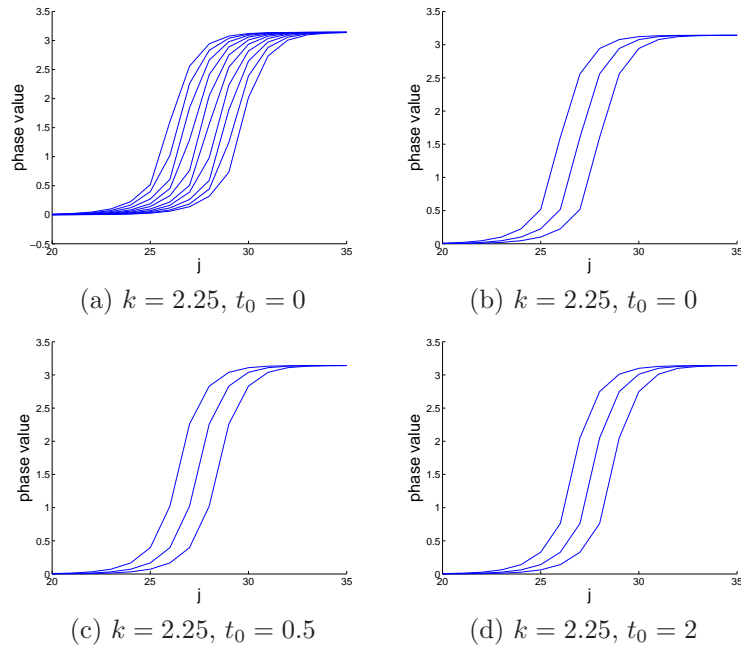
Figure 3.7: Evolution in ODE at $\mu = 0.5$, $k = 2.25$. Subfigure(a), plot of wave fronts every 0.5 time unit starting from $t = 0$. The fronts are 'integer spaced' in part b, c, and d. Subfigure(b), plot of wave fronts with starting time $t = 0$. Subfigure(c), plot of wave fronts with starting time $t = 0.5$. Subfigure(d), plot of wave fronts with starting time $t = 2$.

(a) $k = 1.5$, $t_0 = 0$

(b) $k = 1.5$, $t_0 = 0$

(c) $k = 1.5$, $t_0 = 1$

(d) $k = 1.5$, $t_0 = 2.5$
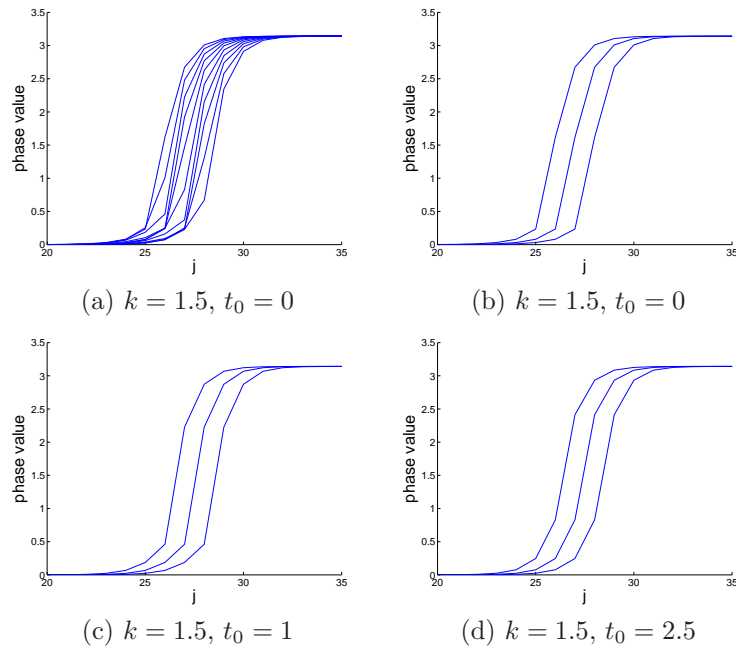
Figure 3.8: Evolution in ODE at $\mu = 0.5$, $k = 1.5$. Subfigure(a), plot of wave fronts every $t = 0.5$ starting from t=0. The fronts are 'integer spaced' in part b, c, and d. Subfigure(b), plot of wave fronts with starting time $t = 0$. Subfigure(c), plot of wave fronts with starting time $t = 1$. Subfigure(d), plot of wave fronts with starting time $t = 2.5$.

(a) $k = 1.1$, $t_0 = 0$

(b) $k = 1.1$, $t_0 = 0$

(c) $k = 1.1$, $t_0 = 1$

(d) $k = 1.1$, $t_0 = 3$
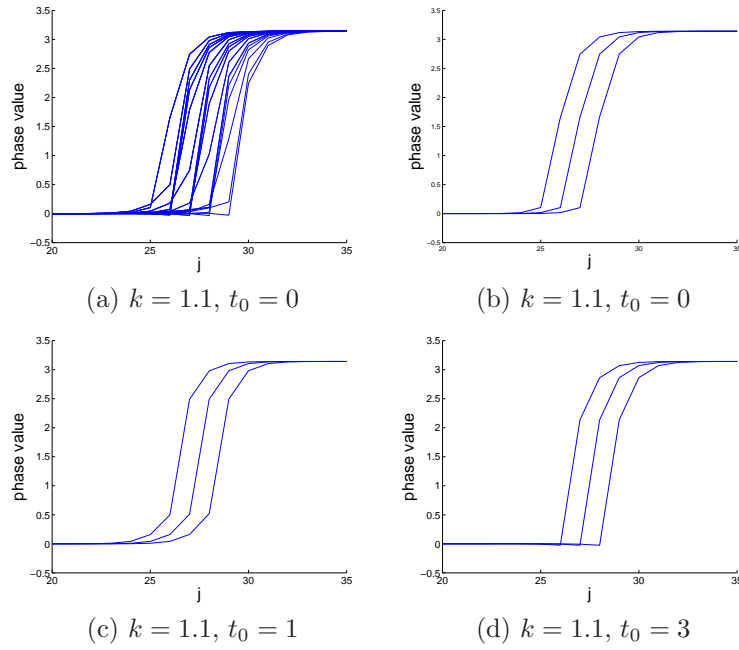
Figure 3.9: Evolution in ODE at $\mu = 0.5$, $k = 1.1$. Subfigure(a), plot of wave fronts every $t = 1$ starting from t=0. The fronts are 'integer spaced' in part b, c, and d. Subfigure(b), plot of wave fronts with starting time $t = 0$. Subfigure(c), plot of wave fronts with starting time $t = 1$. Subfigure(d), plot of wave fronts with starting time $t = 3$.

3.5 Connection between advance-delay differential equation and ODE system solutions

In this section, we show the connection between steady state solution of the PDE and dynamics of the ODE system. From the ansatz of traveling wave equation set up $\theta_j(t) = \phi(z)$, $z = j - ct$, when $t = 0$, we have $z = j$ and thus the value of $\phi(z)$ at integer point is initial value of the ODE system. This is what we analyzed in the previous sections. Here we will explore more. For different values of t, for example $t = 0.01$, we have $z_1 = j - ct = j - 0.01c$. Then $\theta_j(0.01) = \phi(z_1)$ corresponds to value of the jth oscillator at time 0.01. In this way, we can connect the steady state solution of the PDE and the dynamics of the ODE system. All the dynamics in the ODE traveling wave is encoded in the solution of advance-delay differential equation.

In Fig. 3.10 part (a), for $\mu = 0.5$ and $k = 2.25$, we extract the solution of Eq. (3.4) at the integer points $\phi(j)$. We evolve with time step $\Delta t = 0.01$ in the ODE. At each step we plot $(j - ct, \theta_j(t))$ until $t = 1.23$ which is approximately the period $1/c$. These plots are compared with $(z, \phi(z))$ in the bottom panel of Fig. 3.10 part (a). They are visually the same. The same comparison is done with $\mu = .5$ and $k = 1.5$ in Fig. 3.10 part (b) and $\mu = .5$ and $k = 1.1$ in Fig. 3.10 part (c). The agreement in top and bottom panels are clear and this shows that the information of solutions from two methods are encoded into each other.

In addition we solve the PDE for $\mu = 0.5, k = 1.1$ for 2000, 4000, 6000, 8000 points and there is no change in the profile. This shows that oscillatory doesn't come from the numerical error.

3.6 Calculation of the velocity of the traveling wave from ODE

The speed of the front is numerically calculated as follows. We choose an integer grid point k and place the right-traveling front to its left, near an integer grid point
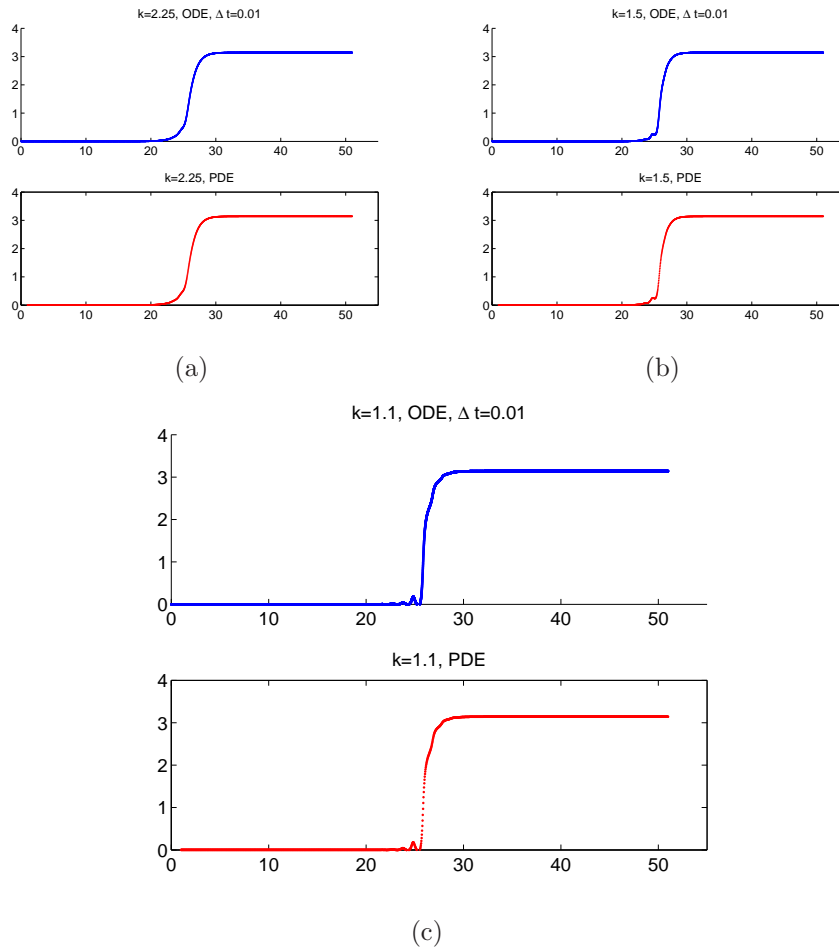
Figure 3.10: The figures show the connection between traveling wave steady state solution of the PDE (3.2) and the solution of the ODE system. For each comparison of $k = 2.25$, $k = 1.5$ and $k = 1.1$, top panel is constructed from the solution to ODE system at t=0, 0.01, 0.02 until $1/c$. Shift the solution $z = j - ct$ and put the solutions together. Bottom panel is the traveling wave solution from advance-delay differential equation. For each comparison, good agreement could be observed.

m with $m < k$ such that $|\theta_m - \frac{\pi}{2}| < |\theta_j - \frac{\pi}{2}|$ for all j. Then θ is close to $\frac{\pi}{2}$ at the integer grid point m than at any other integer grid point. The front is allowed to evolve using the standard fourth order Runge-Kutta method. We count the number of time steps p such that $|\theta_k - \frac{\pi}{2}| < |\theta_j - \frac{\pi}{2}|$ for all j. The total time where $\theta = \frac{\pi}{2}$ lies in the interval $[k - \frac{1}{2}, k + \frac{1}{2}]$ is denoted as $p\Delta t$ where Δt is the Runge-Kutta time step, and the approximation to the speed is then $\frac{1}{p\Delta t}$. If $p = 0$, meaning that the front never entered the interval $[k - \frac{1}{2}, k + \frac{1}{2}]$, then the speed is zero, assuming that the method was allowed to run long enough. Comparing with Fig. 3.5 part (b), the black circle denote where the traveling wave speed degenerates to 0.

In Fig. 3.11, the process of speed calculation is shown. Part (a) show that how the points within region $[k - \frac{1}{2}, k + \frac{1}{2}]$ are counted. The closest phase value θ_j to $pi/2$ is colored in red and black. The closest integer grid points to the red solid points are k. The value j of red solid points lie between $k - \frac{1}{2}$ and $k + \frac{1}{2}$. The closest integer grid points to the black solid points are $k - 1$ or $k + 1$. The total number of the red solid points are p. The estimated speed is calculated by $\hat{c} = \frac{1}{p\Delta t}$. Fig. 3.11 part (b) shows the error in observation and calculation.

The error of the velocity in the calculation is $O(\Delta t)$. The error of observation comes from that the distance traveled during time $p\Delta t$ which is not exact 1. It is between $(p - 1)\Delta t$ and $(p + 1)\Delta t$ as shown in Fig. 3.11 part (b). As a result, $(p - 1)\Delta t < \frac{1}{c} < (p + 1)\Delta t$. Then we have $\frac{1}{(p+1)\Delta t} < c < \frac{1}{(p-1)\Delta t}$. In calculation the speed is estimated by $\hat{c} = \frac{1}{p\Delta t}$. The error is $(\frac{1}{p+1} - \frac{1}{p})\frac{1}{\Delta t} < error = c - \hat{c} < (\frac{1}{p-1} - \frac{1}{p})\frac{1}{\Delta t}$. Then the error is within range $[\frac{-1}{p(p+1)\Delta t}, \frac{1}{p(p-1)\Delta t}]$ which is $O(\frac{1}{p^2\Delta t})$. Here $\frac{1-2\Delta tc}{(p-1)\Delta t} < c < \frac{1}{(p-1)\Delta t}$. As a result $\frac{1-2\Delta tc}{c\Delta t} < p - 1 < \frac{1}{c\Delta t}$. As a result, $p = O(\frac{1}{\Delta t})$. So $O(\frac{1}{p^2\Delta t}) = O(\Delta t)$.
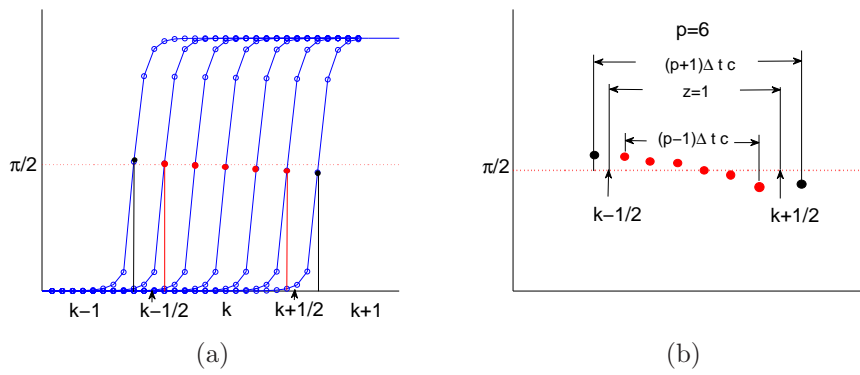
Figure 3.11: Part (a). Figure explanation of speed calculation $\hat{c} = \frac{1}{p\Delta t}$ from the ODE system. The total number of red solid dots is p. The closest integer grid points to the red solid points is k. Part (b). Figure explanation of error in the speed estimation.

CHAPTER 4

BACKGROUND INSTABILITY

In Chapter 2 and Chapter 3, we discuss the stability of the standing wave solution and traveling wave solution on the region $\mu \in [0, \pi/2]$. In this chapter, we analyze the stability of the background. We give a detailed discussion on the symmetry and periodicity in standing wave and traveling wave solutions. In particular, we prove that the system is symmetric about $\mu = (2k+1)\pi$ and periodic in μ with period 2π. Also we introduce and explore the frontal instability.

4.1   Background instability

We now discuss an important aspect of the obtained spectral pictures (e.g. the ones shown in Fig. 3.2 that concerns stability of the background state with $\Theta_0 = 0$ or $\Theta_0 = \pi$. Our solutions clearly have support on both of these states, so the spectrum of these homogeneous states should be mirrored within that of our (standing or traveling) waves. Substituting $\Theta(z, \tau) = \Theta_0 + \epsilon v(z, \tau)$ in Eq. (3.2), where ϵ is a small parameter, and linearizing about Θ_0, one obtains the following linear advance-delay partial differential equation with constant coefficients for $v(z, \tau)$:

$$\epsilon v_\tau - c\epsilon v_z = k[H(\Theta_0 + \epsilon v(z+1,\tau) - \Theta_0 - \epsilon v(z,\tau))$$

$$+ H(\Theta_0 + \epsilon v(z-1,\tau) - \Theta_0 - \epsilon v(z,\tau))] - \sin(2(\Theta_0 + \epsilon v(z,\tau)))$$

$$= k[H(\epsilon v(z+1,\tau) - \epsilon v(z,\tau)) + H(\epsilon v(z-1,\tau) - \epsilon v(z,\tau))] - \sin(2\Theta_0 + 2\epsilon v(z,\tau))$$

$$= k[\sin(\epsilon v(z+1,\tau) - \epsilon v(z,\tau) + \mu) - \sin(\mu) + \sin(\epsilon v(z-1,\tau) - \epsilon v(z,\tau) + \mu)$$

$$- \sin(\mu)] - \sin(2(\Theta_0 + \epsilon v(z,\tau)))$$

$$= k[\sin(\mu) + \epsilon(v(z+1,\tau) - v(z,\tau))\cos(\mu) - \sin(\mu) + \sin(\mu)$$

$$+ \epsilon(v(z-1,\tau) - v(z,\tau))\cos(\mu) - \sin(\mu) + O(\epsilon^2)]$$

$$- \sin(2\Theta_0) - \cos(2\Theta_0)(2\epsilon v(z,\tau))$$

$$= k\epsilon\cos(\mu)[v(z+1,\tau) - 2v(z,\tau) + v(z-1,\tau)] - 2\epsilon v(z,\tau)$$

$$(4.1)$$

Then we have

$$v_\tau - cv_z = k\cos(\mu)[v(z+1,\tau) - 2v(z,\tau) + v(z-1,\tau)] - 2v(z,\tau) \qquad (4.2)$$

Seeking solutions of (4.2) in the form $v = e^{\lambda\tau}e^{ipz}$ for real p, we have

$$\lambda e^{\lambda\tau}e^{ipz} - icpe^{\lambda\tau}e^{ipz} = k\cos(\mu)[e^{\lambda\tau}e^{ip(z+1)} - 2e^{\lambda\tau}e^{ipz} + e^{\lambda\tau}e^{ip(z-1)}] - 2e^{\lambda\tau}e^{ipz}$$

$$\lambda - icp = k\cos(\mu)[e^{ip} - 2 + e^{-ip}] - 2$$

$$\lambda = k\cos(\mu)[\cos(p) + i\sin(p) - 2 + \cos(p) - i\sin(p)] - 2 + icp \qquad (4.3)$$

$$\lambda = 2k\cos(\mu)(\cos(p) - 1) - 2 + icp$$

$$\lambda = 2k\cos(\mu)(-2\sin^2(p/2)) - 2 + icp$$

As a result, we have the formula for λ,

$$\lambda = -2(2k\cos(\mu)\sin^2(p/2) + 1) + icp. \qquad (4.4)$$

The equilibrium state $\Theta(z,\tau) \equiv \Theta_0$ is unstable when Re$\lambda > 0$, i.e. when

$$k \cos(\mu) < -\frac{1}{2 \sin^2(p/2)}$$

for some real p. Since $k > 0$, this can happen for example at large enough k. More precisely, the background solution is always unstable for

$$k > \frac{1}{2} |\sec(\mu)|, \quad \cos(\mu) < 0. \tag{4.5}$$

Additionally, since (4.4) implies that $\mathrm{Re}\lambda = -2(2k \cos(\mu) \sin^2(p/2)+1)$ and $\mathrm{Im}\lambda = cp$, these eigenvalues determine the following locus of points in the spectral plane:

$$\mathrm{Re}\lambda = -2 \left\{ 2k \cos(\mu) \sin^2 \left(\frac{\mathrm{Im}\lambda}{2c} \right) + 1 \right\}, \tag{4.6}$$

which should be traceable in the linearization spectra of the traveling waves considered here.

For $0 \leq \mu \leq \frac{\pi}{2}$, based on equation (4.6), the background is always stable, so any instability must come from the front itself. For example, Fig. 4.1a shows the eigenvalues of the Jacobian matrix associated with the traveling wave solution at $\mu = 0.5$ and $k = 1.5$. The eigenvalues are given for $n = 2001$, 4001 and 16001 nodes in our discretization of the co-traveling wave problem (3.2) on the interval $[-200, 200]$, with the step size $h = 400/(n-1)$. The eigenvalues of the linearized equation about the background solutions $\Theta_0 = 0$ and $\Theta_0 = \pi$ are given by Eq. (4.4). For these parameter values, we theoretically have the range of λ: $-7.27 \leq \mathrm{Re}\lambda \leq -2$. In Fig. 4.1 one can see a band of eigenvalues folding towards the imaginary axis as n increases. Zooming in on the region near the imaginary axis in Fig. 4.1(b), we see that the eigenvalues are converging to the background spectrum as the continuum limit is approached, as predicted. Similar results are found for the cases of $k = 2.25$ and $k = 1.1$. In Chapter 6, we explain further how the forward difference scheme we use results in the particular structure of the continuous spectrum of the problem
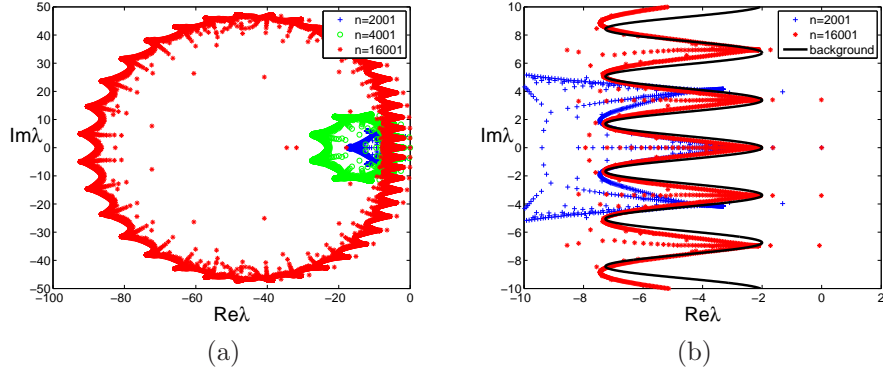
Figure 4.1: (a) The eigenvalues of the Jacobian for the traveling wave solution at $\mu = 0.5$, $k = 1.5$ discretized on the interval $[-200, 200]$ with $n = 2001$, 4001 and 16001 nodes. (b) The enlarged version of the $n = 2001$ and $n = 16001$ cases from (a), along with the continuous background spectrum curve given by Eq. (4.6), near the imaginary axis.

(inducing the parabolic shape observed in Fig. 4.1a) and how a centered difference scheme would affect the corresponding spectral and stability picture.

In the discussion above, we extended the analysis of the standing waves in [6] to traveling wave solutions and background instability. However, somewhat in line with the considerations in [6], this study until now was limited to $0 \leq \mu \leq 1.5$. We now extend our analysis to the region $0 \leq \mu \leq 3\pi/2$. So far, we have obtained stability curves (pitchfork and saddle-node) separating traveling and standing waves. Extending these notions to a broader μ-interval in the (μ, k) plane, we obtain the bifurcation curves for $0 \leq \mu \leq 3\pi/2$ as shown in Fig. 4.2. The method to obtain pitchfork curve is the same with the one on region $\mu \in [0, \pi/2]$ in Chapter 2. Below the curve, the standing waves are stable. Along with extended pitchfork we show the curves above which the background is unstable, according to the inequality (4.5) obtained above for the linearized problem. As shown in Fig. 4.2, the red curve is the background instability curve. The curve coincides with pitchfork curve on part of region II and III in Fig. 4.2.
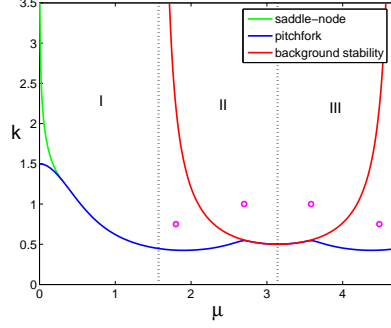
Figure 4.2: Extended pitchfork (blue) and saddle-node (green) bifurcation curves and the background instability curve (red). Magenta circles denote the parameter values where the stability of the traveling waves was probed via direct numerical computations.

To explore the stability of traveling wave solutions where they exist, we divide the parameter space into several regions corresponding to different intervals of μ. These are the μ regions I ($[0, \frac{\pi}{2}]$), II ($[\frac{\pi}{2}, \pi]$) and III ($[\pi, \frac{3\pi}{2}]$). In the regions II and III, we choose points (μ, k) and solve the traveling wave Eq. (3.4) for $\phi(z)$ and velocity c. Using the forward difference or in some cases the centered difference approximation yields convergence to the relevant solutions. As before, we then use the resulting traveling wave as initial data to solve the ODE system (2.1) in order to check its stability and visualize the resulting dynamics. To obtain the initial condition, we evaluate the traveling wave solution at 51 integer points, and then place it on a grid of 81 points by padding it with 0s on the left and πs on the right:

$$\theta_j(0) = \begin{cases} 0, & j = 1, \ldots, 15 \\ \phi(j - 15), & j = 16, \ldots, 66 \\ \pi, & j = 67, \ldots, 81. \end{cases}$$

The padding introduces a small perturbation of the initial curve, which, when the solution is unstable, initiates the instability. The points $(\mu, k) = (1.8, 0.75)$, $(2.7, 1)$,

$(2\pi - 2.7, 1)$, $(2\pi - 1.8, .75,)$(magenta circles in Fig. 4.2) are chosen as representative points from the regions II and III. The points $(\mu, k) = (2.7, 1)$ and $(2\pi - 2.7, 1)$ lie in the region where the background state was shown to be unstable, above the red curve in Fig. 4.2. Perturbed traveling waves for these points are shown in Fig. 4.3 and Fig. 4.4 respectively.

When $(\mu, k) = (2.7, 1) \in II$, the traveling wave is predicted to move to the right with speed $c = 0.2233$. In panel (a) of Fig. 4.3, the initial condition is shown. In panel (b), the solution is shown at time $t = 4$, when the perturbation of the unstable solution has caused the relevant dynamical instability to be manifested in the $\theta \approx 0$ part of the solution. In panel (c), the solution is shown at time $(t = 8.5)$, when the instability of the background is manifested at both ends of the domain. Finally, panel (d) gives the space-time contour plot up to time $t = 50$, clearly illustrating the destabilization of the background and where it is initiated.

In Fig. 4.4, when $(\mu, k) = (2\pi - 2.7, 1) \in III$, the front is predicted to move with speed $c = -0.2233$. The results are similar to the ones discussed above and observed in Fig. 4.3. Observe that the traveling wave solutions $\phi_1(z)$ at $(\mu, k) = (2.7, 1)$, shown in Fig. 4.3(a), and $\phi_2(z)$ in Fig. 4.4(a) at $(\mu, k) = (2\pi - 2.7, 1)$ exhibit the symmetry $\phi_2(z) = \pi - \phi_1(-z)$, and their velocities are equal in absolute value and opposite in sign. This symmetry is discussed in the following section. Importantly, in both cases the intervals where the padding is added, and hence slight perturbations are introduced, are exactly where the instability of the background initially manifests itself (in panels (b) and (c)) numerically.

Fig. 4.5(a) shows time snapshots of the solution of the ODE system (2.1) initialized by the traveling wave (solid blue curve) obtained from Eq. (3.4) at $(\mu, k) = (1.8, 0.75)$, which lies in the region II below the background instability curve. The space-time contour plot of the solution is shown in Fig. 4.5(b). The traveling wave is initially traveling to the right at the positive predicted velocity $c = 0.5493$. However, a frontal
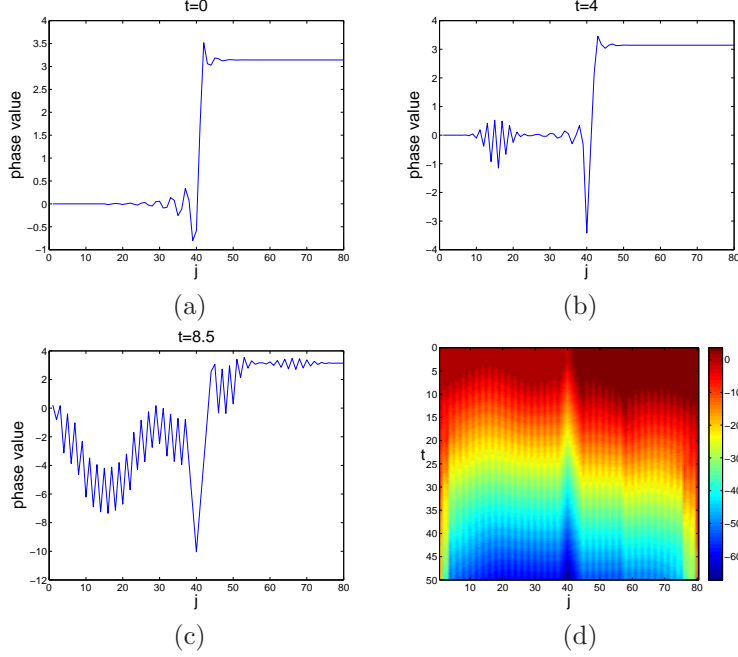
Figure 4.3: Unstable traveling wave at $(\mu, k) = (2.7, 1)$ with $c = 0.2233$: (a) Initial state $(t = 0)$ obtained from the solution of Eq. (3.4). (b) Solution of Eq. (2.1) at $t = 4$ where the left side of the solution, with $\theta_j \approx 0$, manifests destabilization. (c) Solution at $t = 8.5$ where the right side, with $\theta_j \approx \pi$, also shows destabilization. (d) Contour plot of space-time evolution until time $t = 50$. Here the color code represents θ_j values on the real line, rather than in $[0, 2\pi)$ mod 2π.

instability of the traveling wave leads to the formation of two fronts near $t = 7.28$ that can be seen at $t = 14.56$ (dashed-dotted green curve) and $t = 21.85$ (dotted magenta curve) in Fig. 4.5(a), as well as in the contour plot shown in Fig. 4.5b. Interestingly, the two fronts propagate in the opposite directions with the same speed as the initial unstable traveling wave. A similar instability is observed at $(\mu, k) = (2\pi - 1.8, 0.75)$ in region III in Fig. 4.6 . However, in this case the predicted velocity of the traveling wave is found to be negative, $c = -0.5493$. As explained below, this pair of solutions also exhibits the symmetry mentioned above for the solutions shown in Fig 4.3(a) and 4.4(a). In contrast to those solutions, which featured background instability, no instability of the background is observed in these two examples, and only the frontal instability arises.
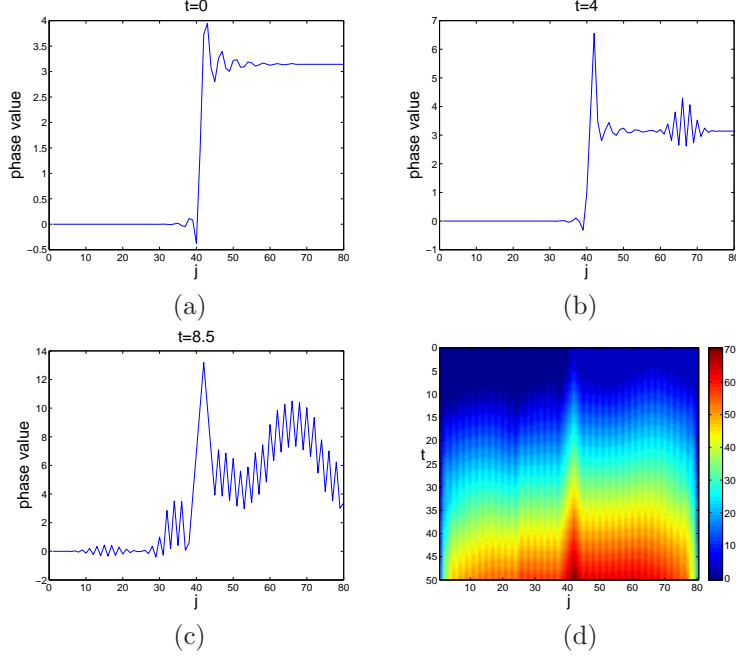
Figure 4.4: Unstable traveling wave at $(\mu, k) = (2\pi - 2.7, 1)$ with $c = -0.2233$: (a) Initial state $(t = 0)$ obtained from the solution of Eq. (3.4). (b) Solution of Eq. (2.1) at $t = 4$ where the right side of the solution, with $\theta_j \approx \pi$ imanifests destabilization. (c) Solution at $t = 8.5$ where the left side, with $\theta_j \approx 0$, suffers a similar effect. (d) Contour plot of space-time evolution until time $t = 50$. Again, the color code represents θ_j values on the real line, rather than in $[0, 2\pi)$ mod 2π.

4.2 Periodicity and symmetry of solution in μ

In this section, we prove that the stability of standing wave solution is 2π periodic in μ and symmetric about $\mu = \pi$. Thus implies that the bifurcation curve is symmetric about $\mu = \pi$ and periodic in 2π. Also we will show that the stability of traveling wave solution is periodic with 2π in μ and symmetric about $\mu = \pi$.

Because the function $H(\theta) = sin(\theta + \mu) - sin(\mu)$ is 2π periodic in μ, at (μ, k) and $(\mu + 2\pi, k)$, the ODE systems are the same and have the same solution θ. Thus supports that the solution of the ODE system is 2π periodic in μ. In the following two subsections, we show the symmetry of standing wave solution and traveling wave solution in μ. In each subsection, we introduce two solutions at one point (μ, k) of parameter space. One solution has front value π to 0 from the left to right and the
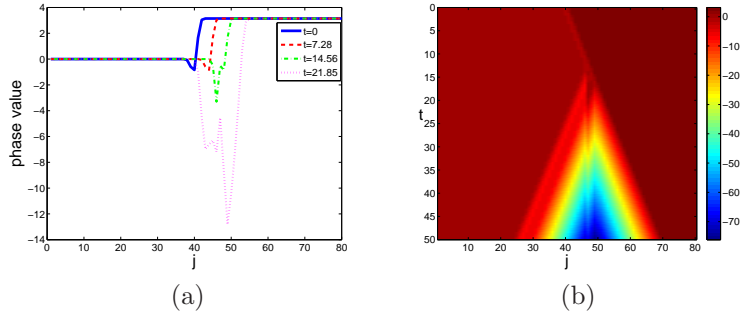
Figure 4.5: Unstable traveling wave at $(\mu, k) = (1.8, 0.75)$ with $c = 0.5493$: (a) Snapshots of the solution of Eq. (2.1) initialized at the traveling wave at times $t = 0$ (solid blue curve), 7.28 (approximate onset of instability, dashed red), 14.56 (dash-dotted green) and 21.85 (dotted magenta). (b) The contour plot of space-time evolution of the solution (with $\theta \in \mathbb{R}$) until time $t = 50$. The traveling wave becomes unstable after an initial transient propagation period and splits into two fronts propagating in the opposite directions with the same speed as the initial wave.
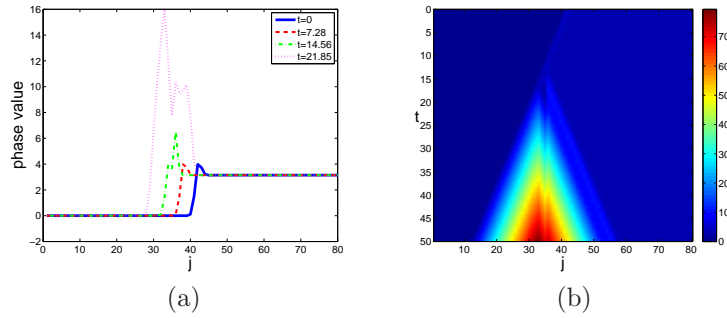
Figure 4.6: Unstable traveling wave at $(\mu, k) = (2\pi - 1.8, 0.75)$ with $c = -0.5493$: (a) Snapshots of the solution of Eq. (2.1) initialized at the traveling wave at times $t = 0$ (solid blue curve), 7.28 (dashed red), 14.56 (approximate onset of instability, dash-dotted green) and 21.85 (dotted magenta). (b) The contour plot of space-time evolution of the solution (with $\theta \in \mathbb{R}$) until time $t = 50$. The traveling wave becomes unstable after an initial propagation transient period and splits into two fronts propagating in opposite directions with the same speed as the initial wave.

other solution has front value 0 to π from left to right. In each case, based on given μ and corresponding solution, we set new parameters and transformed solution. We can derive the same traveling wave equation with transformed solution as solution at

new parameters. As a result, if we know the solution at (μ, k) in $[0, \pi]$. By symmetry property, we can know the solution at $(2\pi - \mu, k)$.

4.2.1 Periodicity and symmetry of standing wave solution in μ

In the ODE system (2.1), let the derivative term to be 0, we have a steady state solution. The solution to (4.7) is a standing wave solution.

$$0 = k[H(\theta_{j-1} - \theta_j) + H(\theta_{j+1} - \theta_j)] + f(\theta_j), \quad \text{for} \ \ j = 2, \ldots, N-1 \tag{4.7}$$

Here $H(\theta) = sin(\theta + \mu) - sin(\mu)$, $f(\theta) = -sin(2\theta)$.

Let $\bar{\theta} = \pi - \theta$, $\bar{\mu} = 2\pi - \mu$, θ is the standing wave solution at (μ, k). θ is π to 0 from left to right.

$$
\begin{aligned}
& k[H(\bar{\theta}_{j-1} - \bar{\theta}_j) + H(\bar{\theta}_{j+1} - \bar{\theta}_j)] + f(\bar{\theta}_j) \\
&= k[sin(\bar{\theta}_{j-1} - \bar{\theta}_j + \bar{\mu}) - sin(\bar{\mu}) + sin(\bar{\theta}_{j+1} - \bar{\theta}_j + \bar{\mu}) - sin(\bar{\mu})] - sin(2\bar{\theta}_j) \\
&= k[sin(\pi - \theta_{j-1} - \pi + \theta_j + 2\pi - \mu) - sin(2\pi - \mu) \\
& \quad + sin(\pi - \theta_{j+1} - \pi + \theta_j + 2\pi - \mu) - sin(2\pi - \mu)] - sin(2\pi - 2\theta_j) \\
&= k[sin(-\theta_{j-1} + \theta_j - \mu) - sin(-\mu) + sin(-\theta_{j+1} + \theta_j - \mu) - sin(-\mu)] - sin(-2\theta_j) \\
&= -k[sin(\theta_{j-1} - \theta_j + \mu) - sin(\mu) + sin(\theta_{j+1} - \theta_j + \mu) - sin(\mu)] + sin(2\theta_j) \\
&= -k[H(\theta_{j-1} - \theta_j) + H(\theta_{j+1} - \theta j)] - f(\theta_j) = 0
\end{aligned}
$$

$$\tag{4.8}$$

Thus $\bar{\theta}$ is a solution at point $(\bar{\mu}, k)$. Equivalently, θ and $\pi - \theta$ are solutions at points (μ, k) and $(2\pi - \mu, k)$ respectively. Because θ and $\pi - \theta$ share the same stability. So the stability curve of the standing wave is symmetric about π. In this way, we can extend the bifurcation curves. Because it is easy to prove the solution has period 2π in μ. So the bifurcation curves can be extended as shown in Fig. 4.7, region IV, V,

VI are $\mu \in [\frac{3}{2}\pi, 2\pi]$, $[2\pi, \frac{5}{2}\pi]$ and $[\frac{5}{2}\pi, 3\pi]$ respectively. Bifurcation curves in region I and V are the same.

Next we show that the standing wave stability curve is symmetric about π in another way. Suppose $\theta = (\theta)$ is the solution at (μ, k). Let $\bar{\theta}_j = \pi - \theta_{N+1-j}$, $j = 1\ldots, N$, $\bar{\mu} = 2\pi - \mu$. $i = N + 1 - j$, $j = 2, \ldots, N - 1$, then $i = 2, \ldots, N - 1$. $\bar{\theta}$ is 0 to π from left to right.

$$k[H(\bar{\theta}_{j-1} - \bar{\theta}_j) + H(\bar{\theta}_{j+1} - \bar{\theta}_j)] + f(\bar{\theta}_j)$$

$$= k[sin(\bar{\theta}_{j-1} - \bar{\theta}_j + \bar{\mu}) - sin(\bar{\mu}) + sin(\bar{\theta}_{j+1} - \bar{\theta}_j + \bar{\mu}) - sin(\bar{\mu})] - sin(2\bar{\theta}_j)$$

$$= k[sin(\pi - \theta_{N+1-j+1} - \pi + \theta_{N+1-j} + 2\pi - \mu) - sin(2\pi - \mu)$$

$$\quad + sin(\pi - \theta_{N+1-j-1} - \pi + \theta_{N+1-j} + 2\pi - \mu) - sin(2\pi - \mu)] - sin(2\pi - 2\theta_{N+1-j})$$

$$= k[sin(-\theta_{N+1-j+1} + \theta_{N+1-j} - \mu) - sin(-\mu) + sin(-\theta_{N+1-j-1} + \theta_{N+1-j} - \mu)$$

$$\quad - sin(-\mu)] - sin(-2\theta_{N+1-j})$$

$$= -k[sin(\theta_{N+2-j} - \theta_{N+1-j} + \mu) - sin(\mu) + sin(\theta_{N-j} - \theta_{N+1-j} + \mu) - sin(\mu)]$$

$$\quad + sin(2\theta_{N+1-j})$$

$$= -k[H(\theta_{N+2-j} - \theta_{N+1-j}) + H(\theta_{N-j} - \theta_{N+1-j})] - f(\theta_{N+1-j})$$

$$= -k[H(\theta_{i+1} - \theta_i) + H(\theta_{i-1} - \theta_i)] - f(\theta_i) = 0$$

$$(4.9)$$

From the deduction of Eq. (4.9), θ and $\bar{\theta}$ are standing wave solutions at points(μ, k) and $(2\pi - \mu, k)$. Also θ and $\bar{\theta}$ share the same stability. Thus the bifurcations curves are symmetric about $\mu = \pi$. In Fig. 4.7, bifurcation curves in region I and II are symmetric with the ones in region IV and III respectively. This we prove the symmetry and periodicity of bifurcation curves(pitchfork curve and saddle-node curve).

45
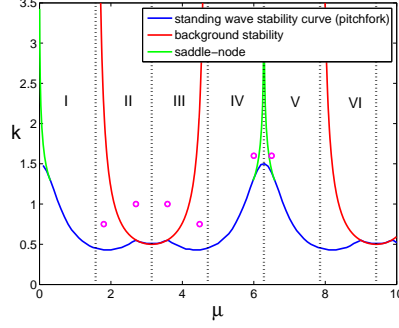
Figure 4.7: Extended pitchfork (blue) and saddle-node (green) bifurcation curves and the background instability curve (red). Magenta circles denote the parameter values where the stability of the traveling waves was probed via direct numerical computations.

4.2.2 Periodicity and symmetry of traveling wave solution in μ

We have analyzed the stability of the standing wave solution on an extended parameter domain. To extend these results to the whole upper half of the parameter plane, we will show that the stability of traveling wave solution is 2π-periodic in μ. Also the stability of traveling wave solution is symmetric about $\mu = \pi$.

To show this, we define new variables. Suppose ϕ is the solution to Eq (3.4) at point (μ, k). Define $\bar{\mu} = 2\pi - \mu$, variable $\bar{\phi}(z) = \pi - \phi(z)$. By this definition, μ and $\bar{\mu}$ are symmetric about π. By this definition, $\bar{\phi}'(z) = -\phi'(z)$. Replace $\phi(z)$ and μ in Eq. (3.4) with $\bar{\phi}(z)$ and $\bar{\mu}$. The we simplify equation of $\bar{\phi}(z)$ and $\bar{\mu}$, we can get the following Eq. (4.10) which is the same with Eq. (3.4).

$$-c(-\bar{\phi}'(z)) = k[sin(\pi - \bar{\phi}(z+1) - \pi + \bar{\phi}(z) + 2\pi - \bar{\mu}) - sin(2\pi - \bar{\mu})$$

$$+ sin(\pi - \bar{\phi}(z-1) - \pi + \bar{\phi}(z) + 2\pi - \bar{\mu}) - sin(2\pi - \bar{\mu})] - sin(2\pi - 2\bar{\phi}(z))$$

$$= k[-sin(\bar{\phi}(z+1) - \bar{\phi}(z) + \bar{\mu}) + sin(\bar{\mu}) - sin(\bar{\phi}(z-1) - \bar{\phi}(z) + \bar{\mu}) + sin(\bar{\mu})]$$

$$+ sin(2\bar{\phi}(z))$$

$$= -k[sin(\bar{\phi}(z+1) - \bar{\phi}(z) + \bar{\mu}) - sin(\bar{\mu}) + sin(\bar{\phi}(z-1) - \bar{\phi}(z) + \bar{\mu}) - sin(\bar{\mu})]$$

$$+ sin(2\bar{\phi}(z))$$

$$= -k[H(\bar{\phi}(z+1) - \bar{\phi}(z)) + H(\bar{\phi}(z-1) - \bar{\phi}(z))] + sin(2\bar{\phi}(z))$$

$$(4.10)$$

Take the negative of both sides of last equation, we have the following Eq. (4.11) which in fact coincides with Eq. (3.4).

$$-c(\bar{\phi}'(z)) = k[H(\bar{\phi}(z+1) - \bar{\phi}(z)) + H(\bar{\phi}(z-1) - \bar{\phi}(z))] + sin(2\bar{\phi}(z)) \qquad (4.11)$$

So $\bar{\phi}(z)$ is a traveling wave solution to the advance-delay differential equation Eq. (3.4). Also we know that if $\phi(z)$ is the solution at point (μ, k), then we can know that $\bar{\phi}(z)$ is a traveling wave solution to Eq. (3.4) at point $(2\pi - \mu, k)$. At point $(2\pi - \mu, k)$, the solution $\bar{\phi}(z)$ has value π on the left boundary and 0 on the right boundary. The wave leading by 0 side travels to right with speed c. The is the same speed (both value and direction) with the speed of solution $\phi(z)$ at (μ, k). Also $\bar{\phi}(z)$ and $\phi(z)$ share the same traveling wave stability. So the stability curve of the traveling wave solution is symmetric about $\mu = \pi$.

Next we show another solution to Eq. (3.4) at point $(\bar{\mu} = 2\pi - \mu, k)$. Similarly, suppose $\phi(z)$ is the solution to Eq. (3.4) at point (μ, k). We set the new parameter $\bar{\mu} = 2\pi - \mu$ and variable $\bar{c} = -c$, $\bar{z} = L - z$ and $\bar{\phi}(\bar{z}) = \pi - \phi(z)$. Suppose range of z is $[a, b]$, so $L = a + b$. Especially, if the range of z is symmetric about 0, then $L = a + (-a) = 0$ and $\bar{z} = -z$. By this setting, μ and $\bar{\mu}$ are symmetric about π and the value of $\phi(z)$ are kept to be 0 and π on left and right boundary respectively.

Naturally from the setting, we have

$$\phi'(z) = \frac{d\phi(z)}{dz} = \frac{d(\pi - \bar{\phi}(\bar{z}))}{d\bar{z}}\frac{d\bar{z}}{dz} = \bar{\phi}'(\bar{z})$$

$$\phi(z+1) = \pi - \bar{\phi}(\bar{z}-1) \tag{4.12}$$

$$\phi(z-1) = \pi - \bar{\phi}(\bar{z}+1)$$

Replace ϕ, μ, z and c with $\bar{\phi}$, $\bar{\mu}$, $\bar{z}$ and $\bar{c}$ in Eq. (3.4). Simplify the equation of $\bar{\phi}$, $\bar{\mu}$, $\bar{z}$ and $\bar{c}$, we can get the following Eq. (4.14).

$$- (-\bar{c})\bar{\phi}'(\bar{z}) = -c\phi'(z)$$

$$= k[H(\phi(z+1) - \phi(z)) + H(\phi(z-1) - \phi(z))] + f(\phi(z))$$

$$= k[sin(\pi - \bar{\phi}(\bar{z}-1) - \pi + \bar{\phi}(\bar{z}) + 2\pi - \bar{\mu}) - sin(2\pi - \bar{\mu})$$

$$\quad + sin(\pi - \bar{\phi}(\bar{z}+1) - \pi + \bar{\phi}(\bar{z}) + 2\pi - \bar{\mu}) - sin(2\pi - \bar{\mu})] - sin(2(\pi - \bar{\phi}(\bar{z})))$$

$$= k[sin(-\bar{\phi}(\bar{z}-1) + \bar{\phi}(\bar{z}) - \bar{\mu}) + sin(\bar{\mu}) + sin(-\bar{\phi}(\bar{z}+1) + \bar{\phi}(\bar{z}) - \bar{\mu}) + sin(\bar{\mu})]$$

$$\quad + sin(2\bar{\phi}(\bar{z}))$$

$$= -k[sin(\bar{\phi}(\bar{z}-1) - \bar{\phi}(\bar{z}) + \bar{\mu}) - sin(\bar{\mu}) + sin(\bar{\phi}(\bar{z}+1) - \bar{\phi}(\bar{z}) + \bar{\mu}) - sin(\bar{\mu})]$$

$$\quad + sin(2\bar{\phi}(\bar{z}))$$

$$= -k[H(\bar{\phi}(\bar{z}-1) - \bar{\phi}(\bar{z})) + H(\bar{\phi}(\bar{z}+1) - \bar{\phi}(\bar{z}))] - f(\bar{\phi}(z))$$

$$\tag{4.13}$$

Take the negative on both sides of Eq. (4.13), we can get

$$-\bar{c}\bar{\phi}'(\bar{z}) = k[H(\bar{\phi}(\bar{z}-1) - \bar{\phi}(\bar{z})) + H(\bar{\phi}(\bar{z}+1) - \bar{\phi}(\bar{z}))] + f(\bar{\phi}(z)) \tag{4.14}$$

Hence, $\bar{\phi}(\bar{z})$ is a solution to the traveling wave equation at $\bar{\mu} = 2\pi - \mu$ with velocity $\bar{c} = -c$. In other words, for any $k > 0$, given a traveling wave $\phi(z)$ with $\mu = \pi + b$ (for some b), there is a traveling wave at $\mu = \pi - b$ obtained through the above transformations. This traveling wave at $\mu = \pi - b$ has the same speed and

48

spectrum as the wave with $\mu = \pi + b$ but propagates in the direction opposite to that of the original traveling wave. This implies that the backward moving waves in regions III and IV of Fig. 4.7 are obtained directly from the waves in regions II and I, respectively, with the spectrum (and hence stability properties) preserved. The observed symmetry obviously exists not only at π but at $(2m - 1)\pi$ for any integer m. Note that in accordance with these results, the extended curve shown in Fig. 4.7 repeats periodically once μ reaches 2π and is symmetric about $\mu = \pi$ and $\mu = 3\pi$. Since the waves under study are 2π-periodic, this analysis can be extended to the entire upper half of the (μ, k) plane. In particular, it explains the symmetry observed above for the solution pairs at $(2.7, 1)$, $(2\pi - 2.7, 1)$ and at $(1.8, 0.75)$, $(2\pi - 1.8, 0.75)$.

Recall that the background is stable in the regions IV and V. To explore the traveling wave stability in these regions, we solve Eq. (3.4) at points $(6, 1.6)$ and $(4\pi - 6, 1.6)$ in regions IV and V, respectively. The fronts and their space-time evolution are shown in Fig. 4.8 for $(\mu, k) = (6, 1.6)$ and Fig. 4.9 for $(\mu, k) = (4\pi - 6, 1.6)$. At the point $(6, 1.6)$ in region IV, the wave is stable and travels to the left, in accordance with the negative velocity $c = -0.2919$ predicted by the traveling wave equation; see Fig. 4.8. At the point $(4\pi - 6, 1.6)$ in region V, the wave is also stable and travels to the right with the positive velocity $c = 0.2919$ as shown in Fig. 4.9.

Through the sample points we have checked in different regions. The results for regions $II - V$ are summarized in Table 4.1. In region II (III), all waves chosen initially move to the right (left) with the positive (negative) velocity predicted by the traveling wave Eq. (3.4) and eventually become unstable. In region IV (V), all waves move to the left (right) with the predicted negative (positive) velocity and remain stable.

In Table 4.2, the symmetry of the solution is shown. At each point (μ, k), there are two different solutions with same velocity and opposite direction. Also at symmetric points, (μ, k) and $(2\pi - \mu, k)$, given one solution $\phi(z)$, we can get a solution $\pi - \phi(z)$

(a)   (b)
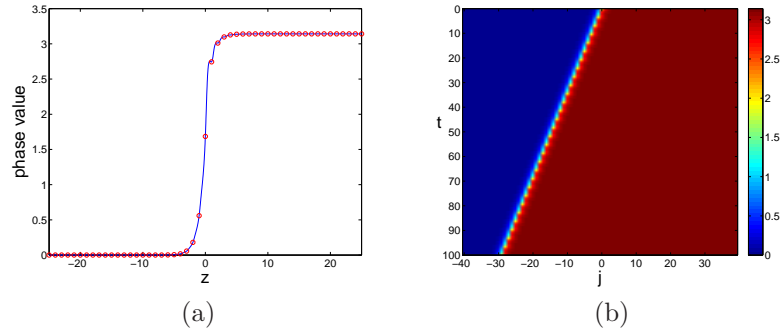
Figure 4.8: Stable traveling wave at $(\mu, k) = (6, 1.6)$ with $c = -0.2919$: (a) The traveling wave $\phi(z)$ (solid line) and the initial condition $\theta_j(0) = \phi(j)$ (circles) for the simulation of the ODE system (2.1). (b) The contour plot of the space-time evolution of the solution of ODE system (2.1) until time $t = 100$. In accordance with the predicted negative velocity, the traveling wave propagates to the left.

(a)   (b)
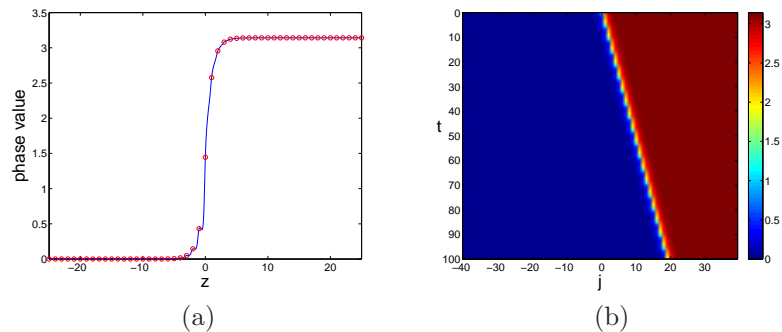
Figure 4.9: Stable traveling wave at $(\mu, k) = (4\pi - 6, 1.6)$ with $c = 0.2919$(a) The traveling wave $\phi(z)$ (solid line) and the initial condition $\theta_j(0) = \phi(j)$ (circles) for the simulation of the ODE system (2.1). (b) The contour plot of the space-time evolution of ODE system (2.1) until time $t = 100$. In accordance with the predicted positive velocity, the traveling wave now propagates to the right.

at the other point. The traveling wave solution property has period 2π in μ. So the solution at (μ, k) and $(2\pi + \mu, k)$ are the same. Similarly, at $(-\mu, k)$ and $(2\pi - \mu, k)$ share the same property.

In summary, we have obtained an analytical expression for the boundary of a region in parameter space where traveling waves suffer a background instability. Numerical simulations show that as parameters are varied above the zero-speed boundary

Table 4.1: Stability and velocities of traveling waves

point (μ, k)	region	stability	velocity
(2.7,1)	II	unstable (background)	0.2233
$(2\pi - 2.7,1)$	III	unstable (background)	-0.2233
(1.8,0.75)	II	unstable (frontal)	0.5493
$(2\pi - 1.8, 0.75)$	III	unstable (frontal)	-0.5493
(6,1.6)	IV	stable	-0.2919
$(4\pi - 6,1.6)$	V	stable	0.1894

Table 4.2: Symmetry in stability and velocities of traveling waves

point	solution	velocity
(μ, k) or $(2\pi + \mu, k)$	$\phi(z)$	c
(μ, k) or $(2\pi + \mu, k)$	$\phi(-z)$	-c
$(-\mu, k)$ or $(2\pi - \mu, k)$	$\pi - \phi(z)$	c
$(-\mu, k)$ or $(2\pi - \mu, k)$	$\pi - \phi(-z)$	-c

of the traveling wave region, traveling waves can be stable or can undergo either a background instability (within the region predicted analytically) or a frontal instability (between the stable region and the background instability region). Due to a symmetry in the model corresponding to the periodicity of H and f, all results repeat symmetrically about $\mu = n\pi$ and periodically in $\mu = 2n\pi$.

4.3   Details about the frontal and background instability

The results of our stability investigations are summarized in Table 4.1. We emphasize that curves in the (μ, k)-plane separating stable and unstable traveling waves sampled above *do not* coincide with the vertical lines $\mu = \pi/2$ and $\mu = 3\pi/2$ bounding regions II and III where unstable waves were found. In particular, our numerical results indicate that the curve separating stable traveling waves at small μ from the unstable ones in region II is located in region II slightly to the right of the vertical line $\mu = \pi/2$. By the symmetry described below we anticipate a similar stability boundary in region III slightly to the left of the line $\mu = 3\pi/2$.

$k = 0.5$	$\mu = 1.61$
$k = 0.6$	$\mu = 1.64$
$k = 0.7$	$\mu = 1.65$
$k = 0.75$	$\mu = 1.65$
$k = 0.8$	$\mu = 1.66$
$k = 0.9$	$\mu = 1.66$
$k = 1.0$	$\mu = 1.66$
$k = 1.1$	$\mu = 1.66$
$k = 1.2$	$\mu = 1.65$
$k = 1.3$	$\mu = 1.65$
$k = 1.3$	$\mu = 1.65$
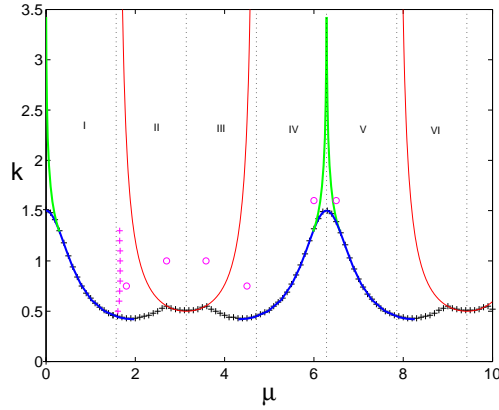
Figure 4.10: At (magenta) points near $\mu = \pi/2$, frontal instability initially disappears. For $\mu \leq \mu_f$, the frontal instability could not be observed.

Table 4.3: Points (μ_f, k_f) for $\mu \leq \mu_f$ where frontal instability disappears

As shown in Table 4.3, at $k = 0.75$, the frontal instability exists at least for $1.65 < \mu < q$, where q satisfies $0.75 = 0.5|\sec(q)|$; that is, until μ reaches the background instability region. No instability is observed for traveling waves at $\mu \leq 1.65$ and $k = 0.75$ propagated until time $t = 500$. The data in Table 4.3 is calculated with centered difference and parameter continuation from unstable region to stable region. The point is where frontal instability begin to disappear.

CHAPTER 5

TWO-DIMENSIONAL PHASE EQUATION DYNAMICS

In this chapter, we introduce the two dimensional ODE system based on the one-dimensional system in previous chapters. With some examples, we show dynamics of two-dimensional ODE system. We compare and visualize the dynamics of the two dimensional system with different initial value (θ) and parameter points (μ, k).

5.1 Two-dimensional discrete system set up

We now begin some explorations of the two-dimensional generalization of our oscillator problem. One oscillator $\theta_{i,j}$ is coupled with four oscillators in the neighborhood, $\theta_{i+1,j}$, $\theta_{i-1,j}$, $\theta_{i,j+1}$ and $\theta_{i,j-1}$ with coupling strength k. Naturally Eq. (2.1) can be extended to two dimensions with the following form. Here $H(\theta)$ and $f(\theta)$ are kept to be the same.

$$\dot{\theta}_{1,1} = k(H(\theta_{1,2} - \theta_{1,1}) + H(\theta_{2,1} - \theta_{1,1})) + f(\theta_{1,1})$$

$$\dot{\theta}_{i,1} = k(H(\theta_{i,2} - \theta_{i,1}) + H(\theta_{i+1,1} - \theta_{i,1}) + H(\theta_{i-1,1} - \theta_{i,1})) + f(\theta_{i,1}),$$

$$i = 2, \ldots, 2n - 1,$$

$$\dot{\theta}_{1,j} = k(H(\theta_{1,j+1} - \theta_{1,j}) + H(\theta_{1,j-1} - \theta_{1,j}) + H(\theta_{2,j} - \theta_{1,j})) + f(\theta_{1,j}),$$

$$j = 2, \ldots, 2n - 1,$$

$$\dot{\theta}_{i,j} = k(H(\theta_{i,j+1} - \theta_{i,j}) + H(\theta_{i,j-1} - \theta_{i,j}) + H(\theta_{i+1,j} - \theta_{i,j}) + H(\theta_{i-1,j} - \theta_{i,j}))$$

$$+ f(\theta_{i,j}), \quad i, j = 2, \ldots, 2n - 1,$$

$$\dot{\theta}_{i,2n} = k(H(\theta_{i,2n-1} - \theta_{i,2n}) + H(\theta_{i+1,2n} - \theta_{i,2n}) + H(\theta_{i-1,2n} - \theta_{i,2n})) + f(\theta_{i,2n}),$$

$$i = 2, \ldots, 2n - 1,$$

$$\dot{\theta}_{2n,j} = k(H(\theta_{2n,j+1} - \theta_{2n,j}) + H(\theta_{2n,j-1} - \theta_{2n,j}) + H(\theta_{2n-1,j} - \theta_{2n,j})) + f(\theta_{2n,j}),$$

$$j = 2, \ldots, 2n - 1,$$

$$\dot{\theta}_{2n,2n} = k(H(\theta_{2n,2n-1} - \theta_{2n,2n}) + H(\theta_{2n-1,2n} - \theta_{2n,2n})) + f(\theta_{2n,2n}).$$

$$(5.1)$$

We start the exploration by solving Eq. (3.4) on the interval $[-25, 25]$ at the parameter values $k = 1.3$ and $\mu = 0.5$ to obtain a one-dimensional traveling wave $\phi(z)$ with velocity $c = 0.4155$. We then solve Eq. (5.1) for $\theta_{i,j}(t)$ using the classical fourth order Runge-Kutta method with the initial data

$$\theta_{i,j}(0) = \begin{cases} 0, & i \leq 3 \\ \phi(i-3), & 4 \leq i \leq 54 \\ \pi, & i \geq 55, \end{cases}$$

and study the two-dimensional evolution of an initially planar front. The planar front propagates in the horizontal direction at the velocity of the one-dimensional wave, suggesting that the solution $\theta_{i,j}(t) = \phi(i - ct)$, which corresponds to a stable traveling
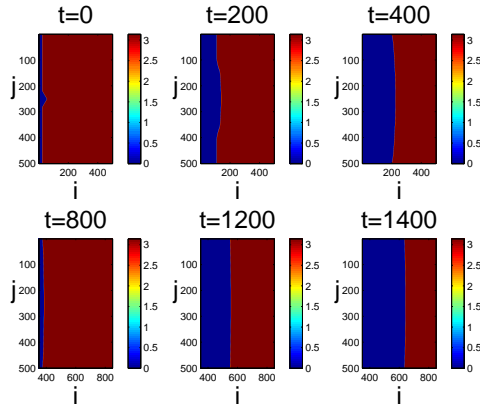
Figure 5.1: Snapshots of the evolution of a perturbed planar front introduced within a two-dimensional domain with $k = 1.3$, $\mu = 0.5$ at times $t = 0, 200, 400, 800, 1200$ and 1400. The evolution shows the healing of the front and the decay of the associated perturbation that restore the dynamically robust planar front traveling with velocity $c = 0.4155$.

wave in the one-dimensional problem, is also stable in the two-dimensional setting. To illustrate this stability, we distort a segment of the planar front in the initial condition, as shown in the first panel ($t = 0$) in Fig. 5.1. The resulting evolution is shown in the remaining panels of Fig. 5.1, where for better visualization, the range of the i-axis is shifted to the left in the last three panels. It can be seen that over time the system "heals" the perturbation and gradually restores its quasi-one-dimensional planar front character, while the solution eventually settles into traveling with the velocity predicted by the one-dimensional results.
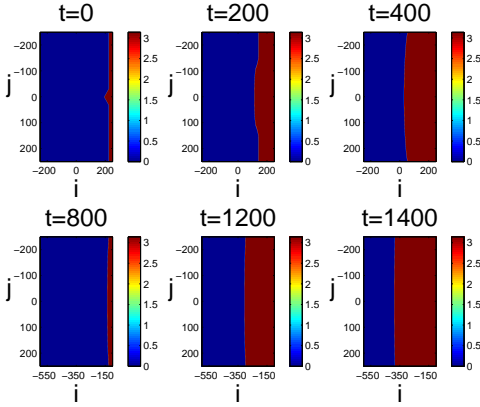
Figure 5.2: Snapshots of the evolution with $\mu = -0.5$, k=1.3. $\theta_{i,j}$ is replaced with $\pi - \theta_{N+1-i,j}$ for any j. This shows the perturbed front travels to the left with velocity approximately $c = 0.4155$.

In Fig. 5.2, we change μ to $-\mu$ and $\theta_{i,j} = \pi - \theta_{N+1-i,j}$, for $j \in [1, N]$. The wave changes the direction but with the same speed. This conclusion is similar with the one we get in one-dimension dynamic system as shown in Table 4.2.

Next we consider the evolution of a radial front. In panel (a) of Fig. 5.3, we show the evolution of an initially circular front for $k = 1.3$ and $\mu = 0.5$. The initial condition is set to $\theta_{i,j}(0) = \pi$ for (i, j) within the circle of radius 30 centered at $(40, 40)$, and $\theta_{i,j}(0) = 0$ outside of the concentric circle of radius 36. The initial value of $\theta_{i,j}$ for (i, j) between these circles is obtained by linear interpolation. The front shrinks and is eventually annihilated (i.e., disappears). The panel (b) of Fig. 5.3 displays horizontal slices of the solution at the initial and final time steps shown above. Notice that in this case, apparently, the initial radial profile of the front is gradually deformed to conform more suitably to the square symmetry of the underlying lattice grid. Hence it appears that linear (planar) fronts are fairly robust in this system, while radial ones are clearly not as robust and eventually disappear.

In Fig. 5.4 panel (a), the initial value is radical front. Within radius 10, the value is 0. Outside of circle with radius 15, the value is π. Between layer with radius 10 and

56
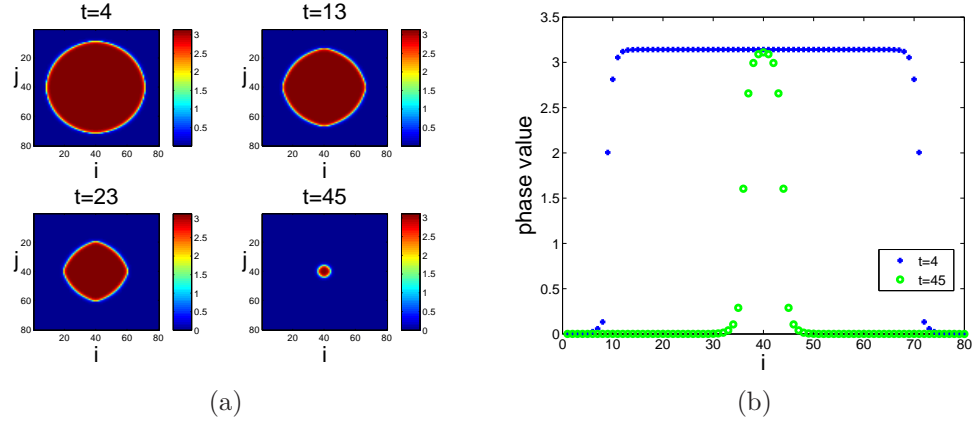
Figure 5.3: Snapshots of the evolution of a circular front with $k = 1.3$, $\mu = 0.5$ at times $t = 4$, 13, 23 and 45. The front shrinks (and is eventually annihilated) as time evolves. In the bottom panel, a horizontal section($j = 40$) of the front at $t = 4$ is denoted by plus signs and a horizontal section of the front at $t = 45$ (of smaller width) is denoted by circles.

15, the value is the linear combination of 0 and π. With $\mu = 0.5, k = 1.3$, as shown in the time evolution at $t = 0, 10, 20$ and 40, the front expands into rectangle shape which is limited by the rectangle boundary. In Fig. 5.4 panel (b), the initial value is radical front. Within radius 10, the value is π. Outside the circle of radius of 15, the value is 0. Between layer with radius 10 and 15, the value is the linear combination of π and 0. With $\mu = -0.5, k = 1.3$, as shown in the time evolution at $t = 0, 10, 20$ and 40, the front expands and evolve into rectangle shape due to the limitation of the rectangle boundary.
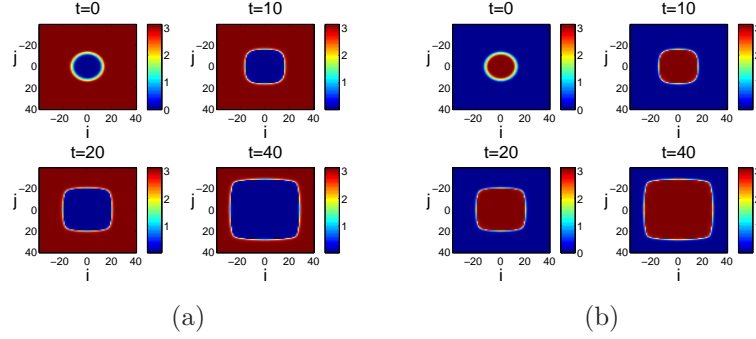
Figure 5.4: Panel (a) Snapshots of the evolution of a circular front with $\mu = 0.5$, $k = 1.3$. The initial value of the ODE system is the reverse of the previous one. It is radical front with 0 value within the circle and value π outside the circle. The front expands as time evolves and value of 0 region invades value π region(0 invades π). Panel (b) Snapshots of the evolution of a circular front with $\mu = -0.5, k = 1.3$ at t=0, 10, 20 and 40. The front expands as time evolves and value of π region invades value 0 region(π invades 0).

5.2 Dynamics of two-dimensional discrete system

As noted in [5], Carpenter [4] observed that experimentally induced phosphenes move according to the following rules in two dimensions:

1. Lines never cross through one another. Rather, they combine to form loops.

2. A line never breaks apart unless it meets another line.

To test whether our two-dimensional model captures these features, we now consider simulations with two symmetric fronts that initially bulge either outward (Fig. 5.5 and Fig. 5.7) or inward (Fig. 5.6 and Fig. 5.8). These initial conditions are shown in the first panel ($t = 0$) of each figure. The simulation results shown in Figs. 5.5-5.8, with $k = 1.3$, $\mu = 0.5$ in Fig. 5.5 and Fig. 5.6 and $k = 2$, $\mu = 0.15$ in Fig. 5.7 and Fig. 5.8, are consistent with Carpenter's observations listed above. We can see that the outwardly bulging fronts eventually touch near the edges of the domain and form one loop. Meanwhile, the inwardly bulging fronts eventually touch near their centers and the lines break into two parts. These features are very much in line with the expectations of [5] (compare with their Fig. 3). However, it should also be mentioned

that [5] posit a third and final feature, namely that:

3. Neighboring lines show a tendency to move in a similar manner.

Our simulations of the coupled oscillator model did *not* reveal such a tendency. Whether the model can be improved to reflect this feature is a question that remains to be considered in future studies.
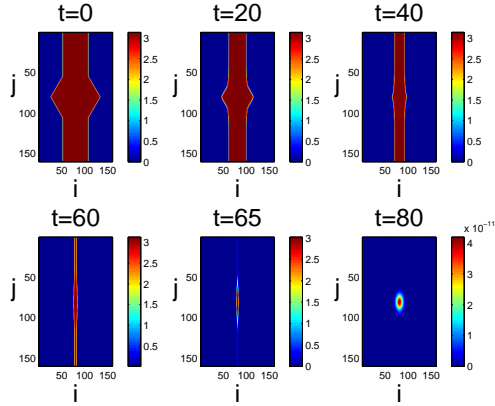
Figure 5.5: Snapshots of two outwardly perturbed fronts at times $t = 0$, 20, 40, 60, 65 and 80 when $k = 1.3$, $\mu = 0.5$. The fronts meet near the domain edges, form a loop, and shrink.
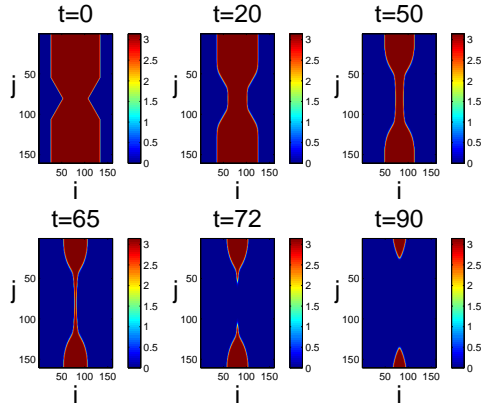
Figure 5.6: Snapshots of two inwardly perturbed fronts at times $t = 0$, 20, 50, 65, 72 and 90 when $k = 1.3$, $\mu = 0.5$. The fronts meet near their centers, separate, and evolve into two (upper and lower) parts.
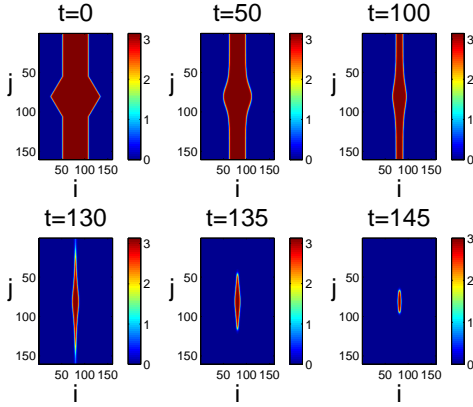
Figure 5.7: Snapshots of two outwardly perturbed fronts at times $t = 0, 50, 100, 130,$ 135 and 145 when $k = 2, \mu = 0.15$. As in Fig. 5.5, the fronts meet near the domain edges, form a loop, and shrink.
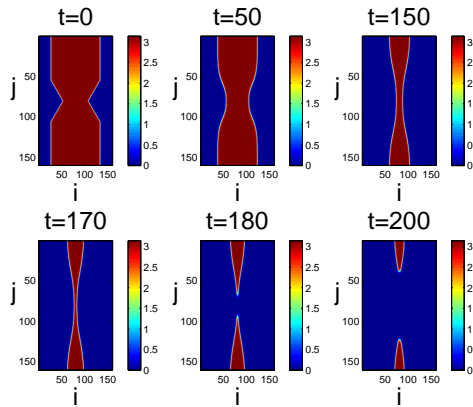
Figure 5.8: Snapshots of two inwardly perturbed fronts at times $t = 0, 50, 150, 170,$ 180 and 200 when $k = 2, \mu = 0.15$. As in Fig. 5.6, the fronts meet near their centers, separate, and evolve into two (upper and lower) parts.

Fig. 5.9 shows the evolution of rectangle front with $\mu = 0.5, k = 1.3$. panel (a), the initial value is set to be rectangle with vertex pointing to vertex of boundary rectangle. From the observation of front at $t = 0, 20, 40$ and 60, the rectangle front shrinks to a circle and finally disappears. In panel (b), the initial value is set to be rectangle with vertex pointing to edge. As shown in $t = 0, 20, 30$ and 35. the rectangle front shrinks and disappears finally.
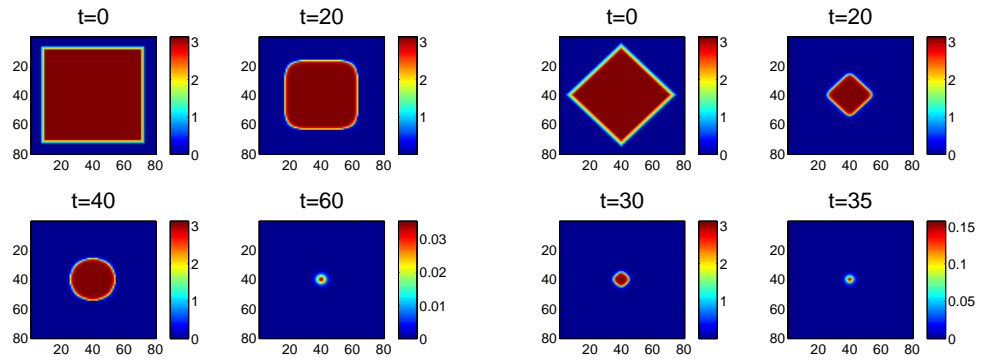
Figure 5.9: Panel (a) Snapshots of rectangle front at times $t = 0, 20, 40$ and 60 when $\mu = 0.5, k = 1.3$. The rectangle front shrinks (and is eventually annihilated) as time evolves. Panel (b) Snapshots of rectangle front at times $t = 0, 20, 30$ and 35 when $\mu = 0.5, k = 1.3$. The rectangle front shrinks (and is eventually annihilated) as time evolves

CHAPTER 6

SOME DETAILS ON NUMERICAL METHODS

In this chapter, we compare and analyze the stability of the traveling wave solution to the advance delay equation (3.4) with both forward and centered difference. Through analysis of eigenvalue spectrums of Jacobian matrix, we discuss the difference in stability of traveling wave solution with two schemes. Also the eigenvalue of background equilibrium state is compared with forward and centered difference result.

6.1 A hyperbolic PDE example

In this section, we solve the following hyperbolic PDE with both forward and centered difference. To analysis the stability, suppose U_j^n is the solution to Eq. (6.1). Here n is the indicator of time discretization and j is the indicator of space discretization. This is an example in [28] Chapter 4.

$$u_t - cu_x = 0 \tag{6.1}$$

With centered difference in space discretization, we have the scheme

$$\frac{U_j^{n+1} - U_j^n}{\Delta t} - c\frac{U_{j+1}^n - U_{j-1}^n}{2\Delta x} = 0 \tag{6.2}$$

Replace with the Fourier mode $U_j^n = \lambda^n e^{ik(j\Delta x)}$. Thus we have

$$\frac{\lambda^{n+1}e^{ikj\Delta x} - \lambda^n e^{ikj\Delta x}}{\Delta t} - c\frac{\lambda^n e^{ik(j+1)\Delta x} - \lambda^n e^{ik(j-1)\Delta x}}{2\Delta x} = 0 \tag{6.3}$$

Simplify it, we can get

$$\lambda - 1 = \frac{c\Delta t}{2\Delta x}(e^{ik\Delta x} - e^{-ik\Delta x}) \tag{6.4}$$

$$\lambda = 1 + \frac{c\Delta t}{\Delta x}isin(k\Delta x) \tag{6.5}$$

Thus we have

$$|\lambda|^2 = 1 + \sigma^2 sin^2(k\Delta x) \tag{6.6}$$

Here $\sigma = c\frac{\Delta t}{\Delta x}$. Because $|\lambda| > 1$ for any value of Δx and Δt, the scheme is unstable [28].

With forward difference in space discretization, we have

$$\frac{U_j^{n+1} - U_j^n}{\Delta t} - c\frac{U_{j+1}^n - U_j^n}{\Delta x} = 0 \tag{6.7}$$

Then we have

$$\frac{\lambda^{n+1}e^{ikj\Delta x} - \lambda^n e^{ikj\Delta x}}{\Delta t} - c\frac{\lambda^n e^{ik(j+1)\Delta x} - \lambda^n e^{ik(j)\Delta x}}{\Delta x} = 0 \tag{6.8}$$

Simplify the equation, we can get,

$$\lambda = 1 + \frac{c\Delta t}{\Delta x}(e^{ik\Delta x} - 1) \tag{6.9}$$

$$\lambda = 1 + \sigma(cos(k\Delta x) + isin(k\Delta x) - 1) \tag{6.10}$$

Thus we have

$$|\lambda|^2 = (1 + \sigma(cos(k\Delta x) - 1))^2 + \sigma^2 sin^2(k\Delta x) \tag{6.11}$$

$$|\lambda|^2 = (1 - \sigma)^2 + \sigma^2 + 2\sigma cos(k\Delta x)(1 - \sigma)$$

$$= 1 + 2\sigma(1 - \sigma)(cos(k\Delta x) - 1)$$

$$= 1 - 2\sigma(1 - \sigma)sin^2(k\Delta x/2) \tag{6.12}$$

For σ satisfying $0 < \sigma = \frac{c\Delta t}{\Delta x} < 1$, the scheme is stable [28].

From the analysis of this example [28], solving Eq. (6.1) with centered difference makes the scheme unstable. But with forward difference, it's stable under certain condition. Compare with our advance delay differential equation which can be written as $u_t - cu_x = f(u)$. There is an extra term $f(u)$. We tentatively propose that the centered difference is not as accurate as forward difference in stability prediction given certain condition satisfied.

6.2 Traveling wave solution stability analysis with forward and centered difference methods

This section examines the stability of the advance delay equation Eq. (3.4) solved with both forward and centered differences. In Fig. 6.1, we show the eigenvalues of Jacobian matrix (both forward and centered difference) for the traveling wave solution at $\mu = 0.5, k = 1.5$, and the background spectrum. Through comparison, we can observe that the centered difference method's error is in the positive real part of the eigenvalue. This instability is predicted by the analysis in section 6.1. The error in the forward difference does not generally affect the stability.

In Fig. 6.2, we show the stability curve obtained from the forward difference and centered difference. The difference implies that the stability analysis with centered difference is inaccurate. Even though the stability curve from the centered difference method is inaccurate, the traveling wave solutions are very accurate. By analysis above, we continue to compare the stability curves obtained with both finite differentiation schemes. In computation, if the maximum real part of eigenvalue is greater than 0.001, we assume the traveling wave solution is unstable. We can see that the stability curves in Fig. 6.2 are very different. The one with centered difference method is much higher than the forward one. Also the stability curve calculated with for-

ward difference is almost overlap with saddle-node curve. This provides a relatively accurate stability prediction.

6.3 Background stability analysis with forward and centered difference methods

To solve the traveling wave Eq. (3.4), we used a second order forward difference scheme and sometimes a second order centered difference scheme to approximate the term $\phi'(z)$. For a grid point j, these approximations are of the form $(-3\theta_j + 4\theta_{j+1} - \theta_{j+2})/(2\Delta x)$ and $(\theta_{j+1} - \theta_{j-1})/(2\Delta x)$, respectively, where Δx is the grid spacing. In some cases, the forward difference approximation used in solving Eq. (3.4) did not converge but the centered difference approximation did. Whichever approximation was used to solve Eq. (3.4) for the traveling wave $\phi(z)$, it was checked that the solution of the ODE system (2.1) with the initial condition $\theta_i(0) = \phi(i)$ produced results that were consistent with the obtained traveling wave solution.

In the following we analyze the stability of the background state in the discretized Eq. (3.4) with the forward and centered difference approximations described above. First, the forward difference approximation is analyzed. In Fig. 4.1, we see that the eigenvalues of the Jacobian for Eq. (3.4) approximate the eigenvalues of the continuum background as the number of points is increased, although the full structure of the forward difference spectral locus is more complex. The eigenvalues for the background can also be obtained in the context of the forward difference as follows. In this case, Eq. (4.2) obtained by linearizing Eq. (3.2) about the background equilibrium state $\Theta_0 = 0$ or $\Theta_0 = \pi$ is replaced by

$$V_\tau - c \left[\frac{-V(J+2,\tau) + 4V(J+1,\tau) - 3V(J,\tau)}{2\Delta x} \right] = \\ k\cos(\mu)[(V(J+q,\tau) - 2V(J,\tau) + V(J-q,\tau))] - 2V(J,\tau), \tag{6.13}$$
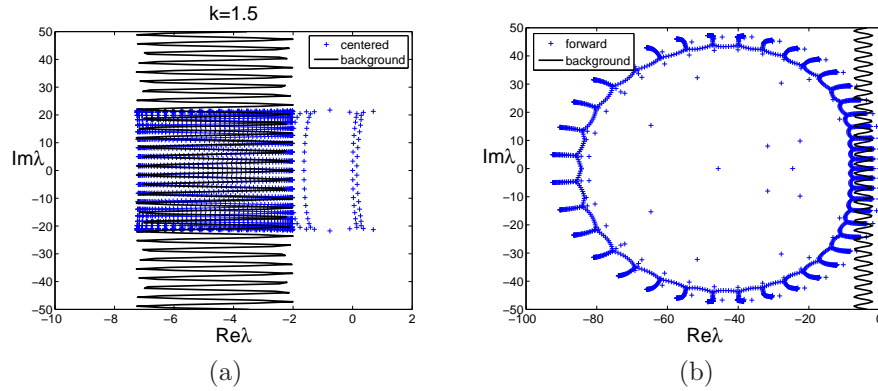
Figure 6.1: Part(a) The eigenvalue of the Jacobian for the traveling wave solution at $\mu = 0.5, k = 1.5$ with centered difference(blue plus). The continuous background spectrum curve given by Eq. (4.6)(black solid). Part(b) The eigenvalue of the Jacobian with forward difference (blue plus). The continuous background spectrum (black solid).
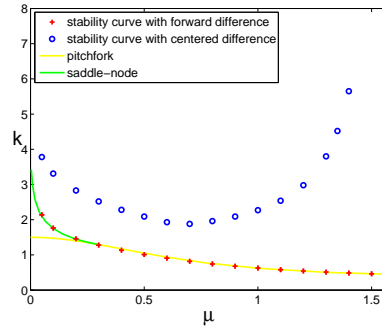
Figure 6.2: stability curves calculated with centered difference(blue circle) and forward difference(red plus). Through comparison, the stability curve with centered difference is much higher than bifurcation curves. The stability curve with forward difference is almost overlap with saddle-node curve.
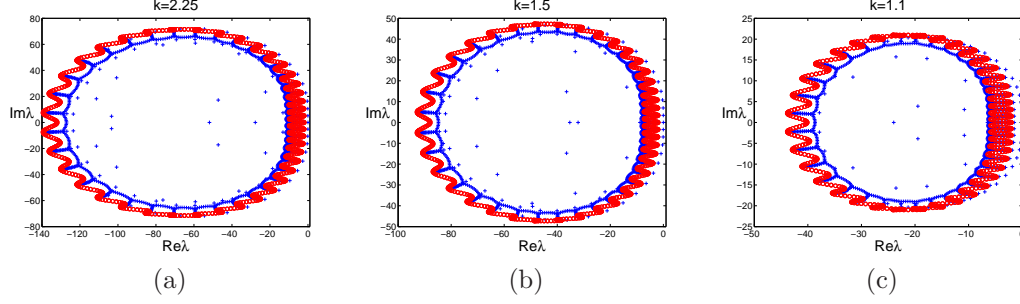
Figure 6.3: Plot of the eigenvalues of the Jacobian associated with the linearization of Eq. (3.2) about the traveling wave solution (blue pluses), solved on $[-25, 25]$ using 2001 nodes and a forward difference scheme, and the eigenvalues for the background equilibrium state (red circles) given by Eq. (6.14). Here $\mu = 0.5$ and $k = 2.25$, 1.5 and 1.1.

where $V(J, \tau)$ is the approximation of $v(z, \tau)$ at a grid point $z_J = J\Delta x$ for integer J and q is an integer such that $q\Delta x = 1$. Seeking solutions in the form $V_J(\tau) = e^{\lambda\tau} e^{iJp\Delta x}$, where p is the wave number, and solving for λ, we find that

$$\lambda = c \left[\frac{-\cos(2p\Delta x) + 4\cos(p\Delta x) - 3}{2\Delta x} \right] + 2k\cos\mu(\cos(p) - 1) - 2 \\ + ic \left[\frac{-\sin(2p\Delta x) + 4\sin(p\Delta x)}{2\Delta x} \right]. \tag{6.14}$$

The real and imaginary parts of these eigenvalues parametrized by p are shown by red circles in Fig. 6.3 at $k = 2.25$, 1.5 and 1.1 and $\mu = 0.5$. For comparison, the eigenvalues of the Jacobian associated with the traveling wave solution are shown by blue pluses (recall also Fig. 4.1, where these eigenvalues are shown for the case $k = 1.5$ and $\mu = 0.5$ for different numbers of nodes in the discretization.) To solve (3.4), 2001 nodes are used in $[-25, 25]$. The plots show that the two sets of eigenvalues are close to each other.

Expanding Eq. (6.14) in Taylor series at small Δx, we obtain

$$\lambda = -\frac{cp^4(\Delta x)^3}{4} + 2\{k\cos(\mu)(\cos(p) - 1) - 1\} + i(cp + c\frac{p^3}{3}(\Delta x)^2 + O((\Delta x)^4)),$$

67

which yields Eq. (4.4) in the limit $\Delta x \to 0$. The principal part of the error in the real and imaginary parts is $-c\frac{p^4}{4}(\Delta x)^3$ and $c\frac{p^3}{3}(\Delta x)^2$ respectively. As the wave number p increases, this error pushes the real part of λ to $-\infty$ and the imaginary part to $+\infty$ and $-\infty$, again in line with the observations of Fig. 4.1.

It is interesting to explore the spectral properties of the background of the traveling wave using a centered difference approximation instead of the forward difference approximation. Eq. (6.13) is then replaced by

$$V_\tau - c\frac{V(J+1,\tau) - V(J-1,\tau)}{2\Delta x} = k\cos(\mu)(V(J+q,\tau)-2V(J,\tau)+V(J-q,\tau))-2V(J,\tau)$$

and the eigenvalues λ are given by

$$\lambda = 2k\cos(\mu)(\cos(p) - 1) - 2 + i\frac{c\sin(p\Delta x)}{\Delta x}. \tag{6.15}$$

In this case there is no error in the real part of λ.

Generally, this centered difference approximation is numerically unstable for the advection equation given by (3.2); see [28]. Here, we find that the nonlinear term does stabilize it for large enough values of k, but the instability in the numerical method is observed for smaller values of k even though the solutions of the traveling wave equation are stable, according to the forward difference approximation. For example, in Fig. 6.4 the eigenvalues obtained using the centered difference approximation of Eq. (3.4) are presented for $k = 2.25$, 1.5 and 1.1 with $\mu = 0.5$. The real parts of the eigenvalues mostly lie between -9.90 and -2 for $k = 2.25$, between -7.27 and -2 for $k = 1.5$ and between -5.86 and -2 for $k = 1.1$, which agree almost exactly with the continuum background theory based on Eq. (4.4). According to Fig. 6.4, however, with fixed $\mu = 0.5$, the centered difference approximation predicts that traveling waves become unstable somewhere between $k = 2.25$ and $k = 1.5$, as some eigenvalues emerge with positive real part due to the instabilities associated with the
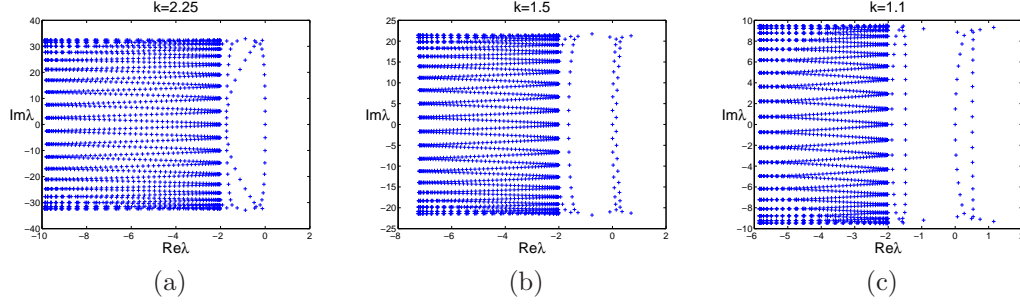
Figure 6.4: Plot of the eigenvalues of the Jacobian associated with the linearization of Eq. (3.2) about the traveling wave solution (blue pluses), solved on $[-25, 25]$ using 2001 nodes and centered difference approximation. Here $\mu = 0.5$ and $k = 2.25$, 1.5 and 1.1.

centered difference approximation. In the results presented in the manuscript, care has been taken to avoid such spurious instabilities induced by the numerical scheme. In Fig. 6.5, we shows the eigenvalues of the Jacobian for the traveling wave solution at $\mu = 0.5$, $k = 2.25, 1.5$ and 1.1. The red curve is the enlargement of eigenvalues for the background equilibrium state given by Eq. (6.15). The black curve is the continuous background spectrum curve given by Eq. (4.6), near the imaginary axis. We can observe that the eigenvalues are converging to the background spectrum as the continuum limit is approached.
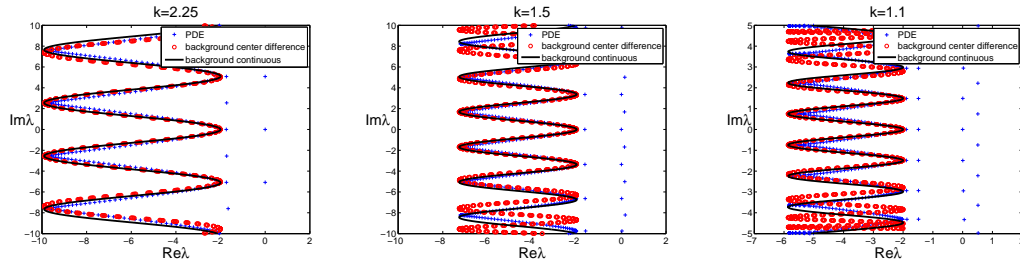
Figure 6.5: Enlarged version of eigenvalue of the Jacobian associated with the linearization about the traveling wave solution(blue pluses), background equilibrium state with centered difference(red circles) and continuous background for $\mu = 0.5$ and $k = 2.25$, 1.5 and 1.1 near imaginary axis.

CHAPTER 7

TURING INSTABILITY IN A HCV MODEL

Based on the HCV model in [32], Dahari et al. develop the HCV model by modifying proliferation and death terms in [33] and [34]. A Hepatitis C virus (HCV) model as shown in Eq. (7.1) is introduced to simulate the dynamics of infected, uninfected and virus cells [29]. We derive dimensionless 3-equation system and 2-equation system. Also we analyze and compare the stationary state of these two systems. A diffusion term and a spatial variable are introduced to investigate the Turing instability of the model. Routh-Hurwitz conditions are applied to test stability of the system. For most parameters, no Turing instability exists. We modify the model and observe Turing instability in the new system.

7.1   3-equation model

7.1.1   3-equation model set up

The model proposed by Reluga et al. in [29] is

$$\frac{dT}{d\hat{t}} = \hat{s} + r_T T(1 - \frac{T + I}{T_{max}}) - d_T T - (1 - \eta)\beta VT + \hat{q}I \tag{7.1a}$$

$$\frac{dI}{d\hat{t}} = r_I I(1 - \frac{T + I}{T_{max}}) + (1 - \eta)\beta VT - d_I I - \hat{q}I \tag{7.1b}$$

$$\frac{dV}{d\hat{t}} = (1 - \epsilon)pI - cV \tag{7.1c}$$

There are three variables T, I and V. T is uninfected hepatocytes, I is infected cells and V is the virus. The parameters in Eq. (7.1) include β (infected rate of T per free virus per hepatocyte), p (production rate of free virus by I), d_I (death rate of I), d_T

(death rate of T), c (free virus clearance rate by immune), r_T, r_I (proliferation rate of T and I), T_{max} (maximum of total number of hepatocytes), $\hat{s}$ (increase rate of T from other source than proliferation), $\hat{q}$ (cure rate of I), η (reduce rate of infection by treatment) and ϵ (reduce rate of viral production by treatment) [29]. Define dimensionless time $t = (r_T - d_T)\hat{t}$, dimensionless state variables:

$$x = \frac{T}{T_{max}}, \qquad y = \frac{I}{T_{max}}, \qquad z = \frac{V}{T_{max}} \tag{7.2}$$

and dimensionless parameters:

$$s = \frac{\hat{s}}{T_{max}(r_T - d_T)}, \; b = \frac{(1-\eta)\beta T_{max}}{r_T - d_T}, \; q = \frac{\hat{q}}{r_T - d_T},$$

$$d_1 = \frac{d_T}{r_T - d_T}, \; d_2 = \frac{d_I}{r_T - d_T}, \; r_1 = \frac{r_T}{r_T - d_T}, \; r_2 = \frac{r_I}{r_T - d_T},$$

$$\epsilon_0 = \frac{(1-\epsilon)p}{r_T - d_T}, \; c_0 = \frac{c}{r_T - d_T}.$$

Thus we get the non-dimensional 3-equation system:

$$\dot{x} = r_1 x(1 - x - y) - d_1 x - bxz + qy + s,$$

$$\dot{y} = r_2 y(1 - x - y) + bxz - d_2 y - qy, \tag{7.3}$$

$$\dot{z} = \epsilon_0 y - c_0 z$$

Initially we consider the simple case $s = q = 0$. Drop s and q terms, the 3-equation system can be written as:

$$\dot{x} = r_1 x(1 - x - y) - d_1 x - bxz$$

$$\dot{y} = r_2 y(1 - x - y) + bxz - d_2 y \tag{7.4}$$

$$\dot{z} = \epsilon_0 y - c_0 z$$

71

Solving the stationary solution of the equations, we get four equilibria $(0, 0, 0)$,
$(1 - \frac{d_1}{r_1}, 0, 0)$, $(0, 1 - \frac{d_2}{r_2}, \frac{\epsilon_0}{c_0}(1 - \frac{d_2}{r_2}))$ and $(-\hat{y} - \frac{b\epsilon_0}{c_0 r_1}\hat{y} + \frac{1}{r_1}, \hat{y}, \frac{\epsilon_0}{c_0}\hat{y})$.
Here $\hat{y} = \frac{c_0(c_0 r_1 d_2 + c_0 r_2 - b\epsilon_0 - c_0 r_1 r_2)}{b\epsilon_0(c_0 r_2 - c_0 r_1 - b\epsilon_0)}$.

Table 7.1: Estimated parameter as shown in [29]

Symbol	Left	Middle	Right
β	1.4×10^{-6}	9.0×10^{-8}	2.8×10^{-8}
T_{max}	5×10^6	5×10^6	1.2×10^7
p	28.7	10.9	13.2
$\hat{s}$	1	1	1
$\hat{q}$	0	0	0
c	6.0	5.8	5.4
d_T	1.2×10^{-2}	1.2×10^{-2}	1.2×10^{-2}
d_I	0.36	0.48	0.13
r_T	3.0	0.70	1.1
r_I	0.97	0.112	0.26

Based on the parameter values as shown in Table 7.1 [29, 40, 45, 44, 46, 43, 41, 42], we can calculate the stationary solution of this system. For each fixed point, we can check the eigenvalue of the following Jacobian matrix A. If all the eigenvalue has a negative real part, the fixed point is stable. Otherwise it is unstable.

$$A = \begin{bmatrix} r_1(1 - 2x - y) - d_1 - bz & -r_1 x & -bx \\ -r_2 y + bz & r_2(1 - x - 2y) - d_2 & bx \\ 0 & \epsilon_0 & -c_0 \end{bmatrix}$$

The equilibria of the 3-equation system for left data, middle data and right data is given in Table 7.2. For the middle and the right data, the last fixed point is negative which is unphysical. For the middle and right data, the stable fixed points only exist when there is no one infected ($y = 0$). The left data's fixed point allows a more interesting fixed point possessing infected and uninfected. It could be interesting to see how these fixed points change as the parameters vary.

72

Table 7.2: Fixed points for left, middle and right data

Left data fixed points	Stability	Middle data fixed points	Stability	Right data fixed points	Stability
(0,0,0)	unstable	(0,0,0)	unstable	(0,0,0)	unstable
(0.9960,0,0)	unstable	(0.9829,0,0)	stable	(0.9891,0,0)	stable
(0,0.6289,0.0602)	unstable	(0,-3.2857,-0.6175)	unstable	(0,0.5000,0.0049)	unstable
(0.3650,0.5159,0.0494)	stable	(6.4309,-4.8608,-0.9135)	unstable	(50.3354,-49.1994,-0.4811)	unstable

Next we show the simulation results of 3-equation system dynamics. Figs. 7.1, 7.2 and 7.3 show some computed trajectories for the 3-equation system when perturbation, of order 10^{-6}, are added to the fixed points for left data. All the initial points near the stable fixed point converge to stable fixed point and all unstable fixed points with small perturbation converge to the stable fixed point. In what follows, $P_0 = (x_0, y_0, z_0) = (0, 0, 0)$, $P_1 = (x_1, y_1, z_1) = (0.996, 0, 0)$, $P_2 = (x_2, y_2, z_2) = (0, 0.6289, 0.0602)$ and $P_3 = (x_3, y_3, z_3) = (0.3650, 0.5159, 0.0494)$. Note how the point near $P_0 = (0, 0, 0)$ moves quickly to the point $P_1 = (0.996, 0, 0)$ and stays near it for quite some time before moving on to the stable fixe point in Fig. 7.3.
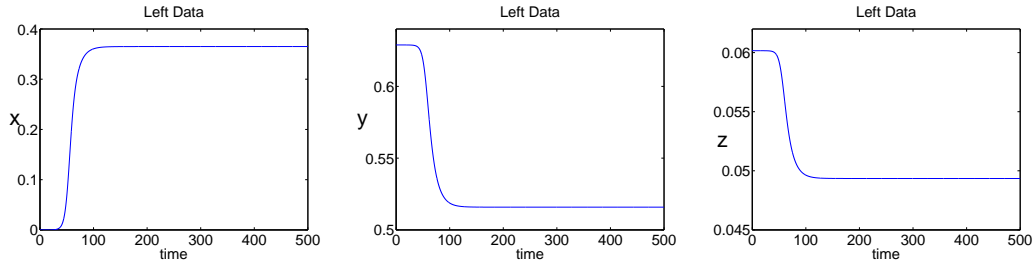
Figure 7.1: For left data: given a perturbation on unstable fixed point (0,0.6289,0.0602), it converges to stable fixed point (0.3650,0.5159,0.0494).

We show these three trajectories in a 3-d plot in Fig. 7.4. One notices again that the unstable point near P_0 moves quickly to the unstable point P_1 and stays there a while before moving to the stable fixed point P_3. We start at the initial point $(1000, 100, 10)$ for the left data, which is far away from the fixed points. The computed trajectories results are shown in Fig. 7.5(a). Fig. 7.5(b) is the trajectory
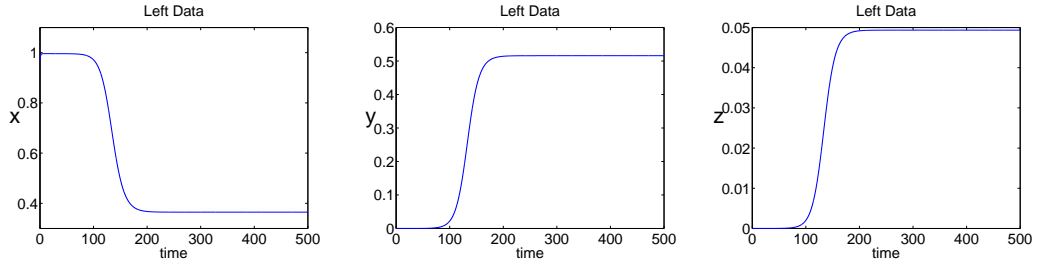
Figure 7.2: For left data: given an perturbation on unstable fixed point (0.9660,0,0), it converges to stable fixed point (0.3650,0.5159,0.0494).
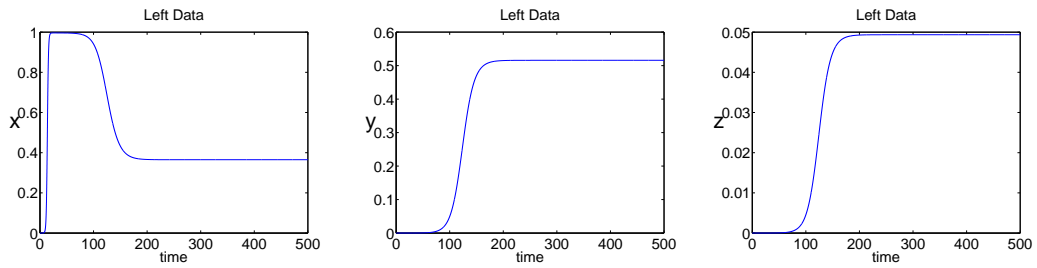
Figure 7.3: For left data: given an perturbation on unstable fixed point (0,0,0), it converges to stable fixed point (0.3650,0.5159,0.0494).

shown at a much later time. One can see clearly that the point goes to the unstable fixed point P_1 then to the stable fixed point P_3.
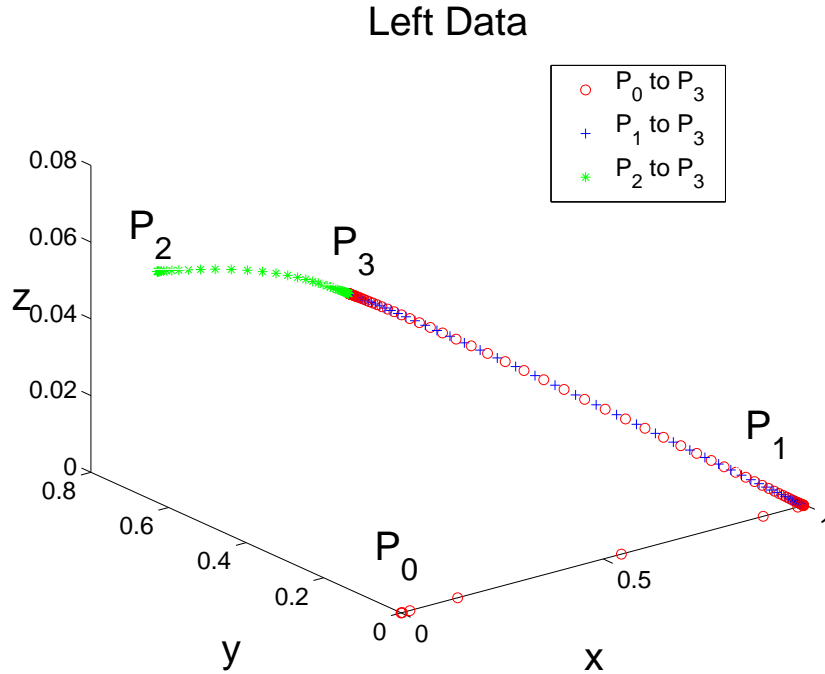
Figure 7.4: For left data: Given a perturbation on unstable fixed points $P_0 = (x_0, y_0, z_0) = (0, 0, 0)$(red), $P_1 = (x_1, y_1, z_1) = (0.9960, 0, 0)$(blue) and $P_2 = (x_2, y_2, z_2) = (0, 0.6289, 0.0602)$(green), they all converge to stable point $P_3 = (x_3, y_3, z_3) = (0.3650, 0.5159, 0.0494)$
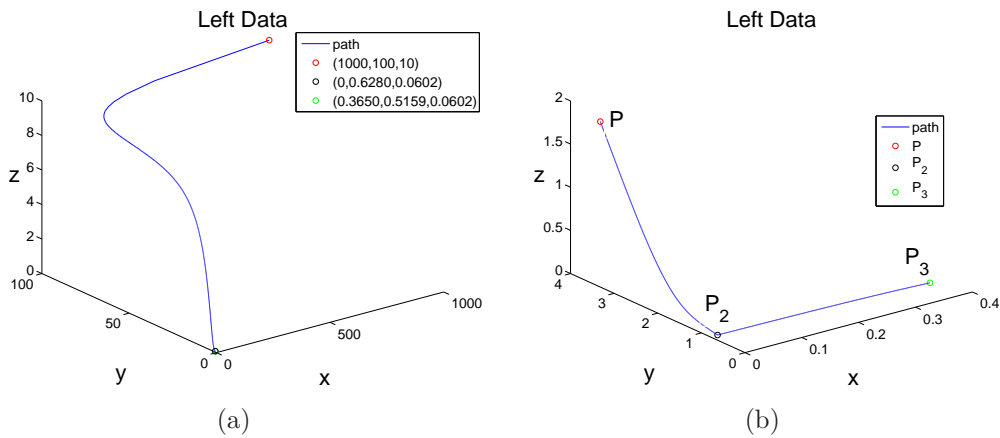
Figure 7.5: Panel (a): For left data, start from a point (1000,100,10) far away from fixed points, it converges to stable fixed point (0.3650,0.5159,0.0494). Panel (b): Zoom in the path close to the stable fixed point shown in Panel (a). $P(0, 3.3167, 1.9173)$ is a point on the trajectory. Before the point converges to P_3, it goes cross to unstable fixed point P_2 and then to the stable fixed point P_3.

7.1.2 Turing instability analysis of 3-equation model

We would like to investigate if there is any Turing (diffusion driven) instability for the system. The 3-equation model is given as follows.

$$\dot{x} = r_1 x(1 - x - y) - d_1 x - bxz = f(x, y, z)$$
$$\dot{y} = r_2 y(1 - x - y) + bxz - d_2 y = g(x, y, z) \tag{7.5}$$
$$\dot{z} = \epsilon_0 y - c_0 z = h(x, y, z)$$

Based on the Turing instability analysis in [31], suppose (x_0, y_0, z_0) is a steady state, then $f(x_0, y_0, z_0) = 0$, $g(x_0, y_0, z_0) = 0$ and $h(x_0, y_0, z_0) = 0$. Linearize about (x_0, y_0, z_0) and set

$$w = \begin{pmatrix} x - x_0 \\ y - y_0 \\ z - z_0 \end{pmatrix} \tag{7.6}$$

for $|w|$ small, we have

$$w_t = Aw \tag{7.7}$$

and

$$A = \begin{pmatrix} f_x & f_y & f_z \\ g_x & g_y & g_z \\ h_x & h_y & h_z \end{pmatrix} \tag{7.8}$$

We now look for solutions in the form $w \propto e^{\lambda t}$ and substitute it into Eq. (7.7), we have $Aw = \lambda w$ [31]. For a nontrivial w, the eigenvalue λ is the solution of $|A - \lambda I| = 0$. Thus we have stable solution if $Re\lambda < 0$. Adding diffusion terms, the reaction-diffusion system of equations becomes:

$$\dot{x} = f(x, y, z) + D_1 \Delta x$$

$$\dot{y} = g(x, y, z) + D_2 \Delta y \qquad (7.9)$$

$$\dot{z} = h(x, y, z) + D_3 \Delta z$$

D_1, D_2 and D_3 are positive diffusion coefficients.

Suppose (x_0, y_0, z_0) is a stable equilibrium of 3-equation system.

Linearizing about the steady state $w = 0$, we have

$$w_t = Aw + D\nabla^2 w \qquad D = \begin{pmatrix} D_1 & 0 & 0 \\ 0 & D_2 & 0 \\ 0 & 0 & D_3 \end{pmatrix} \qquad (7.10)$$

As discussed in [31], the problem is linear and we look for solutions $w(r, t)$ in the form

$$w(r, t) = \sum_k c_k e^{\lambda t} W_k(r) \qquad (7.11)$$

Here $W_k(r)$ is the eigenfunction corresponding to the wavenumber k satisfying $\nabla^2 W + k^2 W = 0$.

Plugging Eq. (7.11) into (7.10), for each k, we have

$$\lambda W_k = A W_k + D\nabla^2 W_k = A W_k - D k^2 W_k \qquad (7.12)$$

For nontrivial solutions for W_k, λ are determined by the roots of the characteristic polynomial $|\lambda - A + Dk^2| = 0$ which can be written as

$$p(\lambda) = \lambda^3 - Tr(\hat{A}(k^2))\lambda^2 + \lambda H(k^2) - det(\hat{A}(k^2)) = 0 \qquad (7.13)$$

where

$$\hat{A}\left(k^2\right) = \begin{bmatrix} -D_1 k^2 + f_x & f_y & f_z \\ g_x & -D_2 k^2 + g_y & g_z \\ h_x & h_y & -D_3 k^2 + h_z \end{bmatrix}.$$

$$\text{Tr}\left(\hat{A}(k^2)\right) = -k^2(D_1 + D_2 + D_3) + \text{Tr}(A),$$

$$H\left(k^2\right) = (D_1 D_2 + D_1 D_3 + D_2 D_3)k^4 - [g_y(D_1 + D_3) + f_x(D_2 + D_3)$$

$$+ h_z(D_1 + D_2)]k^2 + f_x g_y + f_x h_z + g_y h_z - g_z h_y - g_x f_y - f_z h_x,$$

$$\det\left(\hat{A}(k^2)\right) = -D_1 D_2 D_3 k^6 + (D_1 D_2 h_z + D_1 D_3 g_y + D_2 D_3 f_x)k^4$$

$$- (D_1 g_y h_z + D_2 f_x h_z + D_3 f_x g_y - D_1 g_z h_y - D_3 g_x f_y)k^2 + \det(A).$$

To examine the Turing instability of 3-equation system, we use the Routh-Hurwitz conditions. (The details of Routh-Hurwitz will be introduced in the last section of the Chapter.) Routh-Hurwitz conditions are necessary and sufficient conditions on coefficient a_i such that the zeros of $p(\lambda)$ have $Re(\lambda) < 0$, guaranteeing stability. For third degree characteristic polynomial $p(\lambda) = \lambda^3 + a_1\lambda^2 + a_2\lambda + a_3$, the Routh-Hurwitz criteria are $a_1 > 0$, $a_3 > 0$ and $a_1 a_2 > a_3$. Here $a_1 = -Tr(\hat{A}(k^2))$, $a_2 = H(k^2)$ and $a_3 = -det(\hat{A}(k^2))$.

To obtain the instability, we need to violate at least one of three above conditions. In other words, we need to satisfy at least one of the following conditions.

Condition 1: $Tr(\hat{A}(k^2)) > 0$

Condition 2: $det(\hat{A}(k^2)) > 0$

Condition 3: $Tr(\hat{A}(k^2))H(k^2) - det(\hat{A}(k^2)) > 0$

Next we show some simulation results for values of these conditions. Fig. 7.6-Fig. 7.9 are plots of $Tr(\hat{A}(k^2))$, $det(\hat{A}(k^2))$ and $Tr(\hat{A}(k^2))H(k^2) - det(\hat{A}(k^2))$ for

different diffusion coefficients D_1, D_2, D_3 and k. All the conditions values are negative. In over exhaustive computation, none of the three conditions were satisfied and the Routh-Hurwitz conditions were not violated. Turing instability was not observed here.

In Fig. 7.6 Let $D_1 = D_2 = 0$, $D_3 = 1$ and let k range over $[1, 100]$. In this case, we plot the condition values vs k for left, middle and right data. From the plot, we can see that three conditions value are negative.
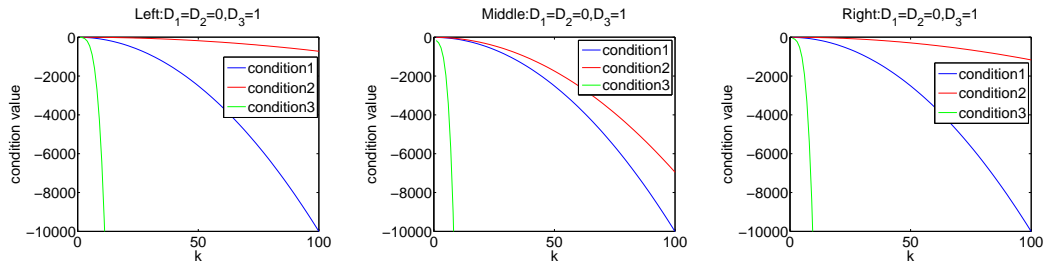
Figure 7.6: Keep $D_1 = D_2 = 0$, $D_3 = 1$. Plot of three conditions value vs k. From the plot, all the conditions values are negative.

In Fig. 7.7, let $D_1 = D_2 = 0$, $k = 1$. D_3 ranges over $[0.001, 1000]$. Plot the condition value vs D_3 for left, middle and right data. In this case, condition values are negative.
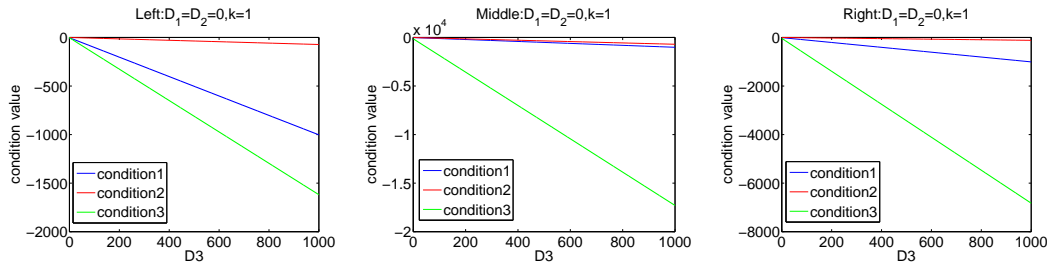
Figure 7.7: Keep $D_1 = D_2 = 0$, $k = 1$. Plot of condition value vs D_3. From the plot, three conditions value are all negative.

In Fig. 7.8, for right data, change value of ϵ from 0.996 to 0.2, 0.6 and 0.8. Other parameter values are kept the same: $D_1 = D_2 = 0$, $k = 1$. Plot the condition value vs D_3. From the results, all condition values are negative.
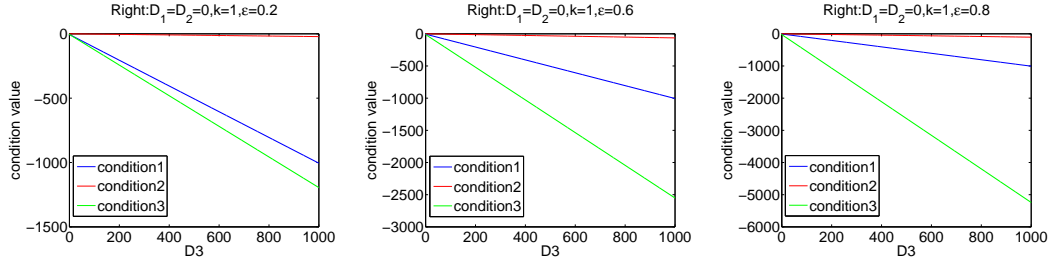
Figure 7.8: Keep $D_1 = D_2 = 0$, $k = 1$. Change the value of ϵ. Plot of condition values vs D_3. From the plot, three conditions value are all negative.

In Fig. 7.9, change value of D_1 and D_2 to 0.1. Other parameter values are kept the same: $k = 1$. Plot the condition values vs D_3 for left, middle and right data. From the results, all condition value are negative.
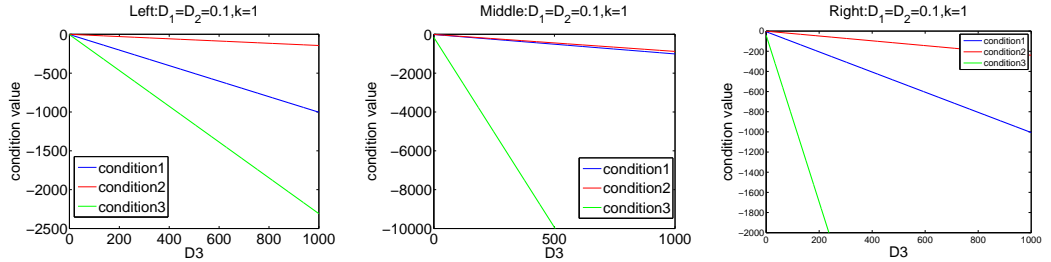
Figure 7.9: $D_1 = D_2 = 0.1$. Plot the condition value vs D_3 for left, middle and right data. From the plot, three conditions value are all negative.

From the tests above, if $D_1 = D_2 = 0$, the condition function, with given left, middle and right data, could not provide a positive condition value. In Fig. 7.8, value of ϵ is varied. From the plot, condition 2 values are closer to 0, but they are never positive. In Fig. 7.9, D_1 and D_2 value are changed to 0.1, keep other parameters to be the same, the condition values are still negative. No Turing instability is observed here.

7.1.3 Discussion about convergence to fixed points

For the left data, the nonzero fixed points and eigenvalues are listed in the following table. For the convergence of solution, there are two cases: convergence to stable fixed point $(0.3650, 0.5159, 0.0494)$ and stay at unstable fixed point $(0, 0.6289, 0.0602)$. For 3-equation model, the eigenvalues of Jacobian matrix at stable fixed point are negative. For the case the solution converges to stable fixed point, the distance between the solution and stable fixed point will converge to 0. For the case that solution stays at unstable fixed point, the eigenvalues for unstable fixed point $(0, 0.6289, 0.0602)$ are -2.0080, -0.2041, 0.2277. If the solution gets close to unstable fixed point, it should be attracted by the plane generated by eigenvectors corresponding two negative eigenvalues. The distance of solution to this plane and unstable fixed point should both decrease to almost 0.

Table 7.3: Fixed points and Eigenvalues for Left data

3-equation nonzero fixed point	stability	Eigenvalues
(0.9960,0,0)	unstable	(-1; 0.0941; 0.0602)
(0,0.6289,0.0602)	unstable	(-2.0080; -0.2041; 0.2277)
(0.3650,0.5159,0.0494)	stable	(-0.0817; -0.4471;-2.0949)

For most initial points near the fixed point, they will converge to stable fixed points. For some initial points lying far from fixed points, they may stay at unstable fixed points. For many points converging to stable fixed points, it will go through unstable fixed point(distance can be 10^{-10}) and then to stable fixed point. In Fig. 7.10 panel (a), with initial point $(0.3650+1, 0.5159+1, 0.0494+1)$, the trajectory initially goes towards the unstable fixed point but turns quickly to the stable fixed point. In Fig. 7.10 panel (b), with initial point $(0.3650 + 100, 0.5159 + 100, 0.0494 + 100)$, the trajectory stays very near the unstable fixed point until about $t = 600$ then goes towards the stable fixed point. In panel (c) and (d), with initial point $(0.3650+$

$1000, 0.5159+1000, 0.0494+1000$), we show a trajectory until $t = 100$ (c) and $t = 1000$ (d). It stays near the unstable fixed point at least until $t = 1000$.
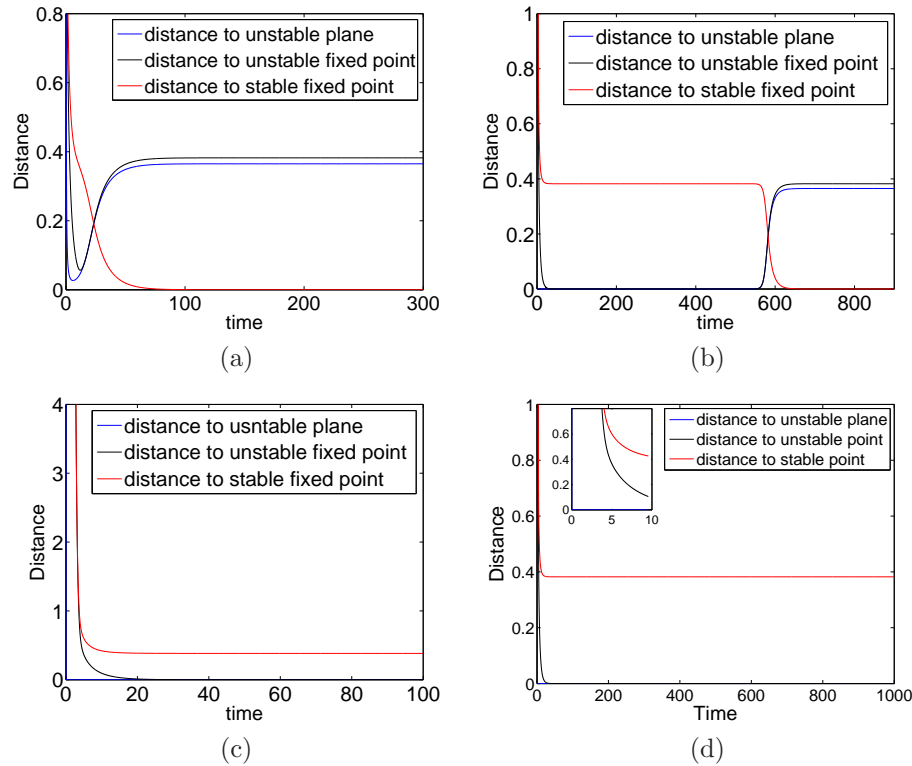
Figure 7.10: Part (a), initial value: $(0.3650 + 1, 0.5159 + 1, 0.0494 + 1)$, add stable fixed point by 1. The solution converges to stable fixed point. Three curves in the plot: the distance of solution to unstable plane(blue, generated by eigenvectors corresponding to two negative eigenvalues), unstable fixed point(black) and stable fixed point(red). As the solution converges to stable fixed point, the distance to stable fixed point converges to 0. Part (b), with initial point $(0.3650 + 100, 0.5159 + 100, 0.0494 + 100)$ adding 100 to stable fixed point, first the solution goes to unstable fixed point on the unstable plane, and then it converges to stable fixed point around t=600. Part (c), initial value $(0.3650 + 1000, 0.5159 + 1000, 0.0494 + 1000)$, add stable fixed point by 1000. The solution converges to unstable fixed point. As the solution converges to unstable fixed point, the distance to unstable plane(generated by eigenvectors corresponding to two negative eigenvalues) converges to 0. Also the distance to unstable fixed points converges to 0. Part (d), a time extension plot for part (c). Given enough long time t=1000, the convergency to stable fixed point is not observed.

Table 7.4: Time at unstable fixed points before converging to stable fixed point for Left data

Initial Point	Time(Approximate)
(0.3650+1,0.5159+1,0.0494+1)	t=100
(0.3650+50,0.5159+50,0.0494+50)	t=300
(0.3650+75,0.5159+75,0.0494+75)	t=400
(0.3650+120,0.5159+120,0.0494+120)	t=700
(0.3650+200,0.5159+200,0.0494+200)	t=1100
(0.3650+500,0.5159+500,0.0494+500)	t=2600
(0.3650+700,0.5159+700,0.0494+700)	$t > 9000$

7.1.4 Dynamics of 3-equation model with diffusion terms

Here we add diffusion terms to 3-equation model. x, y and z are dependent variables of t and u. Here t is the time variable and u is the 1-d spatial variable.

The 3-equation model with diffusion terms is:

$$\dot{x} = r_1 x(1 - x - y) - d_1 x - bxz + D_1 x_{uu},$$

$$\dot{y} = r_2 y(1 - x - y) + bxz - d_2 y + D_2 y_{uu}, \qquad (7.14)$$

$$\dot{z} = \epsilon_0 y - c_0 z + D_3 z_{uu}$$

We use Gaussian curves as our initial value for x, y and z: $x = y = z = \frac{e^{-u^2}}{10\sqrt{2\pi}}$.

The dynamics of x, y and z with left data are shown in Fig. 7.11. At t=200, the value of x, y and z converge to stable fixed point.
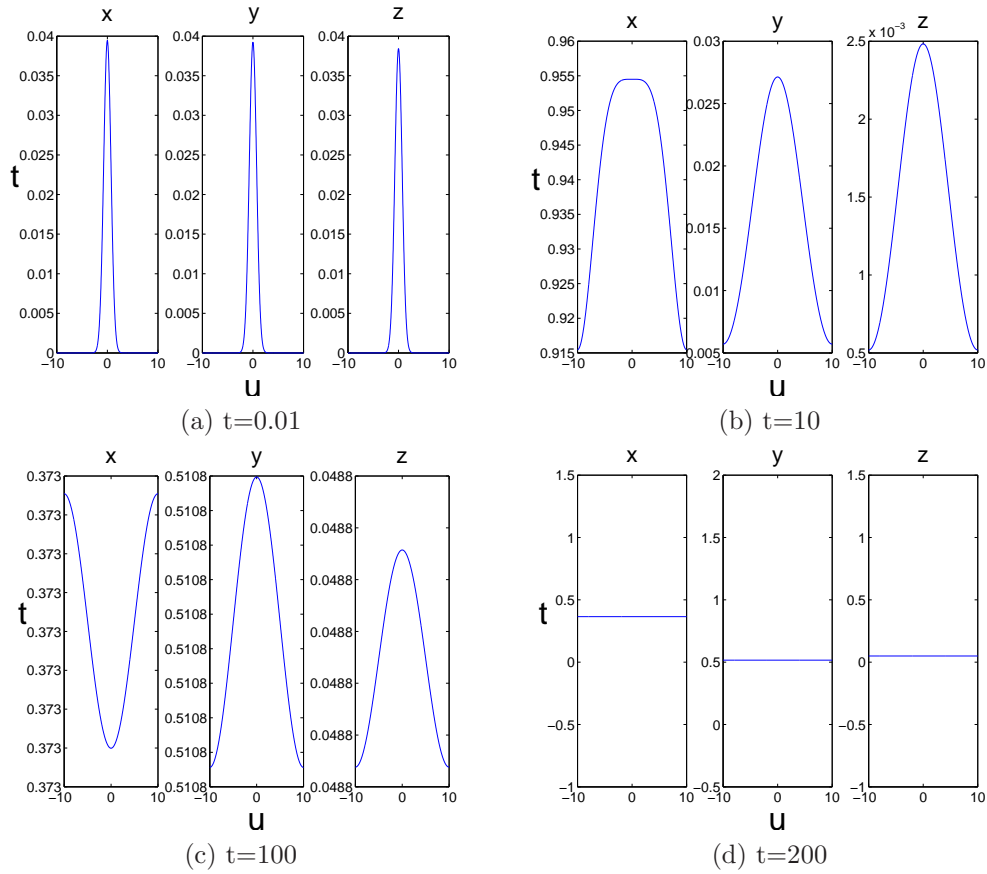
Figure 7.11: $D_1 = D_2 = D_3 = 1$. For left data, the solution x, y and z at t=0.01, t=10, t=100 and t=200.
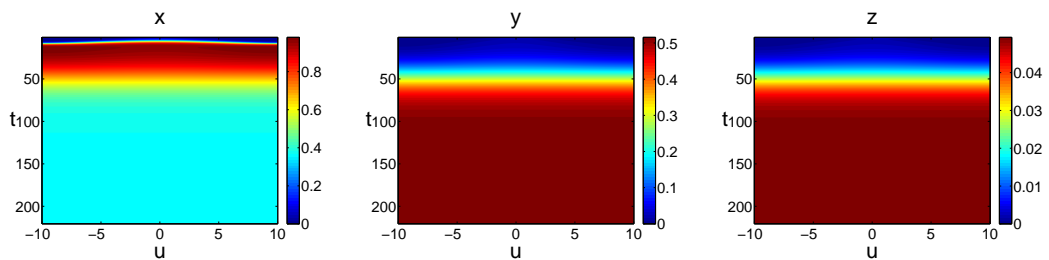
Figure 7.12: Left Data: time evolution of variable x, y and z.

The dynamics of x, y and z with right data as parameters are shown in Fig. 7.13. As time becomes large enough, it converges to stable fixed point.

(a) t=0　　　　　　　　　　　(b) t=10

(c) t=100　　　　　　　　　　(d) t=200
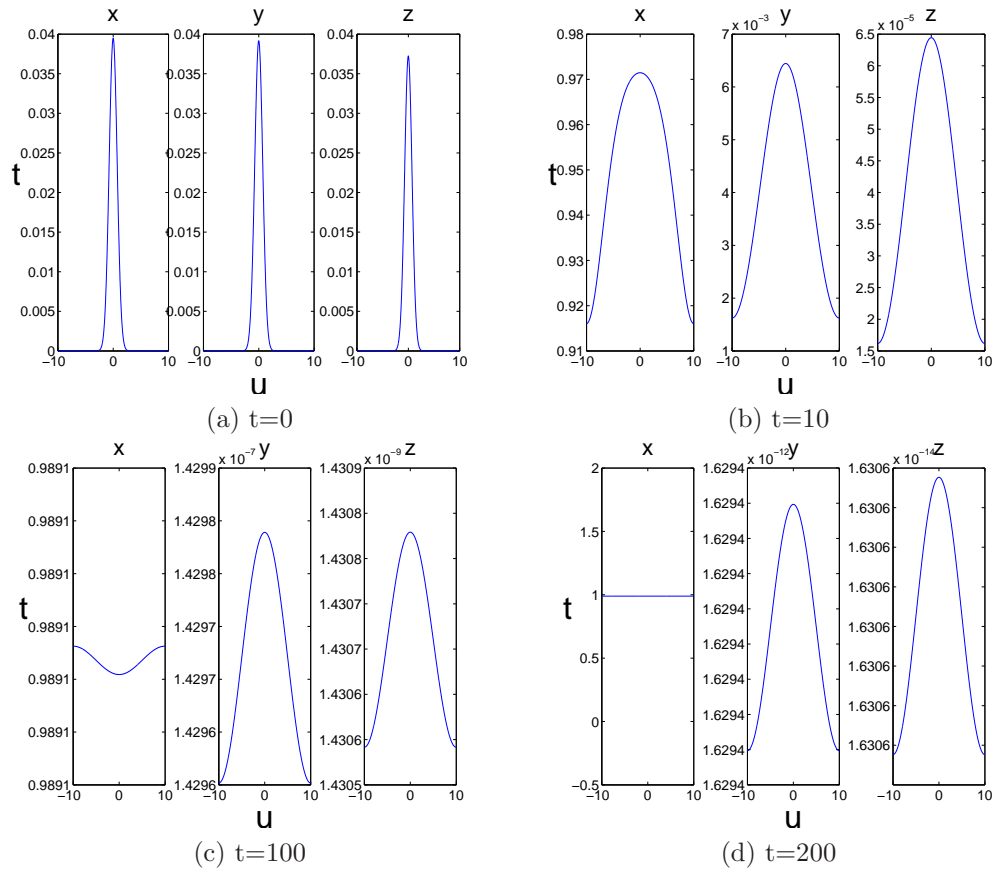
Figure 7.13: $D_1 = D_2 = D_3 = 1$. For right data, the solution x, y and z at t=0, t=10, t=100 and t=200.
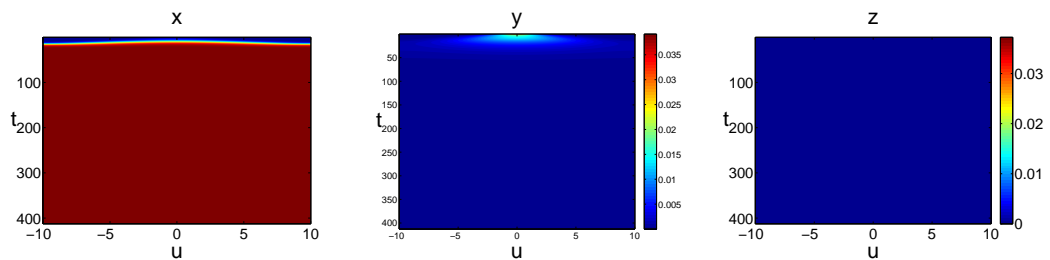
Figure 7.14: Right Data: time evolution of variable x, y and z.

7.2 2-equation model

7.2.1 2-equation model set up

For the original differential equation(7.1) in [29], using the following dimensionless variables and parameters

$$x = \frac{T}{T_{max}} \qquad y = \frac{I}{T_{max}} \tag{7.15a}$$

$$s = \frac{\hat{s}r_T}{(r_T - d_T)^2 T_{max}} \qquad b = \frac{p\beta T_{max}}{cr_T} \qquad q = \frac{\hat{q}}{r_T - d_T} \tag{7.15b}$$

$$r = \frac{r_I}{r_T} \qquad d = \frac{d_I r_T - d_T r_I}{r_T(r_T - d_T)} \qquad 1 - \theta = (1 - \epsilon)(1 - \eta), \tag{7.15c}$$

we get the dimensionless model [29]:

$$\dot{x} = x(1 - x - y) - (1 - \theta)byx + qy + s, \tag{7.16a}$$

$$\dot{y} = ry(1 - x - y) + (1 - \theta)byx - dy - qy, \tag{7.16b}$$

The table of fixed points and stability are listed below:

Table 7.5: Fixed points for left, middle and right data

Left data fixed points	Stability	Middle data fixed points	Stability	Right data fixed points	Stability
(0,0)	unstable	(0,0)	unstable	(0,0)	unstable
(1,0)	unstable	(1,0)	stable	(1,0)	stable
(0,0.63139)	unstable	(0,-3.34302)	unstable	(0,0.50551)	unstable
(0.36646,0.51793)	stable	(6.54303,-4.94554)	unstable	(50.89058,-49.74201)	unstable

7.2.2 Turing instability analysis when s=q=0, $\theta = 0$

The equation simplifies to:

$$\dot{x} = x(1 - x - y) - byx = f(x, y),$$

$$\dot{y} = ry(1 - x - y) + byx - dy = g(x, y) \tag{7.17}$$

Here we show analytically with the Routh-Hurwitz conditions, there can not be Turing instability. Set $f(x, y) = 0$ and $g(x, y) = 0$. We can solve four stable states: $(0, 0)$, $(1, 0)$, $(0, 1 - d/r)$ and $(\frac{db + d - br}{b(1 + b - r)}, \frac{b - d}{b(1 + b - r)})$.

The Jacobian matrix is:

$$
A = \begin{bmatrix} f_x & f_y \\ g_x & g_y \end{bmatrix} = \begin{bmatrix} 1 - 2x - y - by & -x(1 + b) \\ -ry + by & r(1 - x - 2y) - d + bx \end{bmatrix}
$$

Using the same technique with last section, we linearize around steady state (x_0, y_0), then the characteristic equation is $|\lambda I - A| = 0$, thus $\lambda^2 + (-f_x - g_y)\lambda + det(A) = 0$

By Routh-Hurwitz conditions, the stability conditions are:

$$f_x + g_y < 0 \tag{7.18}$$

$$det(A) > 0 \tag{7.19}$$

Plug the equilibrium points $(1, 0),(0, 1 - d/r)$ and $(\frac{db+d-br}{b(1+b-r)}, \frac{b-d}{b(1+b-r)})$ in formula of $f_x = 1 - 2x - y - by$ and $g_y = r(1 - x - 2y) - d + bx$. Solve inequalities $f_x + g_y < 0$ and $det(A) > 0$, we can find the stability region.

For equilibrium point $(0,0)$, $f_x = 1$, $g_y = r - d$, $f_y = 0$ and $g_x = 0$.

For equilibrium point $(1,0)$, $f_x = -1$, $g_y = b - d$, $f_y = -1 - b$ and $g_x = 0$.

For equilibrium point $(0, 1 - d/r)$, $f_x = 1 - (b + 1)(1 - \frac{d}{r})$, $g_y = -r + d$, $f_y = 0$ and $g_x = (b - r)(1 - \frac{d}{r})$.

For equilibrium point $(\frac{db+d-br}{b(1+b-r)}, \frac{b-d}{b(1+b-r)})$, $f_x = \frac{br-bd-d}{b(1+b-r)}$, $g_y = \frac{-r(b-d)}{b(1+b-r)}$, $f_y = -\frac{(db+d-br)(1+b)}{b(1+b-r)}$ and $g_x = \frac{(b-r)(b-d)}{b(1+b-r)}$.

For the above four equilibrium points $(0, 0),(1, 0),(0, 1-d/r)$ and $(\frac{db+d-br}{b(1+b-r)}, \frac{b-d}{b(1+b-r)})$, the corresponding stable region are: Never stable, $b < d$, $r > d + d/b$ and $rb/(1+b) < d < b$ respectively. This is shown in Table 7.6 and the same with results in [29].

87

Table 7.6: Equilibrium Points and Stable Region (Compare to [29] Table 3.1)

Equilibrium Points	Stable Region
$(0, 0)$	never
$(1, 0)$	$b < d$
$(0, 1 - d/r)$	$r > d + d/b$
$(\frac{db+d-br}{b(1+b-r)}, \frac{b-d}{b(1+b-r)})$	$rb/(1+b) < d < b$

We add diffusion terms:

$$\dot{x} = x(1 - x - y) - byx + D_1 \Delta x, \tag{7.20a}$$

$$\dot{y} = ry(1 - x - y) + byx - dy + D_2 \Delta y, \tag{7.20b}$$

Similarly, we have

$$\hat{A}(k^2) = \begin{bmatrix} -D_1 k^2 + f_x & f_y \\ g_x & -D_2 k^2 + g_y \end{bmatrix},$$

With the same technique in last section, we can derive the characteristic equation is

$$\lambda^2 + (D_1 k^2 + D_2 k^2 - f_x - g_y)\lambda + D_1 D_2 k^4 - D_1 g_y k^2 - D_2 f_x k^2 + det(A) = 0.$$

By Routh-Hurwitz conditions, the instability condition for Eq. (7.20) are:

$a_1 = D_1 k^2 + D_2 k^2 - f_x - g_y < 0$ or

$a_2 = D_1 D_2 k^4 - D_1 g_y k^2 - D_2 f_x k^2 + det(A) < 0$

As analyzed above, for all fixed points in stable states, $f_x < 0$ and $g_y < 0$. And we know D_1, D_2 and k^2, $det(A)$ are all positive. So neither condition a_1 or a_2 could be satisfied. For system given by Eq. (7.17), there is no possibility to achieve Turing instability.

7.2.3 Turing instability when s=q=0, $\theta \neq 0$

For this case, we multiply a factor $(1 - \theta)$ reducing the transmission rate b where θ is the dimensionless treatment efficacy. The Turing instability analysis is similar with previous section when $\theta = 0$. The only difference is to change b to $(1 - \theta)b$ in

all expression containing b. The equilibrium points are $(0,0),(1,0),(0,1-d/r)$ and $(\frac{db(1-\theta)+d-b(1-\theta)r}{b(1-\theta)(1+b(1-\theta)-r)}, \frac{b(1-\theta)-d}{b(1-\theta)(1+b(1-\theta)-r)})$.

In this case, the Jacobian matrix is

$$
A = \begin{bmatrix} f_x & f_y \\ g_x & g_y \end{bmatrix} = \begin{bmatrix} 1-2x-y-b(1-\theta)y & -x(1+b(1-\theta)) \\ -ry+b(1-\theta)y & r(1-x-2y)-d+b(1-\theta)x \end{bmatrix},
$$

The corresponding stability regions are shown below:

Table 7.7: Equilibrium Points and Stable Region

Equilibrium Points	Stable Region
$(0,0)$	never
$(1,0)$	$b(1-\theta) < d$
$(0,1-d/r)$	$r > d+d/(b(1-\theta))$
$(\frac{db(1-\theta)+d-b(1-\theta)r}{b(1-\theta)(1+b(1-\theta)-r)}, \frac{b(1-\theta)-d}{b(1-\theta)(1+b(1-\theta)-r)})$	$rb(1-\theta)/(1+b(1-\theta)) < d < b(1-\theta)$

For equilibrium point $(1,0)$, $f_x = -1$, $g_y = b(1-\theta)-d$, $f_y = -1-b(1-\theta)$ and $g_x = 0$.

For equilibrium point $(0,1-d/r)$, $f_x = 1-(b(1+\theta)+1)(1-\frac{d}{r})$, $g_y = -r+d$, $f_y = 0$ and $g_x = (b(1-\theta)-r)(1-\frac{d}{r})$.

For equilibrium point $(\frac{db(1-\theta)+d-b(1-\theta)r}{b(1-\theta)(1+b(1-\theta)-r)}, \frac{b(1-\theta)-d}{b(1-\theta)(1+b(1-\theta)-r)})$, $f_x = \frac{b(1-\theta)r-b(1-\theta)d-d}{b(1-\theta)(1+b(1-\theta)-r)}$, $g_y = \frac{-r(b(1-\theta)-d)}{b(1-\theta)(1+b(1-\theta)-r)}$, $f_y = -\frac{(db(1-\theta)+d-b(1-\theta)r)(1+b(1-\theta))}{b(1-\theta)(1+b(1-\theta)-r)}$ and $g_x = \frac{(b(1-\theta)-r)(b(1-\theta)-d)}{b(1-\theta)(1+b(1-\theta)-r)}$.

f_x and g_x are negative for all stable equilibrium points. So there is no Turing instability when $s = q = 0$, $\theta \neq 0$.

7.2.4 Turing instability when $s \neq 0$, $q \neq 0$, $\theta = 0$

In this case, the model can be written as:

$$\dot{x} = x(1-x-y)-byx+qy+s, \tag{7.21a}$$

$$\dot{y} = ry(1-x-y)+byx-dy-qy, \tag{7.21b}$$

89

The Jacobian matrix in this condition is:

$$A = \begin{bmatrix} f_x & f_y \\ g_x & g_y \end{bmatrix} = \begin{bmatrix} 1 - 2x - y - by & -x(1+b) + q \\ -ry + by & r(1-x-2y) - d + bx - q \end{bmatrix},$$

In this case, as shown in [29] section 3.2, there are four equilibrium points. Two of them are $(\frac{1-\sqrt{1+4s}}{2}, 0)$ and $(\frac{1+\sqrt{1-4s}}{2}, 0)$. The first one is never stable. The second one is never Turing unstable as $f_x < 0$ and $g_y < 0$. The other two equilibrium points stability analysis is more complex and is not fully discussed or proved here.

7.3 Numerical comparison between 2-equation and 3-equation models

In [29], the authors present a three species model for the interaction between uninfected hepatocytes, the infected cells and virus. The system is non-dimensionalized, resulting in the following equations.

$$\dot{x} = r_1 x (1 - x - y) - d_1 x - bxz, \tag{7.22a}$$

$$\dot{y} = r_2 y (1 - x - y) + bxz - d_2 y, \tag{7.22b}$$

$$\dot{z} = \epsilon_0 y - c_0 z \tag{7.22c}$$

Making the assumption that the concentration of infected cells is proportional to the concentration in the virus results in two species (infected and uninfected cells) system given by

$$\dot{x} = x(1 - x - y) - byx, \tag{7.23a}$$

$$\dot{y} = ry(1 - x - y) + byx - dy, \tag{7.23b}$$

The tables of fixed points and stability are listed below for the three data sets (left, middle and right) for the full three species system and two species system.

90

For the two-equation(species) fixed points, we show the fixed points for uninfected and infected cells. The third coordinate is the calculated viral concentration (V) from the assumption that it is proportional to the amount of infected cells (second coordinate). For the derivation of 2d system from 3d system, the approximation term is $V(\hat{t}) \approx \dfrac{(1-\epsilon)p}{c} I(\hat{t})$. Results are presented for left, middle and right data in table 7.8, 7.9 and 7.10. The fixed points and stability from two systems are comparable.

Table 7.8: Fixed points for Left data

2-equation fixed point	stability,	2-equation fixed points plus estimated V,	3-equation fixed point	stability
(0,0)	unstable	(0,0,0)	(0,0,0)	unstable
(1,0)	unstable	(1,0,0)	(0.9960,0,0)	unstable
(0,0.63139)	unstable	(0,0.63139,0.06040)	(0,0.6289,0.0602)	unstable
(0.36646,0.51793)	stable	(0.36646,0.51793,0.04955)	(0.3650,0.5159,0.0494)	stable

Table 7.9: Fixed points for Middle data

2-equation fixed point	stability,	2-equation fixed points plus estimated V,	3-equation fixed point	stability
(0,0)	unstable	(0,0,0)	(0,0,0)	unstable
(1,0)	stable	(1,0,0)	(0.9829,0,0)	stable
(0,-3.34302)	unstable	(0,-3.3430,-0.62826)	(0,-3.2857,-0.6175)	unstable
(6.54303,-4.94554)	unstable	(6.54303,-4.94554,-0.92942)	(6.4309,-4.8608,-0.9135)	unstable

Table 7.10: Fixed points for Right data

2-equation fixed point	stability,	2-equation fixed points plus estimated V,	3-equation fixed point	stability
(0,0)	unstable	(0,0,0)	(0,0,0)	unstable
(1,0)	stable	(1,0,0)	(0.9891,0,0)	stable
(0,0.50551)	unstable	(0,0.50551,0.00494)	(0,0.5000,0.0049)	unstable
(50.89058,-49.74201)	unstable	(50.89058,-49.74201,-0.48637)	(50.3354,-49.1994,-0.4811)	unstable

7.4 A new model and Turing instability analysis

Consider the new 2-equation model:

$$\dot{x} = r_1 x(1 - x - y) - bxy^2 + s - sx + D_1 \Delta y \tag{7.24a}$$

$$\dot{y} = r_2 y(1 - x - y) + bxy^2 - dy + D_2 \Delta y \tag{7.24b}$$

In this model, the infected population interacting with the uninfected term is changed from xy to xy^2. Also Turing instability is observed with a set of parameters. Fig. 7.15 represents the simulation result when $r_1 = 0.01$, $r_2 = 0.01$, $b = 1$, $s = 0.09$, $D_1 = 1$, $D_2 = 0.01$ and $d = 0.086$. In this case, the Turing instability is observed. Panel (a) shows the stable fixed points of the system without diffusion. Panel (b) shows the initial data with perturbation on fixed point in (a). Panel (c) shows solution to Eq. (7.24) after long time evolution. Panel (d) shows contour plots of solution x and y over time. Turing instability could be observed in (c) and (d). Notice in (c) and (d), at locations where more infected species exist, there are fewer uninfected and vice versa.
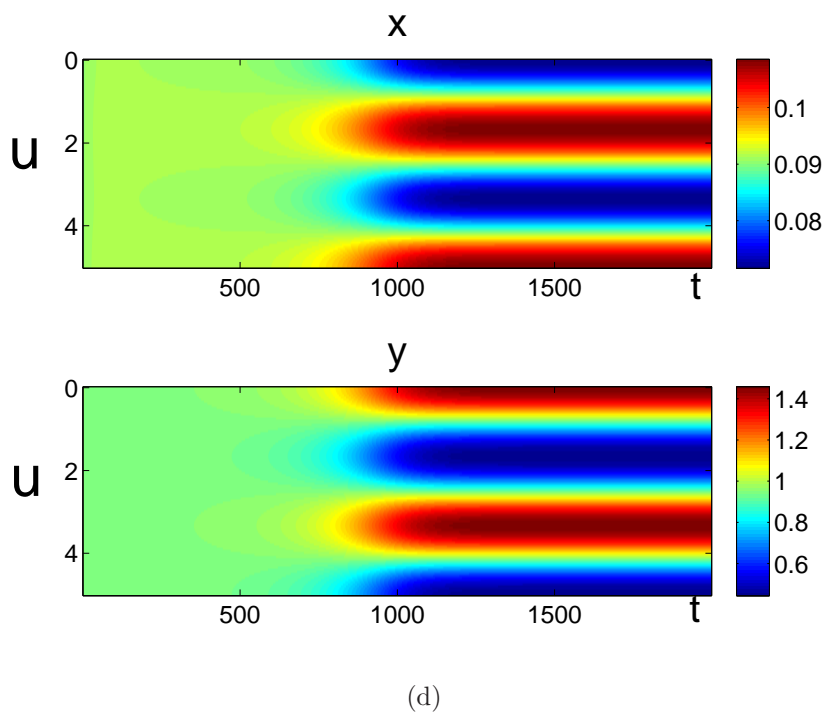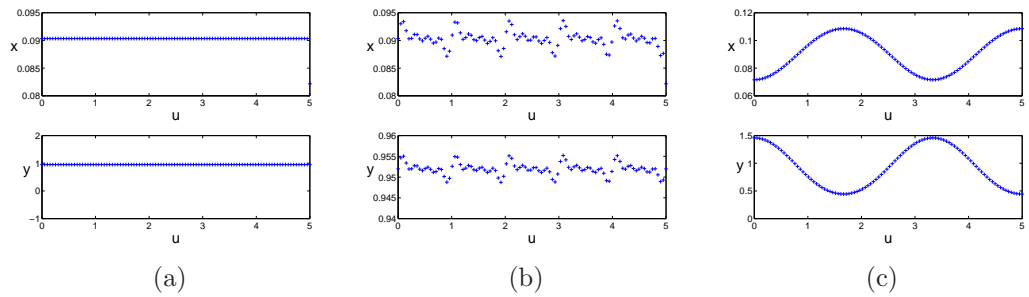
Figure 7.15: Panel (a) fixed points without diffusion. Panel (b) initial data with perturbation. Panel (c) solution to (7.24) after long time evolution. Panel (d) contour plots of the solutions over time.

7.5 Routh-Hurwitz condition

Routh-Hurwitz criteria is proposed by mathematicians E.J. Routh and A. Hurwitz to test whether the real part of the roots are negative [30]. As summarized in [30], the necessary and sufficient conditions on a_i, $i = 1, ..., n$ such that the zeros of $p(\lambda)$ have $Re(\lambda) < 0$ are the Routh-Hurwitz conditions.

Given the polynomial $p(\lambda) = \lambda^n + a_1\lambda^{n-1} + ... + a_{n-1}\lambda + a_n$, where the coefficients a_i are real constraints, $i = 1, ..., n$.

The Routh-Hurwitz conditions are:

$$D_1 = a_1 > 0, \qquad D_2 = \begin{vmatrix} a_1 & a_3 \\ 1 & a_2 \end{vmatrix} > 0, \qquad D_3 = \begin{vmatrix} a_1 & a_3 & a_5 \\ 1 & a_2 & a_4 \\ 0 & a_1 & a_3 \end{vmatrix} > 0,$$

$$D_k = \begin{vmatrix} a_1 & a_3 & \cdots & \cdots & \cdots \\ 1 & a_2 & a_4 & \cdots & \cdots \\ 0 & a_1 & a_3 & \cdots & \cdots \\ 0 & 1 & a_2 & \cdots & \cdots \\ \vdots & \vdots & \vdots & \vdots & \vdots \\ 0 & 0 & \cdots & \cdots & a_k \end{vmatrix} > 0, \qquad k = 1, 2, \ldots, n,$$

and $a_j = 0$ if $j > n$.

Here D_k is the determinant of the kth matrix (Hurwitz matrix).

Routh-Hurwitz criteria for n=2, 3 and 4.

$n = 2$: $a_1 > 0$ and $a_2 > 0$

$n = 3$: $a_1 > 0$, $a_3 > 0$, and $a_1a_2 > a_3$

$n = 4$: $a_1 > 0$, $a_3 > 0$, $a_4 > 0$, and $a_1a_2a_3 > a_3^2 + a_1^2a_4$

CHAPTER 8

TUMOR DYNAMICS

In this chapter, we try to find an optimal radiotherapy method for malignant brain tumor patients. In [47], the Fisher-Kolmogorov (FK) type equation (8.1) is proposed to simulate the growth of brain tumor

$$u_t = Du_{xx} + \rho u(1 - u) \tag{8.1}$$

FK equation is a reaction-diffusion equation and applied in population dynamics [31, 51, 52]. In this dissertation, FK equation is used in tumor modeling [49, 48, 50]. The authors in [47] derive a system of effective particle methods (ODEs) to describe the dynamics of a single front and localized solutions of Eq. (8.1). These ODEs describe the evolution of some important dynamical quantities. We compare the solutions of the effective particle methods (ODEs) and the FK equations (PDEs). The comparison shows good quantitative agreement. Then we develop the tumor model with radiotherapy. We analyze the single front and localized solution for ODEs and PDEs under the condition of radiotherapy. A comparison of the ODEs with radiotherapy and dynamics of PDE with radiotherapy shows good quantitative agreement. Different radiotherapy methods are designed and simulated to determine the optimal therapy which gives the longest survival time for the patient. Also we consider the radiotherapy for low grade glioma which provides smaller total radiation than before. Besides this, we compare the radiotherapy effects of different radiotherapy methods when keeping the damage to the normal tissue the same.

8.1 PDE and ODE modeling tumor dynamics with single front solution

In [47], Fisher-Kolmogorov Equation (8.1) is applied to simulate the growth of brain tumor. In this model, $u(x,t)$ represents the tumor density which is a time and space dependent variable. For the two parts of FK equation, $u_t = Du_{xx}$ is a heat equation which describes the distribution property of tumor cells. D is the diffusion coefficient. The second term $u_t = \rho u(1-u)$ is a logistic model which describes the proliferation of the tumor cells and ρ is proliferation coefficient. The FK equation describes the proliferation and diffusion process of tumor cells. As $u(x,t)$ is the tumor density, so the range is $u \in [0,1]$.

In [47], a set of effective equations are derived to describe the single front solution of FK equation. The parameters in the solutions are ruled by a system of ODEs as shown and proved in [47]. In our simulation, we set coefficients $D=1$ and $\rho=1$. For other values of D and ρ, we can convert them to 1 through a variable transformation.

There are nonnegative traveling wave solutions $u = u(z)$ where $z = x - ct$ to Fisher-Kolmogorov equation $u_t = Du_{xx} + \rho u(1-u)$. It satisfies the boundary conditions $\lim_{z \to +\infty} u(z) = 0$ and $\lim_{z \to -\infty} u(z) = 1$ and solves the ODE $Du''(z) + cu'(z) + \rho u(1-u) = 0$. As introduced in [47], we approximate the dynamics of the ODEs with the ansatz

$$u(x,t) = A(t)f(\frac{x - X(t)}{\omega(t)}) \tag{8.2}$$

Here $A(t)$ is the wave amplitude. $X(t)$ is the front position and $\omega(t)$ is the front width. When $D = \rho = 1$, the only simple explicit solution of the Fisher-Kolmogorov equation is $u(z) = \dfrac{1}{(1 + e^{z/\sqrt{6}})^2}$ [56]. In [47], the front profile is chosen as

$$u(x,t) = \frac{A(t)}{(1 + e^{(x - X(t))/\omega(t)})^2} \tag{8.3}$$

96

In [47], three integral quantities for the front analysis are defined:

$$I_1(t) = \int_{-\infty}^{\infty} u_x dx \tag{8.4a}$$

$$I_2(t) = \frac{\int_{-\infty}^{\infty} x u_x dx}{I_1} \tag{8.4b}$$

$$I_3(t) = \frac{\int_{-\infty}^{\infty} (x - I_2)^2 u_x dx}{I_1} \tag{8.4c}$$

Here I_1, I_2 and I_3 represent the L_1 norm (number of particles), center of mass and width of the gradient of the density u. Plug expression of u (8.3) into (8.4). Simplify the equations and we can get the following [47]:

$$I_1 = -A(t) \tag{8.5a}$$

$$I_2 = X(t) - \omega(t) \tag{8.5b}$$

$$I_3 = (\frac{\pi^2}{3} - 1)\omega^2 \tag{8.5c}$$

Then we can obtain the equations for I_1, I_2 and I_3.

$$\frac{dI_1}{dt} = -\rho A(t)(1 - A(t)) \tag{8.6a}$$

$$\frac{dI_2}{dt} = \frac{5}{6}\rho A(t)\omega(t) \tag{8.6b}$$

$$\frac{dI_3}{dt} = 2D - \frac{1}{3}\rho A(t)\omega^2(t). \tag{8.6c}$$

Finally we can get ODEs for the evolution of effective particles $A(t)$, $X(t)$ and $\omega(t)$ [47]:

$$\frac{dA(t)}{dt} = \rho A(t)(1 - A(t)) \tag{8.7a}$$

$$\frac{dX(t)}{dt} - \frac{d\omega(t)}{dt} = \frac{5}{6}\rho A(t)\omega(t) \tag{8.7b}$$

$$\frac{d\omega^2(t)}{dt} = \frac{6D}{\pi^2 - 3} - \frac{\rho}{\pi^2 - 3}A(t)\omega^2(t). \tag{8.7c}$$

These ODEs rule the dynamics of front parameters A, ω and X as introduced in [47]. In the following work, we will compare the front parameters solved from both the ODEs and FK equation (PDE). We now discuss about the initial values. We would like to introduce two initial values. If the surgery achieves gross tumor resection (GTR), there is relatively less tumor density left in the body. If the surgery achieves subtotal resection (STR), there is relatively greater tumor density left in the body. Initial conditions for the PDE are given by $u(x,0) = 0.01e^{-x^2}$ for GTR and $u(x,0) = 0.1e^{-x^2}$ for STR. The initial condition for the ODE is in the form $u(x,0) = \dfrac{A(0)}{[1 + e^{(x-X(0))/w(0)}]^2}$ as introduced in Eq. (8.3). The Least Square Method is used to solve the value of $A(0)$, $X(0)$ and $w(0)$. By minimizing formula $\int_0^\infty (u(x,0) - \dfrac{A(0)}{[1 + e^{(x-X(0))/w(0)}]^2})^2dx$, we get $A(0) = 0.0121$, $X(0) = 1.0992$, $w(0) = 0.4376$ for GTR and $A(0) = 0.1213$, $X(0) = 1.0992$, $w(0) = 0.4372$ for STR. With these initial conditions, we can solve A, ω and X from the ODEs (8.7). Then we can get $u(x,t)$ through Eq. (8.3).

We solve the PDE (8.1) for $u(x,t)$ with the same initial conditions. In Fig. 8.1(a), we show the comparison of the evolution of u with GTR initial condition. The dashed red curve is corresponding to the ODE solutions. The solid blue curve is corresponding to the PDE solutions. The PDE and ODE results show good quantitative agreement. Similarly, in Fig. 8.1(b), we show the comparison of the evolution of u with STR initial condition.

Next we compare the front parameters solved from both PDE and ODEs. We can solve A, ω and X from the ODEs with GTR initial condition. Then we calculate dx/dt by differentiate X with respect to t. We plot the quantities A, ω and dx/dt

(a) A0=0.0121, w0=0.4376, X0=1.0992   (b) A0=0.1213, w0=0.4372, X0=1.0992
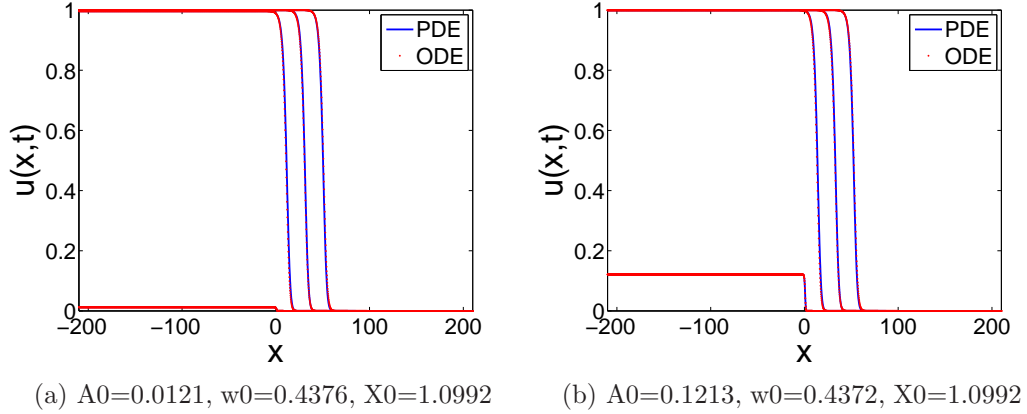
Figure 8.1: This is a comparison of the evolution of u for single front solutions of Fisher-Kolmogorov equation (solid curves) with that provided by the effective particle equations (dashed curves) for various times: t=0, 10, 20, 30 from the left to right (low to the high) profiles. The diffusion coefficient is $D = 1$ and the growth rate $\rho = 1$.

in Fig. 8.2. From PDE (FK equation) we solve $u(x,t)$ with GTR initial condition. Then from Eq. (8.4), we can solve I_1, I_2 and I_3. Then from Eq. (8.5), we solve A, ω and dx/dt. We put the results in Fig. 8.2 and compare the evolution of amplitude A, width w and velocity dX/dt of the single front obtained from both ODEs and PDE. The solutions obtained from ODEs and PDE show excellent agreement. In this way, analyzing the dynamics from the ODEs provides a relatively convenient way to study the tumor front as discussed in [47].

8.2   Simulation results for single front solution with radiation

In this section, radiotherapy is taken into consideration. In the following results for the single front we use exclusively the initial data based upon $u(x,0) = 0.01e^{-x^2}$ (GTR). When considering the effect of radiotherapy, we focus on the reduction of tumor cells. We define the survival probability of the tumor cell of each radiotherapy to be s which is a function of radiation amount the patient is exposed to per dose. For each dose of radiation, the density of the tumor cells will be re-

| (a) A | (b) w | (c) dx/dt |
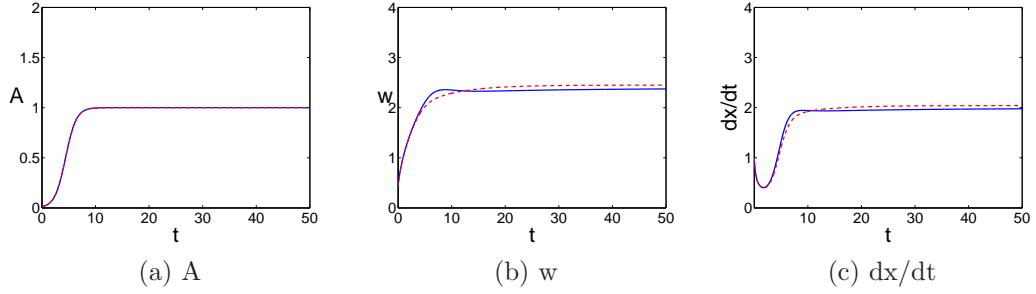
Figure 8.2: Similar with the comparison in [47] Fig. 2.1, this is a comparison of the evolution of amplitude A, width of the solution w and $\frac{dX}{dt}$ for single front solutions of PDE (solid curves) with the solutions of ODE (dashed curves). Coefficients D=1 and $\rho = 1$. The initial data is given by Eq. (8.3) with $A(0) = 0.0121$, $w(0) = 0.4376$, $X(0) = 1.0992$.

duced to $u \cdot s$. The formula of s is selected as $s = e^{-\alpha d - \beta d^2}$ where d represents the amount of radiation per dose [47][53]. Generally, the ratio $\alpha/\beta = 10$ if u represents tumor cells. (For normal cells, the ratio is smaller e.g. $\alpha/\beta = 3$) [47]. To illustrate it, we assume the radiation is 2 Gy each dose, 30 fractions in total. The parameter values are chosen as $\alpha = 0.083$, $\beta = 0.0083$. Then the survival probability is $s = e^{-0.083 \times 2 - 0.0083 \times 4} = 0.82$. This means that for each dose of radiation, the density u(x,t) is reduced to 82 percent. For the PDE case (8.1), the tumor cell density function $u(x, t)$ is updated by multiplying a survival probability s, $u(x, t) = u(x, t) \cdot s$. For ODE case, when radiation is applied, by Eq. (8.5a) and (8.4a), the amplitude $A(t)$ is updated by $A(t) = A(t) \cdot s$. For each dose of radiotherapy, the amplitude of the tumor cells $A(t)$ will be updated once. A standard dosage for radiotherapy is 2Gy/dose (The gray (symbol: Gy) is the unit of radiation), 30 doses in total with the total radiation 60 Gy. Suppose the radiation is provided from Monday to Friday, 5 days a week, then the total radiotherapy period is 6 weeks.

To find the optimal radiotherapy, 21 radiation methods were applied and compared. The radiation methods include different radiation amounts per dose (0.5, 1, 1.5, 2, 2.5, 3 and 3.4 Gy) and different interval time (one dose per day, twice per

100

(a) A   (b) w localized solution   (c) dx localized solution
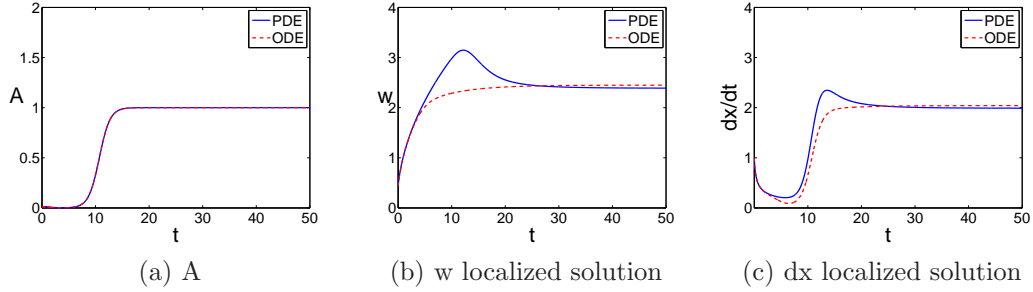
Figure 8.3: Comparison of the evolution of single front solutions of the PDE (solid curves) with the solutions of the ODE (dashed curve) under radiotherapy 0.5 Gy per dose twice a day. The initial data is given by Eq. (8.3) with $A(0) = 0.0121$, $w(0) = 0.4376$, $X(0) = 1.0992$. The corresponding ODEs are solved taking the $A(0)$, $w(0)$ and $X(0)$ as initial values for A(t), w(t) and X(t).

day and with a gap month in the middle of the whole radiation period). In the computation, no radiation is applied on Saturday and Sunday. '0.5 per 12 hour' is the combination of 0.5 Gy per 12 hours and 2 fractions per day from Monday through Friday. '0.5 per day with month gap' is the combination of 0.5 Gy per day from Monday to Friday. The 60 Gy of total radiation is equally separated into two parts with 30 Gy each part. Between the two parts, there is a gap month. In the gap month, no radiation is given. Then 1 Gy, 1.5 Gy, 2 Gy, 2.5 Gy, 3 Gy and 3.4 Gy each dose under different time period are tested. The total radiation for each experiment is kept to be 60 Gy. The maximum amount for one dose is 3.4 Gy which is thought to be maximum radiation a patient can tolerate without burning the normal tissue.

Fig. 8.3 shows the comparison of the evolution of front parameters solved from PDE and ODEs under radiotherapy of 0.5 Gy per dose and twice per day. The front parameters include amplitude A, width ω and velocity dx/dt. The results obtained from ODEs and PDE show good quantitative agreement. In this way, under radiotherapy, analyzing the dynamics from the ODEs also provides a relatively convenient way to study the tumor growth front.

(a) 0.5Gy 2 dose per day

(b) 0.5Gy 2 dose per day
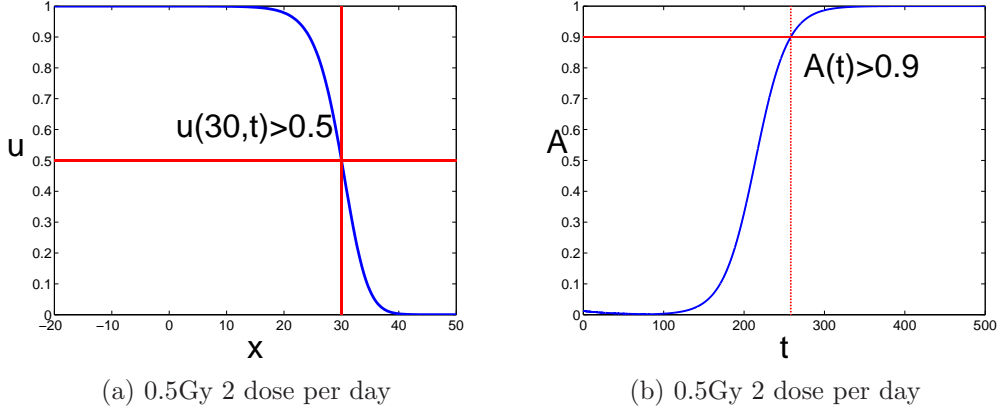
Figure 8.4: This figure is used to illustrate the criterion 1 and criterion 2 in cutoff to calculate the lifetime.

As the tumor becomes large, it will be fatal for the patient. To measure the patients' lifetime, we select two cutoff criteria. The first cutoff criterion occurs when $u(30, t) = 0.5$, i.e., when the density at location $x = 30$ equals 0.5. The second cutoff criterion occurs when the amplitude $A = 0.9$. The ODEs and PDE results are compared for both cutoff criteria. Fig. 8.4 illustrates both criteria. In panel (a), it is cut off as $u(30, t)$ increases to 0.5. In panel (b), it is cut off as $A(t)$ increases to 0.9. The cut off criteria are selected to make the simulation results comparable to lifetime in clinical data.

The method to calculate lifetime is done as follows. Suppose the solution to Fisher-Kolmogorov equation $u_t = Du_{xx} + \rho u(1 - u)$ is $u(\hat{x}, \hat{t})$. The solution to $u_t = u_{xx} + u(1 - u)$ is $u(x, t)$. $x = \hat{x}\sqrt{\rho/D}$, $t = \hat{t}\rho$. In previous work, The "cut off" at radius $\hat{x} = 30mm$ with density $u(30, \hat{t}) = 0.5$. We calculate the corresponding x. Use the 'cut off' criteria $u(x, t) = \frac{A(t)}{[1+e^{(x-x_0(t))/w(t)}]^2} = 0.5$ to calculate t. Through formula $\hat{t} = t/\rho$,the comparable lifetime $\hat{t}$ could be obtained. Here $\rho = 0.05$, $D = 0.06$.

In Table 8.1, the computed lifetimes are listed for the single front for both the ODE and PDE using the cutoff $u(30, t) = 0.5$. In Table 8.2, the lifetimes are listed for a single front using cutoff $A = 0.9$. Fig. 8.5 is a plot of the lifetime data shown in

Table 8.1 and 8.2. From the tables, the longest lifetime is achieved at the radiation 3 Gy each dose, time interval is 12 hours. For cutoff criterion 1 ($u(30, t) = 0.5$), the longest lifetime is 508 days and 460 days for PDE and ODE respectively. For criterion 2, the longest lifetime is 288 days for both PDE and ODE. This is concluded in Table 8.3. Notice that by using criteria 2 ($A = 0.9$), the PDE and ODE results agree better.

Table 8.1: Lifetime for Single front (cut off with u)

Method No.	Dose(Gy)	ODE	PDE
1	0.5 per day	461	427
2	1 per day	465	429
3	1.5 per day	470	433
4	2 per day	474	436
5	2.5 per day	479	439
6	3 per day	484	442
7	3.4 per day	490	447
8	0.5 per 12 hour	480	440
9	1 per 12 hour	486	444
10	1.5 per 12 hour	491	448
11	2 per 12 hour	497	452
12	2.5 per 12 hour	499	453
13	3 per 12 hour	508	460
14	3.4 per 12 hour	505	457
15	0.5 per day with month gap	463	427
16	1 per day with month gap	467	431
17	1.5 per day with month gap	473	434
18	2 per day with month gap	478	439
19	2.5 per day with month gap	479	439
20	3 per day with month gap	490	447
21	3.4 per day with month gap	483	442

Table 8.2: Lifetime for Single front(cut off with A=0.9)

Method No.	Dose(Gy)	ODE	PDE
1	0.5 per day	244	244
2	1 per day	242	242
3	1.5 per day	247	247
4	2 per day	252	252
5	2.5 per day	257	257
6	3 per day	262	262
7	3.4 per day	268	268
8	0.5 per 12 hour	258	258
9	1 per 12 hour	264	264
10	1.5 per 12 hour	270	270
11	2 per 12 hour	276	276
12	2.5 per 12 hour	278	278
13	3 per 12 hour	288	288
14	3.4 per 12 hour	284	284
15	0.5 per day with month gap	258	258
16	1 per day with month gap	245	245
17	1.5 per day with month gap	250	250
18	2 per day with month gap	256	256
19	2.5 per day with month gap	257	257
20	3 per day with month gap	268	268
21	3.4 per day with month gap	261	261
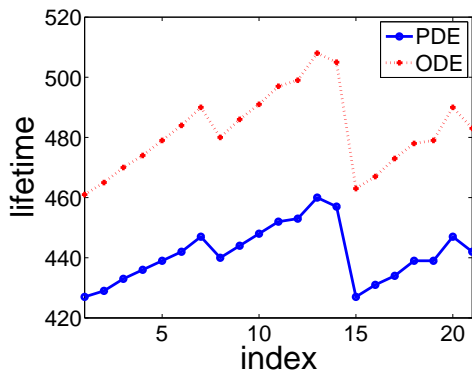
(a) single front cut off u   (b) single front cut off with A
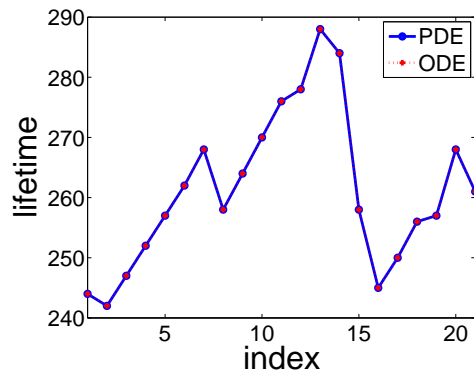
Figure 8.5: Plot of lifetime with different cutoffs. The x-axis 0-20 shows the 21 radiation methods listed in table 1 and 2. The y-axis is the lifetime corresponding to each radiotherapy method.

Table 8.3: Longest lifetime for Single Front

Single Front	ODE	PDE
Criterion 1 u(30,t)=0.5	508	460
Criterion 2 A(t)=0.9	288	288

8.3 PDE and ODE modeling tumor dynamics with localized solution

In [47], the localized solution for the ODEs is derived. The ansatz for localized solution is given as

$$u(x,t) = A(t)\left(\frac{1}{1 + e^{(x-X(t))/w(t)}} - \frac{1}{1 + e^{(x+X(t))/w(t)}}\right)^2 \tag{8.8}$$

In [47], the quantities defined for effective method are:

$$n(t) = \int_{-\infty}^{\infty} u\,dx \tag{8.9a}$$

$$\sigma^2(t) = \frac{1}{n(t)} \int_{-\infty}^{\infty} x^2 u\,dx \tag{8.9b}$$

$$\gamma(t) = -\int_{0}^{\infty} u_x\,dx \tag{8.9c}$$

Here $n(t)$ represents the total mass. σ^2 represents the variance of the density distribution. $\gamma(t)$ gives the right-front size. Plugging (8.8) in (8.9), a system of ODEs consisting $A(t)$, $\omega(t)$ and $X(t)$ could be obtained. The details are shown in [47] section 3.3. We solve the ODEs and FK equation (PDE) with initial condition in the form of Eq. (8.8) and compare the results.

In Fig. 8.6, we show the evolutions of localized solution u obtained from solving the PDE and the ODEs. The solutions are shown and compared at time $t = 0, 3, 10$
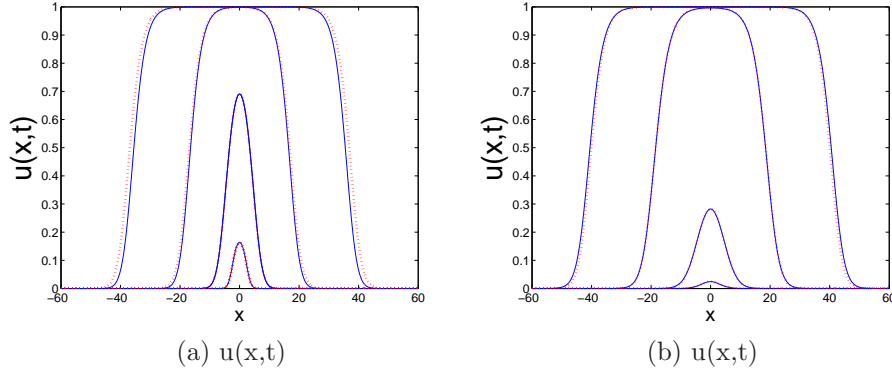
Figure 8.6: Same with the comparison in [47] Fig. 3.1, this is a comparison of the evolution of localized solutions of the Fisher-Kolmogorov equation (8.1) (solid curves) with that provided by the ansatz (8.8) (dasher curves) for various time: t=0, 3, 10, 20. D=1 and $\rho = 1$. The initial data is given with (a) $A_0 = 0.2$, $w_0 = 1$, and $X_0 = 3$;(b) $A_0 = 0.9$, $w_0 = 3$, and $X_0 = 1$

and 20. The initial conditions for the two examples are $A(0) = 0.2$, $w(0) = 1$ and $X(0) = 3$ in Fig. 8.6 (a) and $A(0) = 0.9$, $w(0) = 3$ and $X(0) = 1$ in Fig. 8.6 (b). This comparison is done in [47] Figure 3.1.

In Fig. 8.7, we show the evolution of the localized solution of A, w and $\frac{dX}{dt}$ for the PDE and ODE with initial values $A(0) = 0.5$, $w(0) = 1$ and $X(0) = 2$. The solutions from ODE and PDE show good quantitative agreement. This comparison is done in [47] Figure 3.2.

8.4   Simulation results for localized solution with radiation

In Fig. 8.8, we give a comparison of the ODE and PDE results for a localized solution with 2 Gy per dose and one dose per day. The initial condition is $A(0) = .5$, $w(0) = 1$ and $X(0) = 2$. When radiotherapy is applied, the front of the traveling wave is changed.

In Fig. 8.9, we present two cutoff criteria for localized solution with initial data $A(0) = 0.5$, $w(0) = 1$ and $X(0) = 2$. In this plot, the time t and space x is scaled to the solution with parameters $\rho = 0.05$ and $D = 0.06$.

107

(a) A localized solution   (b) w localized solution   (c) dx0 localized solution
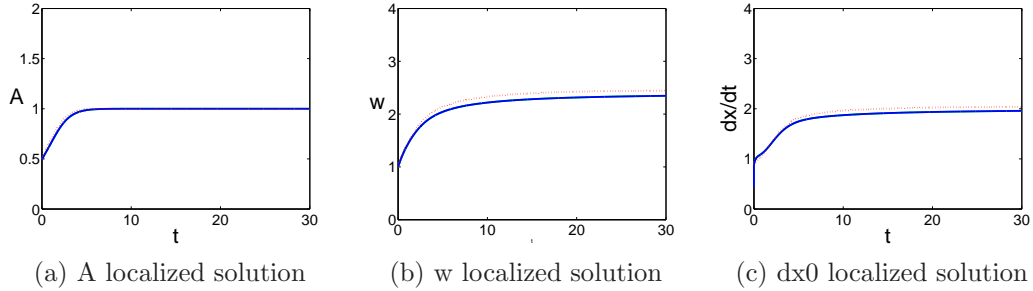
Figure 8.7: Same with the comparison in [47]. This is a comparison of the evolution of localized solutions of the Fisher-Kolmogorov equation (solid curves) with the solutions of the effective particle method (dashed curves). D=1, $\rho = 1$. The initial data is given by Eq. (8.8) with A(0)=0.5, w(0)=1, X(0)=2.

(a) A localized solution with (b) w localized solution with (c) dx localized solution with
radiation   radiation   radiation
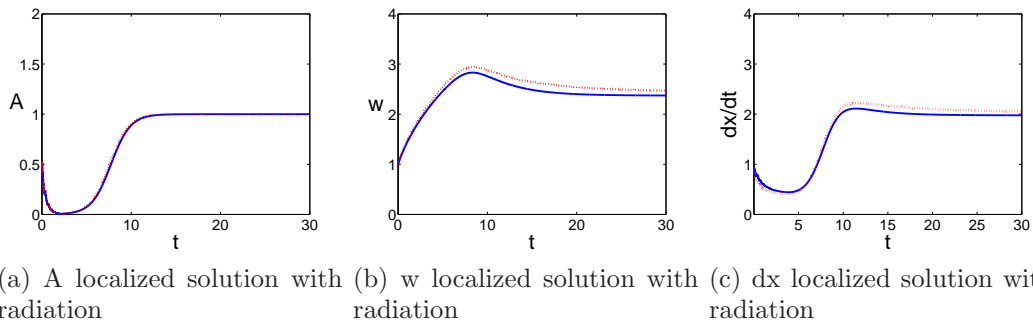
Figure 8.8: Plot of A, w and dx/dt. Comparison of the evolution of localized solutions of the PDE (solid curves) with the solutions of the ODE (dashed curves) under radiotherapy of 2 Gy per dose and one dose per day. The initial data is given by Eq. (8.8) with A(0)=0.5, w(0)=1, X(0)=2.

(a) contour plot of u(x,t)   (b) plot of u with u(30,t)=0.5   (c) plot of A with A(t)=0.9
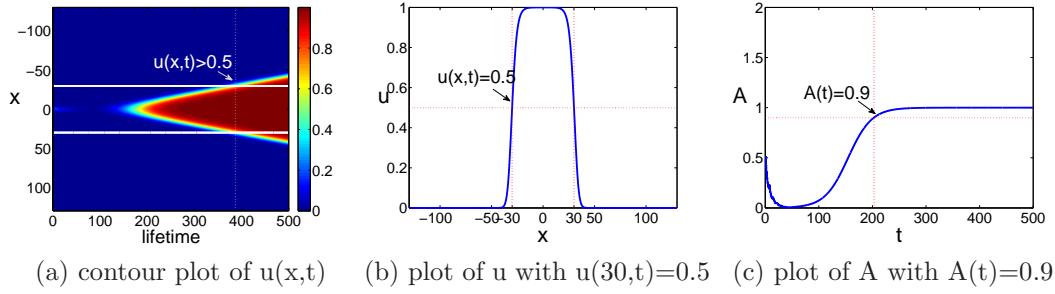
Figure 8.9: Comparison of cut off criteria $u(30,t) = 0.5$ and $A(t) = 0.9$. Initial value is $A(0) = 0.5$, $w(0) = 1$, $X(0) = 2$. In (a)-(c), the solution is solved from PDE. The radiation is 2 Gy per dose and once per day.

In Tables 8.4 and 8.5, we list the lifetimes from 21 therapies for the localized solution to both the PDE and ODE. The lifetime is plotted in Fig. 8.10 for comparison.

Table 8.4: Lifetime for Localized solution(cut off with u)

Method No.	Dose(Gy)	ODE	PDE
1	0.5 per day	347	357
2	1 per day	368	377
3	1.5 per day	370	380
4	2 per day	373	382
5	2.5 per day	373	385
6	3 per day	379	388
7	3.4 per day	379	392
8	0.5 per 12 hour	359	387
9	1 per 12 hour	381	390
10	1.5 per 12 hour	385	393
11	2 per 12 hour	388	397
12	2.5 per 12 hour	386	398
13	3 per 12 hour	396	405
14	3.4 per 12 hour	388	402
15	0.5 per day with month gap	368	378
16	1 per day with month gap	369	379
17	1.5 per day with month gap	372	382
18	2 per day with month gap	376	385
19	2.5 per day with month gap	376	385
20	3 per day with month gap	384	393
21	3.4 per day with month gap	379	388

8.5 Low Grade Glioma radiation simulation results

In this section, Low Grade Glioma Radiotherapy experiment is simulated. Low grade glioma has lower proliferation and patients have longer lifetime [61, 63, 65, 47]. For low grade glioma radiotherapy, the standard dose is 1.8 Gy per dose, the total dosage is 54 Gy [47]. We keep the time interval as a free parameter. The radiotherapy is twice per day, once per day, once per week, twice per week, three times per week and four times per week. For example, once per week, we try to give radiation on every Monday. If we give every Tuesday or Wednesday or Thursday or Friday, the clinical results are similar. The cut off criterion 1 $(u(30, t) = .5)$ and criterion 2 $(A(t) = 0.9)$ are the same with criterion in last section. Table. 8.7 and 8.8 show the simulation results with 1.8 Gy per dose but varying the time interval.

Table 8.5: Lifetime for Localized solution(cut off with A=0.9)

Method No.	Dose(Gy)	ODE	PDE
1	0.5 per day	222	223
2	1 per day	193	196
3	1.5 per day	195	198
4	2 per day	199	203
5	2.5 per day	198	208
6	3 per day	209	213
7	3.4 per day	208	219
8	0.5 per 12 hour	209	212
9	1 per 12 hour	212	215
10	1.5 per 12 hour	218	221
11	2 per 12 hour	224	227
12	2.5 per 12 hour	220	229
13	3 per 12 hour	236	239
14	3.4 per 12 hour	224	235
15	0.5 per day with month gap	249	249
16	1 per day with month gap	202	205
17	1.5 per day with month gap	201	204
18	2 per day with month gap	205	209
19	2.5 per day with month gap	205	209
20	3 per day with month gap	220	217
21	3.4 per day with month gap	209	212

Next we consider the reduction of normal cells with radiation. The damage function is $nd(1 + \frac{d}{\alpha/\beta})$ and $\alpha\beta = 3$ for normal cells. Here d represents the radiation per dose and n means the number of doses. For standard low grade glioma radiation 1.8 Gy per dose, 30 doses in total, keeping equivalent damage to normal cells with 0.9 Gy per dose, we can calculate the number of doses by $\frac{n_1 d_1}{n_2 d_2} = \frac{1+\frac{d_2}{3}}{1+\frac{d_1}{3}}$. So the amount of radiation is $n_2 = 74$ for the same damage to normal cells. Table. 8.9 and Table. 8.10 show the lifetime of patients given the same damage to the normal tissue during radiation. In the same way, two criteria are used for comparison. 1.8 Gy each dose and 30 doses in total is the standard dosage used in these two tables. We keep the damage to the normal tissue the same. The corresponding lifetime are listed in the Tables 8.9 and 8.10. The radiation methods are 0.45, 0.9, 1.35, 1.8, 2.25, 2.7, 3.15 and 3.6 Gy

(a) localized solution cut off with u   (b) localized solution cut off with A
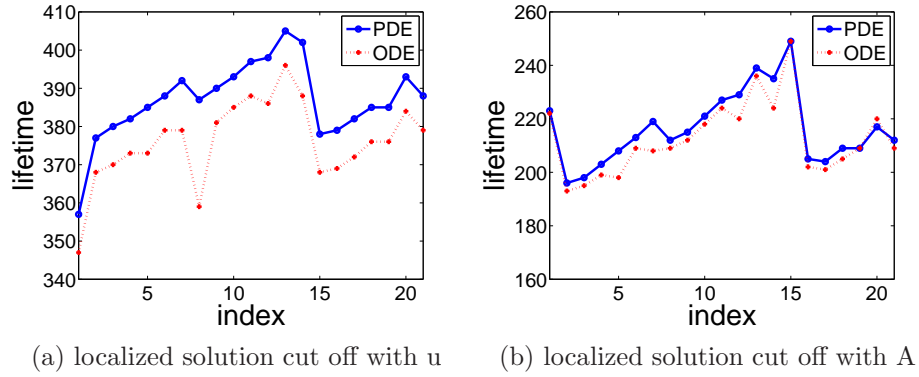
Figure 8.10: Comparison of the lifetime

Table 8.6: Longest lifetime for Localized Solution

Localized Solution	ODE	PDE
Criterion 1 u(30,t)=0.5	396	405
Criterion 2 A(t)=0.9	249	249

per dose, one dose per day by keeping damage to the normal tissue the same. If given
one dose per day, the small amount 0.45 per dose shows the best result.

Table 8.7: Low Grade Glioma radiation: Localized solution(cut off with u(30,t)=0.5)

Dose(Gy)	ODE	PDE
twice per day	378	333
once per day	365	331
once per week	368	333
twice per week	366	332
three times per week	365	331
four times per week	365	330

Table 8.8: Low Grade Glioma radiation: Localized solution(cut off with A(t)=0.9)

Dose(Gy)	ODE	PDE
twice per day	206	210
once per day	185	188
once per week	252	252
twice per week	193	197
three times per week	187	191
four times per week	185	189

Table 8.9: Low Grade Glioma radiation: Localized Solutions Case - normal tissue damage the same(cut off with u(30,t)=0.5)

Dose(Gy)	ODE	PDE
0.45 per day	384	394
0.9 per day	374	383
1.35 per day	367	376
1.8 per day	365	374
2.25 per day	359	368
2.7 per day	356	365
3.15 per day	359	368
3.6 per day	350	359

Table 8.10: Low Grade Glioma radiation: Localized Solution Case - normal tissue damage the same(cut off with $A(t) = 0.9$)

Dose(Gy)	ODE	PDE
0.45 per day	280	281
0.9 per day	205	208
1.35 per day	190	193
1.8 per day	185	188
2.25 per day	173	177
2.7 per day	167	171
3.15 per day	173	177
3.6 per day	156	160

CHAPTER 9

CONCLUSIONS AND FUTURE CHALLENGES

9.1 Traveling wave solution in a chain of periodically forced coupled nonlinear oscillators

In the present work we have revisited a generic nonlinear lattice model derived in
[6] and associated with the dynamics of a forced network of coupled oscillators. A
specific motivation for studying this system comes from its relevance to phosphenes,
artificial perceptions of light arising in the visual system in which contours, possibly
representing boundaries between sets of neurons in different activity states or phases,
emerge and propagate. We complemented the important initial steady state analy-
sis of [6] (see also [5]) by exploring the possibility of traveling waves in the system
of ordinary differential equations. This led us to introduce the co-traveling frame
(advance-delay) PDE and study existence and stability properties of the traveling
waves as both special periodic modulo shift solutions of the original systems of ODEs
and stationary solutions of the co-traveling frame PDE. Our results on traveling waves
complement the work of [6] on the existence and stability of standing waves. We found
a curve above which the standing waves become unstable. This curve agrees with and
extends the bifurcation curves obtained in [6] by analyzing the equilibrium states of
the ODE system. We showed that the instability of standing waves above the curve
leads to the emergence of stable traveling waves in some parameter regimes, while
at other parameter values traveling waves exhibit either frontal or background in-
stability. An analysis of the background steady states provided information about
the spectrum of these waves. From an applications perspective, a two-dimensional

collection of oscillators, corresponding to cells in the retina or in a layer of visual cortex, is most relevant, and for this reason we also considered some prototypical examples of two-dimensional evolution. In particular, we demonstrated that perturbed planar fronts can heal and resume their planar form, while radial fronts shrink. Our simulations of the system that initially has two fronts with bulging centers are in qualitative agreement with Carpenter's experimental observations [4] (see also the discussion of [5]).

The present work leads to numerous interesting questions for the further exploration of this and related systems. In particular, obtaining an analytical handle on the spectrum of the front in the co-traveling wave PDE and connecting this spectrum to the stability properties of the original ODEs would be extremely valuable from a theoretical perspective, not only in the context of the present setting but also for wide additional classes of lattice dynamical problems bearing traveling waves, such as generalized Frenkel-Kontorova (see [8] and references therein), Fermi-Pasta-Ulam (see e.g. [9, 11, 12] and the discussion of Chapter 1 in [13]) or nonlinear Schrödinger systems (see e.g. [14, 16, 17, 19] and the discussion of Chapter 21 in [20]). On the numerical front, while we explored a few prototypical cases of two-dimensional evolution, a better understanding of the stationary and traveling states in two dimensions clearly merits further investigation. Another interesting direction is to formulate and study solutions and spectra of a two-component problem that may support traveling pulses.

On the applications side, once the basic properties of this model system are more fully understood, it may serve as a form of computational test bed for exploring and making predictions about visual phenomena evoked by electrical stimulation. In this context, it may be interesting to explore the influence of changes in the amplitude or qualitative form of the forcing function on wave propagation [3] and to investigate waves induced by presenting traveling wave stimuli (e.g., [22, 23]), representing ob-

jects passing through the visual field, in addition to periodic forcing. Indeed, these adjustments may help resolve the model's current failure to capture the observation that neighboring fronts tend to propagate in a similar manner. At a more fundamental level, the present class of models appears to be a (modified) overdamped variant of the widely studied, so-called sine lattices (see e.g. [24] and, for a discussion of some of the relevant applications, [26]), hence it would be particularly interesting to explore hybrid variants of these models having as special case limits the overdamped and the undamped cases previously explored. Some of these issues are currently under investigation and will be reported upon in future publications.

9.2   Turing instability in a HCV model

Diffusion was added to an existing model for HCV. We have investigated extensively the possibility of Turing instability in the model numerically which appears to not exist. We have also shown analytically for certain regimes of the parameters that Turing instability can not exist. A slight variation of the existing model is introduced where Turing instability is demonstrated. A future goal is to study this model more extensively and study its robustness and limitations. Also we can look at other models which might exhibit Turing instability. In addition, it would be desirable to prove or disprove generally whether the original model can have Turing instability in whole parameter space.

9.3   Tumor dynamics

For tumor dynamics modeling, based on [47], we have studied an effective particle method derived from a PDE and compared the results predicted by the effective particle method and the PDE. We also included the radiotherapy in this comparison. We discussed about the low grade glioma radiation and studied the radiotherapy

effect when keeping the damage to normal tissue the same. For future work, we can try to design and compare other different radiotherapy methods.

BIBLIOGRAPHY

[1] L. Cervetto, G. C. Demontis, C. Gargini, Cellular mechanisms underlying the pharmacological induction of phosphenes, British J. Pharmacol. **150**, 383 (2007).

[2] E. Zrenner, Will retinal implants restore vision?, Science. **295**, 1022 (2002).

[3] E.J. Tehovnik, W.M. Slocum, Electrical induction of vision, *Neuroscience & Biobehavioral Review*, **37**, 803 (2013).

[4] R. Carpenter, Contour-like phosphenes from electrical stimulation of the human eye; some new observations, J. Physiol. **229**, 767 (1973).

[5] J. Drover, G. Ermentrout, Phase boundaries as electrically induced phosphenes, SIAM J. Appl. Dyn. Syst. **5**, 529 (2006).

[6] H. Parks, G. Ermentrout, J. Rubin, The dynamics of a forced coupled network of active elements, Physica D **240**, 554 (2011).

[7] B. Ermentrout, Simulating, analyzing and animating dynamical systems: a guide to XPPAUT for researchers and students, SIAM, Philadelphia, PA (2002).

[8] O. M. Braun and Y. S. Kivshar. The Frenkel-Kontorova model: concepts, methods and applications. Springer, Berlin-Heidelberg, 2004.

[9] G. Friesecke, R.L. Pego, Solitary waves on FPU lattices: I. Qualitative properties, renormalization and continuum limit, Nonlinearity, **12**, 1601 (1999); G. Friesecke, R.L. Pego, Solitary waves on FPU lattices: II. Linear implies nonlinear stability, Nonlinearity, **15**, 1343 (2002); G. Friesecke, R.L. Pego, Solitary waves on Fermi-Pasta-Ulam lattices: III. Howland-type Floquet theory, Nonlinearity, **17**, 207 (2004).

[10] G. Friesecke, R. L. Pego, Solitary waves on Fermi-Pasta-Ulam lattices: IV. Proof of stability at low energy, Nonlinearity, **17**, 2229 (2004).

[11] J. English and R. L. Pego, On the solitary wave pulse in a chain of beads, Proceedings of the AMS **133**, 1763 (2005).

[12] A. Stefanov and P. Kevrekidis, Traveling waves for monomer chains with pre-compression, Nonlinearity **26** 539 (2013).

[13] V. F. Nesterenko, Dynamics Of Heterogeneous Materials, Springer-Verlag, New York, 2001.

[14] D.E. Pelinovsky, V.M. Rothos, Bifurcations of traveling wave solutions in the discrete NLS equations, Phys. D **202**, 16 (2005).

[15] D.E. Pelinovsky, Translationally invariant nonlinear Schrödinger lattices, Nonlinearity **19**, 2695 (2006).

[16] O.F.Oxtoby, I. V. Barashenkov, Moving solitons in the discrete nonlinear Schrödinger equation, Phys. Rev. E **76**, 036603 (2007).

[17] T.R.O. Melvin, A.R. Champneys, P. G. Kevrekidis and J. Cuevas, Radiationless traveling waves in saturable nonlinear Schrödinger equation, Phys. Rev. Lett. **97**, 124101 (2006);

[18] T.R.O. Melvin, A.R. Champneys, P.G. Kevrekidis and J. Cuevas, Traveling solitary waves in the discrete Schrödinger equation with saturable nonlinearity: Existence, stability and dynamics, Physica D **237**, 551 (2008).

[19] M. Syafwan, H. Susanto, S.M. Cox and B.A. Malomed, Variational approximations for traveling solitons in a discrete nonlinear Schrödinger equation, J. Phys. A: Math. Theor. **45**, 075207 (2012).

[20] P. G. Kevrekidis, The discrete nonlinear Schrödinger equation: mathematical analysis, numerical computations and physical perspectives, Springer-Verlag, Heidelberg, (2009).

[21] A. Carpio, L. L. Bonilla, Wave front depinning transition in discrete one-dimensional reaction-diffusion systems, Physical Review Letters 86 (26) (2001) 6034.

[22] S.E. Folias and P.C. Bressloff, Stimulus-locked traveling waves and breathers in an excitatory neural network, SIAM J. Appl. Math., **65**, 2067 (2005).

[23] G.B. Ermentrout, J. Jalics, and J. Rubin, Stimulus-driven traveling solutions in continuum neuronal models with a general smooth firing rate function, SIAM J. Appl. Math., **70**, 3039 (2010).

[24] S. Homma and S. Takeno, A coupled base-rotator model for structure and dynamics of DNA local fluctuations in helical twist angles and topological solitons, Progress of Theoretical Physics **72**, 679 (1984).

[25] S. Takeno and S. Homma, Kinks and breathers associated with collective sugar puckering in DNA, Progress of Theoretical Physics. **77**, 548 (1987).

[26] F. Zhang, Kink shape modes and resonant dynamics in sine-lattices, Physica D: Nonlinear Phenomena **110**, 51 (1997).

[27] Eusebius Doedel, Lecture Notes on numerical analysis of nonlinear equation, (2010).

[28] K. W. Morton and D.F Mayers, Numerical solution of partial differential equations Chapter 4, Cambridge University Press (1994).

[29] T. C. Reluga, H. Dahari, A. S. Perelson, Analysis of Hepatitis C Virus infection models with Hepatocyte Homeostasis, SIAM Journal on Applied Mathematics. **69**, 999 (2009).

[30] Linda J. S. Allen, An introduction to mathematical biology Ch. 4 Linear Differential Equations: Theory and Examples (2007).

[31] J. D. Murray, Mathematical Biology I and II, Third Edition, Springer-Verlag (2002).

[32] A. U. Neumann, N. P. Lam, J. Dahari, D. R. Gretch, et al., Hepatitis C viral dynamics in vivo and the antiviral efficacy of interferon-alpha therapy, Science, **282**, 103 (1998).

[33] H. Dahari, A. Lo, R. M. Ribeiro, Modeling hepatitis C virus dynamics: Liver regeneration and critical drug efficacy, Journal of Theoretical Biology, **47**, 371 (2007).

[34] H. Dahari, R. M. Ribeiro, and A. S. Perelson, Triphasic decline of HCV RNA during antiviral therapy, Hepatology, **46**, 16 (2007).

[35] NIH, National Institutes of Health Concenesus Development Conference: Management of hpatitis C, Hepatology, **36**, S3 (2002).

[36] A. Perelson, A. Neumann, M. Markowitz, J. Leonard, and D. Ho, HCV-1 dynamics in vivo: Virion clearance rate, infected cell life-span, and viral generation time, Science, **271**, 1582 (1996).

[37] A. S. Perelson, Modelling viral and immune system dynamics, Nature Reviews Immunology, **2**, 28 (2002).

[38] Wei X, Ghosh SK, Taylor ME, Johnson VA, Emini EA, Deutsch P, Lifson JD, et al., Viral dynamics in human immunodeficiency virus type 1 infection, Nature, **373**, 117 (1995).

[39] A. S. Perelson, E. Herrmann, F. Micol, and S. Zeuzem, New kinetic models for the hepatitis C virus, Hepatology. **42**, 749 (2005).

[40] H. Dahari, M. Major, X. Zhang, K. Mihalik, C. M. Rice, A. S. Perelson, S. M. Feinstone, and A. U. Neumann, Mathematical modeling of primary hepatitis C infection: Noncytolytic clearance and early blockage of virion production, Gastroenterology, **128**, 1056 (2005).

[41] I. R. Mackay, Hepatoimmunology: A perspective. Special Feature, Immunology and Cell Biology, **80**, 36 (2002).

[42] R. N. M. Macsween, A. D. Burt, B. C. Portmann, K. G. Ishak, P. J. Scheuer, and P. P. Anthony, Pathology of the Liver, Churchill Livingstone, London (1987).

[43] R. A. Macdonald, 'Lifespan' of liver cells. Autoradio-graphic study using tritiated thymidine in normal, cirrhotic, and partially hepatectomized rats, Archives of Internal Medicine, **107**, 335 (1961).

[44] S. Sherlock and J. Dooley, Diseases of the Liver and Biliary System, Blackwell Science (2002).

[45] N. D. Theise, M. Nimmakayalu, R. Gardner, P. B. Illei, G. Morgan, L. Teperman, O. Henegariu, and D. S. Krause, Liver from bone marrow in humans, Hepatology, **32**, 11 (2000).

[46] R. Ribeiro, Dynamics of alanine aminotransferase during hepatitis C virus treatment, Hepatology, **38**, 509 (2003).

[47] Juan Belmont-Beita, Gabriel F. Calvo and Victor M. Perez-Garcia, Effective particle methods for Fisher-Kolmogorov equations: theory and applications to brain tumor dynamics, Communications in Nonlinear Science and Numerical Simulation **19**, 3267 (2014).

[48] C. Wang, J. K. Rockhill, M. Mrugala, D.L. Peacock, A. Lai, K. Jusenius, J. M. Wardlaw, T. Cloughesy, et al., Prognostic significance of growth kinetics in newly diagnosed glioblastomas revealed by combining serial imaging with a novel biomathematical model, Cancer Research. **69**, 9133 (2009).

[49] K. R. Swanson, R. Rostomily, E. C. Alvord, Jr, Predicting Survival of Patients with Glioblastoma by Combining a Mathematical Model and Pre-operative MR imaging Characteristics: A Proof of Principle, British Journal of Cancer, **98**, 113 (2008).

[50] V. M. Perez-Garcia, G. F. Calvo, J. Belmonte-Beitia, D. Diego, L. A. Perez-Romasanta, Bright solitons in malignant gliomas, Phys. Rev. E **84**, 021921 (2011).

[51] N. Shigesada, K. Kawasaki, Biological Invasions: Theory and Practice, Oxford University Press (1997).

[52] V. Volpert, S. Petrovskii, Reaction-diffusion waves in biology, Physics of Life Reviews **6**, 267 (2009).

[53] Albert Van der Kogel, Michael Joiner, Basic clinical radiobiology, Oxford University Press, (2009)

[54] J. A. Sherrat, On the transition from initial data to travelling waves in the Fisher-KPP equation, Dynamics and Stability of Systems **13**, 167 (1998).

[55] A. Kolmogoroff, I. Petrovsky, and N. Piscounoff, Etude de l'equation de la diffusion avec croissance de la quantite de matiere et son application a un probleme biologique. Moscow University, Bulletin of Mathematical Sciences **1**, 1 (1937).

[56] M. J. Ablowitz, A. Zeppetella, Explicit solutions of Fisher's equation for a special wave speed, Bulletin of Mathematical Biology. **41**, 835 (1979).

[57] E. Mandonnet, J-Y Delattre, M-L Tanguy, K. R. Swanson, A. F. Carpentier, H. Duffau, P. Cornu, R. Van Effenterre, E. C. Alvord Jr., and L. Capelle, Continuous growth of mean tumor diameter in a subset of WHO grade II gliomas, Annals of Neurology, **53**, 524 (2003).

[58] S. Jbabdi, E. Mandonnet, H. Duffau, L. Capelle, K. R. Swanson, M. Pelegrini-Issac, R. Guillevin, H. Benali, Simulation of anisotropic growth of low-grade gliomas using diffusion tensor imaging, Magnetic Resonance in Medicine, **54**, 616 (2005).

[59] C. Gerin, J. Pallud, B. Grammaticos, E. Mandonnet, C. Deroulers, P. Varlet, L. Capelle, L. Taillandier, L. Bauchet, H. Duffau, M. Badoual, Improving the time-machine: estimating date of birth of grade II gliomas. Cell Proliferation. **45**, 76 (2012).

[60] K. R. Swanson, R. C. Rockne, J. Claridge, M. A. Chaplain, E. C. Alvord Jr, A. R. Anderson, Quantifying the role of angiogenesis in malignant progression of gliomas: in silico modeling integrates imaging and histology, Cancer Research **71**, 7366 (2011).

[61] Ruiz, J., Lesser, G. J., Low-Grade Gliomas, Current Treatment Options in Oncology, **10**, 231 (2009).

[62] V. M. Perez-Garcia, M. Bogdanska, A. Martinez-Gonzalez, J. Belmonte, P. Schucht, L. A. Perez-Romasanta, Delay effects in the response of low grade gliomas to radiotherapy: A mathematical model and its therapeutical implications, Mathematical Medicine and Biology, **32** 397 (2015).

[63] Francesco Pignatti, Martin van den Bent, et al., Prognostic factors for survival in adult patients with cerebral low-grade glioma, Journal Clinical Oncology., **20**, 2076 (2002).

[64] Higuchi Y., Iwadate Y. Yamaura A., Treatment of low-grade oligodendroglial tumors without radiotherapy., Neurology **63**, 2384 (2004).

[65] Nader Pouratian, David Schiff, Management of low-grade glioma, Current Neurology and Neuroscience Reports, **10**, 224 (2010)

[66] A. B. M. Karim, B. Maat, et al., A randomized trial on dose-response in radiation therapy of low-grade cerebral glioma: EORTC study 22844, International Journal of Radiation Oncology. Biology. Physics. **36**, 549 (1996).

[67] J. Pallud, L. Taillandier, L. Capelle, D. Fontaine, M. Peyre, et al., Quantitative Morphological MRI Follow-up of Low-grade Glioma: A Plead for Systematic Measurement of Growth Rates, Neurosurgery **71**, 729 (2012).

[68] J. Pallud, J. F. Llitjos, F. Dhermain, P. Varlet, E. Dezamis, et al., Dynamic imaging response following radiation therapy predicts long-term outcomes for diffuse low-grade gliomas, Neuro Oncol, **14**, 496 (2012).